University of Silesia
Institute of Physics

Natalia Woźnica

Ph.D. Thesis

The atomic scale structure of nanocarbons: modelling and experimental verification by neutron and X-ray diffraction, Raman spectroscopy and electron microscopy.

Supervisor:

prof. dr hab. Andrzej Burian

Katowice, 2016

Acknowledgements

The work presented in this thesis would not have been possible without the support of various people and organizations, and I would like to express my gratitude for them here. Being as scatterbrained as I am I would like to apologise in advance to those whom I accidentally omitted. I would like to thank following people:

Andrzej Burian for his supervision, discussions and endless patience, especially with text corrections, as well as for sharing his programs used in this work,

Lukasz Hawelek for his help and advice, especially with computational methods,

Stanislaw Duber for his help with synthesis of the saccharose and cellulose samples, for sharing his vast knowledge about activated carbons,

At the ILL for supervision during my stay there and for introducing me to the world of neutrons:

Henry E. Fischer,
Stephane Rols,
Gabriel Cuello,
Michela Brunelli,
Helmut Schober,

Veijo Honkimäki for his help with synchrotron measurements,

Miroslawa Pawlyta for providing HRTEM images,

Alain Bulou for his help with Raman measurements,

Ivan Bobrinetskiy for supplying the graphene sample.

Moreover I would like to acknowledge the support of Polish National Science Centre. This work was supported by NCN project DEC-2013/09/N/ST3/01686

Abstract

The aim of this study was to describe the atomic structure of a series of carbon-based materials such as graphene, carbonized cellulose and saccarose along with activated carbons obtained from carbonized samples. While graphene is a relatively new and innovative material, activated carbons have been in use since ancient times. Historically they were used as a medicine and nowadays they have found much wider applications. Their great usefulness lies mostly in their porous structure and greatly expanded specific surface.

The primary techniques in this work were wide angle diffraction of neutrons and X-rays combined with computer simulations. Because the investigated materials had very small ordered structures it was necessary to analyse data in both real ($S(Q)$) and reciprocal space (PDF). First, the structure was estimated by the paracrystalline model, and then models containing physical defects were simulated with molecular dynamics. In molecular dynamics simulations point-type defects were considered. The *REBO* (Reactive Empirical Bond Order) potential was used for atoms within one layer and the Lennard-Jones potential was applied for consecutive layers. Additional information was obtained from High Resolution Transmission Electron Microscopy and Raman spectroscopy. The obtained results suggest that the investigated graphene consists mainly of 3-layered structures 36 Å in diameter and containing di-vacancies. In case of both pairs precursor-activated carbon, a change in structure after activation was noticed – the creation of multi-layered additions within the created pore walls. In all cases vacancies are preferred over STW type of defect. Carbonized saccarose contained mostly 4-layered structures of 24 Å and after activation it became a 3-layered structure of 24 Å diameter with a 10% addition of a 15-layered structure. For cellulose the numbers present in the following way: carbonized sample – 3 layers of 9.6 Å; activated sample – 3 layers + 20% 18 layers of 22 Å.

Contents

1 Introduction

In this work, a study of the atomic structure of various forms of nanocarbon samples is presented. The techniques selected for this task were Wide Angle Neutron Scattering (*WANS*), Wide Angle X-ray Scattering (*WAXS*), High Resolution Transmission Electron Microscopy (*HRTEM*), and Raman scattering. In order to obtain the most of structural information from diffraction data, computer simulations were performed. In addition to Molecular Dynamics, simulations based on the paracrystalline idea were carried out. The samples included in this work are two sets of precursor – activated carbon pairs and graphene. The activated carbons were obtained from carbonized saccharose and cellulose which were also included in study. Even though the samples look different on the macroscopic scale, the graphene as ultra light, fluffy powder, saccharose samples more like a powder composed of shiny black little crystals, while cellulose samples look like black spongy powder, they have proven to have similar structures on the atomic scale. This work presents a walk through of the reasons on which this conclusion is based.

In Chapter 2 information about carbon materials is gathered. Graphene is a relatively new nanomaterial with many promising applications. On the other hand activated carbons were in medicinal use since ancient times. Nowadays their application range broadened. The applied techniques are discussed in Chapter 3. The *HRTEM* provided images of the sample and Raman scattering gave insights into the disorder of the sample. From the diffraction data combined with computer simulations conclusions about averaged atomic structure were drawn. The results are gathered in Chapter 4, grouped by the type of the sample: graphene, saccharose and cellulose. In the last chapter – Chapter 5 a summary is presented.

2 Carbon materials

2.1 General information

Carbon forms a vast number of compounds (natural and synthetic). It outnumbers all other known compounds aside from hydrogen ones. To this number we can also add different carbon structures. Starting from plain graphite, through beautiful diamonds to exotic nanotubes, fullerenes, nanoonions... The list of nanocarbon structures seems to be constantly growing. Moreover, almost all of them can be decorated with other compounds changing their properties. Properties of carbon-obtained materials can also vary a lot depending on their structure. Just by changing the number of equivalent bonds one can go from one of the hardest material, such as diamond, to graphite, which is a relatively soft and weakly-bonded material (along c axis). The basic properties of carbon are gathered in Table 2.1. A few chosen forms of carbon materials are discussed in more detail further in this section.

2.1.1 Graphite

Graphite is an allotrope of carbon, its structure is shown in Figure 2.1. It is a gray mineral with metallic luster and it is oily in touch. Sp^2 hybridization (trigonal one) implies that each atom is bound to 3 other neighbours while the 4th valence electron is delocalized forming a π bond. The length of the C-C bond is equal to 142 pm, and the valence angle is 120^o. Due to this delocalized orbital graphite behaves as semimetal. Weak interaction between layers is of the van der Waals type and results in a much larger distance between layers – 335 pm. Within a layer, graphite is ordered in the so-called honeycomb structure, while the whole crystal has the hexagonal structure. The alternating layers are stacked in the A-B-A-B sequence.

Table 2.1: Basic properties of carbon [1].

symbol	C
atomic number	6
electron configuration	$1s^2 2s^2 2p^2$
atomic mass [u]	12.0107
triple point (diamond-liquid-vapour) [K]	4765
sublimation point [K]	3915
graphite density $\left[\mathrm{g \cdot cm^{-3}}\right]$	2.1-2.3
diamond density $\left[\mathrm{g \cdot cm^{-3}}\right]$	3.514
ionization energy $\left[\mathrm{kJ \cdot mol^{-1}}\right]$	1086.4
bond energy C-C $\left[\mathrm{kJ \cdot mol^{-1}}\right]$	348
bond energy C-H $\left[\mathrm{kJ \cdot mol^{-1}}\right]$	411
bond energy C-O $\left[\mathrm{kJ \cdot mol^{-1}}\right]$	358
covalent radius [pm]	77
ionic radius C^{4+} LK=4 [pm]	15

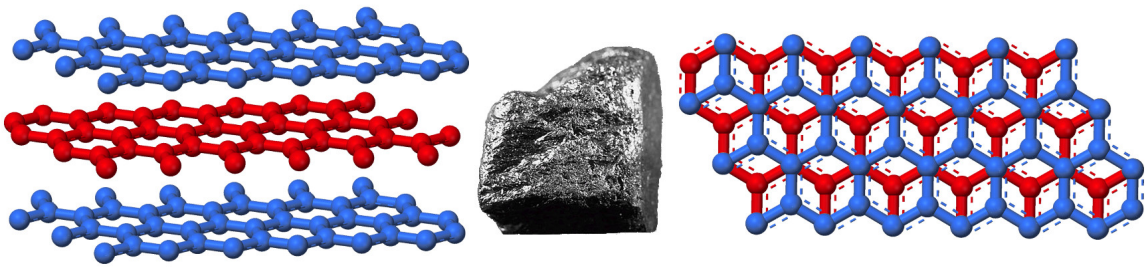

Figure 2.1: Structure of graphite (left & right), graphite as a mineral (center).

2.1.2 Turbostratic carbon

One can think of turbostratic carbon as graphite that lost its order along the c axis. Such kind of disorder can be imposed on the graphite structure by random translation or rotation of subsequent layers. However, the honeycomb structure is still preserved within a layer. Due to the disorder present in the structure, the interlayer distances in turbostratic carbon are approximately 344 pm and are clearly greater than those of graphite [2]. The key word here is *approximately* as the distance between layers is not constant and changes for various carbon materials. The differences between graphite and turbostratic carbon are shown in Figure 2.2. As in any crystal, topological defects can occur within a layer and deformation of such a layer can arise [3].

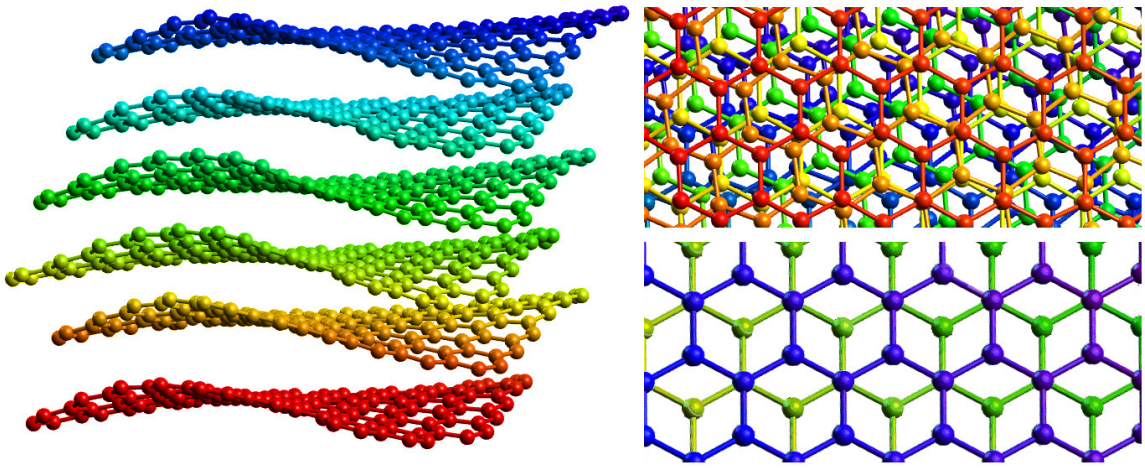

Figure 2.2: Structure of turbostratic carbon: side view (left), top view (top right) and structure of graphite for comparison (bottom right).

For diffraction purposes (discussed further in Chapter 3.1.1 and Chapter 3.1.2) we will consider only translational disorder omitting the rotational one as it will have similar effect on the diffraction pattern of powder carbon materials. We can describe the position of atom n in cell m_1m_2 layer m_3 as [4]:

$$R_m^n = m_1a_1 + m_2a_2 + m_3a_3 + \mathbf{r_n} + \delta m_3a_1 + \epsilon m_3a_2 \tag{2.1}$$

where $\mathbf{r_n}$ is the base vector of atoms of type n, and δ and ϵ are chosen randomly.

2.1.3 Graphene

Graphene is a single layer of graphite – carbon ordered in the honeycomb lattice. Each atom has sp^2 hybridization and is bound to 3 other neighbours. It also has a delocalized π orbital. However, in contrast to graphite, it does not contribute via van der Waals forces to the formation of 3D material. Until recently graphene was only a virtual concept used to describe and explain properties of materials such as graphite, or nanotubes. The material itself was thought to be too unstable to exist in a free state. However, in 2004 it [5] was proven otherwise. The first method to obtain graphene did not require much more than a piece of graphite and a scotch tape.

Many different methods were developed since then [6]. Mostly they involve some kind of exfoliation process, however many others depend on "bottom up" synthesis or deposition processes. They also vary a lot in terms of specialised equipment which is needed. Some need chemical compounds or equipment only seen in laboratories while others need as little as the aforementioned scotch tape or plain simple kitchen blender along with some soap. Unfortunately, most of these methods struggle with issues such as scalability and defects which directly influence the material properties [7]. Moreover, most of them initially produce a mixture of single-layered graphene and few-layered graphene. A lot of effort is invested into improving those techniques as graphene is a very promising material in nanotechnology. Due to its structure it has unique mechanical, electronic and thermal properties that make it an exceptional material for applications in transparent electrodes [8], field-effect transistors [9], ultrasensitive sensors [10], and novel nanocomposites for energy storage [11].

2.1.4 Activated carbon

While the question about structure of activated carbons (ACs) dates back to the middle of the 20-th century, the material itself has been known since ancient times. ACs were mentioned in ancient Egyptian papyri or by Hippocrates. The first to have looked into their structure was R. Franklin [12]. Their numerous applications strongly rely on their significantly expanded specific surface. They can reach as much area as a football field in a mass of just 3.5 g of carbon, which is the equivalent of 17.5 carat. For comparison, the

Williamson pink diamond owned by Queen Elizabeth II set in a flower brooch weights 23.6 carats. The origin of such an expanded surface lies in the porosity of ACs. This porous material is used almost everywhere: as a medicine, in various types of filters, for fuel storage, or in supercapacitors.

ACs can be obtained from almost anything containing carbon. Of course in such a situation, a preparatory step in the form of carbonization is required. Most commonly they are obtained from coals or carbonized materials like timber, coconut shells or sugars. ACs are obtained in a process called activation. The activation process both creates new pores, and improves access to ones already existing within the material [13]. The activation process can be classified as chemical or thermal. Thermal activation requires high temperature, oxygen or carbon dioxide, and sometimes steam to burn-off carbon atoms from the structure. As the name suggests, in chemical activation different kinds of chemicals are involved in "plucking" atoms [14]. The most common ones are: $ZnCl_2$, H_3PO_4 or KOH. It can also be: $AlCl_3$, $MgCl_3$, $NaOH$ and many others. Heat treatment is also often required in this type of activation.

As pores are such an important feature in ACs it was suggested to classify them by size [15]:

- micropores are smaller than 2 nm,
- mesopores are within $2 - 50$ nm,
- macropores are bigger than 50 nm.

While micropores are responsible for most of the specific surface in the material, bigger pores are as important, providing access to the smaller ones.

A quantity mentioned before, *specific surface*, defined as $\frac{area}{mass}$, is often used to characterize AC. An attempt to quantify it by measurement can be done by carrying out a BET measurement. BET stands for the Brunauer, Emmett, and Teller isotherm equation. In this method, the adsorption isotherms of gases are used to calculate specific surface. It is very useful for mesoporous and macroporous surfaces, however with microporous systems it sometimes gives imprecise results. [16]

As it was mentioned before, the first attempt to describe the structure of ACs was made

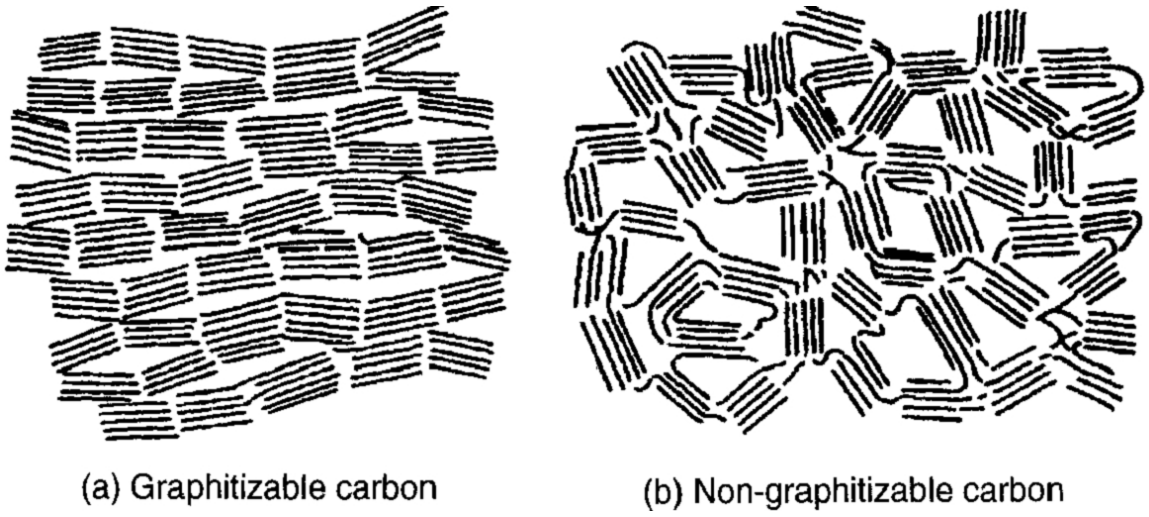

Figure 2.3: ACs as categorized by Franklin.

by Rosalind Franklin. She described them using microcrystalites of graphite. She also divided them into two groups: graphitizing and non-graphitizing ones (Figure 2.3).

The graphitizing ones are much more ordered and upon a high temperature treatment transform into graphite. Non-graphitizing ones, as the name suggests, do not transform into graphite. Such a behaviour was explained through the existence of graphene "linkers" between microcrystalites which are responsible for their much more stable structure.

The question of the AC structure resurfaced recently with the discovery of fullerenes and nanotubes as they introduced curved surfaces, linked with the formation of non-hexagonal rings in the honeycomb lattice. This idea incorporates in a better way the porous nature of ACs [17–21].

2.2 Samples

2.2.1 Graphene

The sample investigated in this work was provided by Carbonlight Company (Russia). It was obtained from graphite by chemical exfoliation. The graphite was oxidized following the modified Hummers method [22] and subsequently reduced. Oxidation was achieved by following several steps. First, a graphite powder was mixed with a solution of

sulphuric and nitric acids while stirred and cooled. Then, potassium permanganate ($KMnO_4$) was added to the mixture. The concentration of $KMnO_4$ was three times higher than the concentration of the graphite powder. Hydrogen peroxide was then added with care and after an hour it was diluted three times with distilled water. The suspended fraction was left for a few hours to sediment. The sought fraction was the upper transparent layer and it was carefully decanted. The obtained material was filtered, washed with distilled water and dried at room temperature until a constant weight was obtained. The obtained graphite oxide was then reduced by heat treatment. Such a process resulted in the exfoliation of the obtained powder.

2.2.2 Saccharose samples

Saccharose, commonly known as sucrose or sugar, is a disaccharide combination of glucose and fructose. Its chemical formula is $C_{12}H_{22}O_{11}$, the molecule is presented in Figure 2.4.

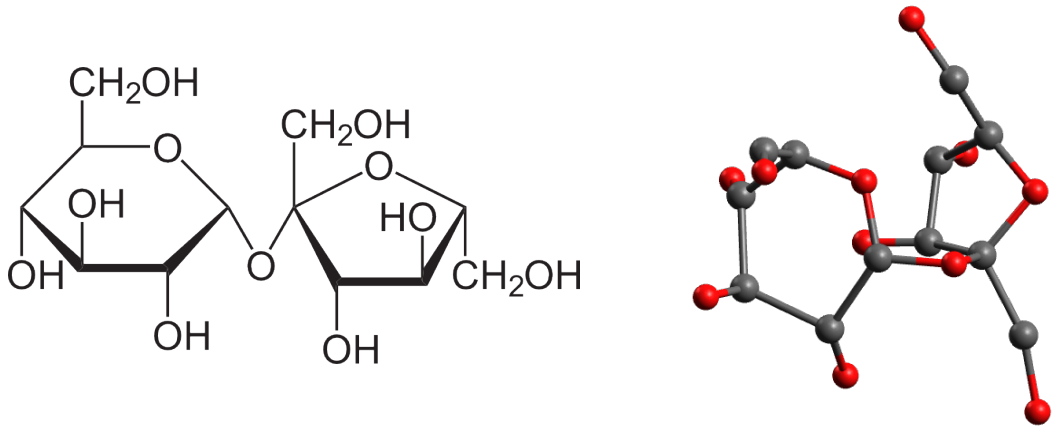

Figure 2.4: A saccharose molecule. Left: simplified schematics, right: visualisation of the molecule. In the visualisation hydrogen atoms were removed for clarity reasons. Gray color represents carbon atoms, while red stands for oxygen.

Carbonized saccharose

Pure saccharose was caramelized in a ceramic bowl in an oven in ambient atmosphere up to 200°C. After the heat treatment, the obtained black stiff foam was crunched and

subjected to the next step of heat treatment. The second step was to heat treat the sample in a tube furnace up to targeted temperature 950°C with a 4 °C/min heating ratio. The sample was under constant argon flow and was kept at the target temperature for 60 min. The sample cooled down naturally still under argon flow.

Activated saccharose

In order to activate the previously obtained carbonized saccharose, it was ground with $NaOH$ in a weight ratio of 1 : 2. The next step was to heat treat such a mixture. It was performed in a tube furnace under argon flow at a ratio of 4 °C/min up to 850 °C at which point the sample was left at constant temperature for 1 hour. The sample was allowed to cool down naturally. To purify the sample, it was soaked numerous times in distilled water, vacuum filtered and finally dried in a furnace. As the porous nature of the sample made it difficult to purify the sample from $NaOH$ contamination even after long treatment with distilled water, the sample was heat treated once again. This time the targeted temperature was 1000°C under argon flow.

2.2.3 Cellulose samples

Cellulose is a polysaccharide with the chemical formula $(C_6H_{10}O_5)_n$. It is found in primary cell wall of green plants. The cellulose molecule is presented in Figure 2.5.

Carbonized cellulose

Pure cellulose underwent similar treatment as pure saccharose. The first step of heat treatment was unnecessary and pure cellulose was only treated in a tube furnace.

Activated cellulose

Carbonized cellulose underwent exactly the same treatment as carbonized saccharose

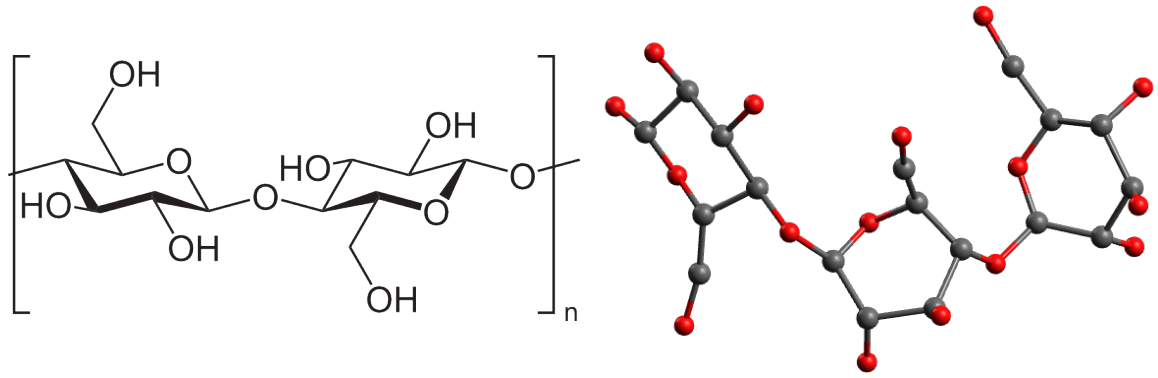

Figure 2.5: A cellulose molecule. Left: simplified schematics, right: visualisation of the molecule. In the visualisation hydrogen atoms were removed for clarity reasons. Gray color represents carbon atoms, while red stands for oxygen.

3 Theoretical background

3.1 Experimental measurements

3.1.1 Wide Angle Neutron Scattering

The neutron is a particle discovered by Chadwick in 1932, which is built from one u and two d quarks. It possesses a spin of $1/2$ and its mass is $m_n = 1.0087\,\mathrm{u}$ [23]. A neutron of certain velocity v can be linked with the de Broglie wavelength λ through the equation:

$$\lambda = \frac{h}{m_n v} \tag{3.1}$$

which then can be transformed to a wavelength – energy relation:

$$\lambda = \sqrt{\frac{82}{E}}\,\left[\text{Å, meV}\right] \tag{3.2}$$

and the wavelength – temperature relation [24]:

$$\lambda = \sqrt{\frac{633}{T}}\,\left[\text{Å, K}\right] \tag{3.3}$$

The neutron is unstable outside of nuclei and decays as follows:

$$n \rightarrow e^- + p^+ + \bar{\nu_e}$$

Its half life time equals $T_{1/2} = 615\,\mathrm{s}$ [25]. A nuclear reaction is needed in order to obtain free neutrons. The most effective sources of neutrons are the fission process and spallation.

Spallation sources

One way to obtain a high number of neutrons for scientific purposes requires a target built of heavy nuclei and a beam of much lighter particles. Very often lead or uranium

are used as a target and the proton functions as a bullet. By hitting the target, the lighter particle breaks off parts of the target nucleus. The nucleus is excited as well, and as a result even more particles are released by evaporation.

In Switzerland at the Paul Scherrer Institute there is one of the European spallation sources – SINQ. It is a continuous source with parameters as discussed below [26]. After passing through three of SINQ's accelerators, the delivered proton beam achieves 590 MeV in energy at a current up to 2.3 mA. As at the PSI they have two pion production targets, the proton energy is reduced to 570 MeV by passing through them. The lead target is suspended in a heavy water tank from which neutrons are extracted.

Another European spallation source called ISIS is located in England. ISIS is a pulsed source with parameters as discussed below [27]. ISIS's linac provides 200 μs long, 22 mA pulses of proton beam. After acceleration, the proton pulses are cumulated in order to achieve higher current of the beam. In the end, a mean current of 200 μA is delivered to the targets. At ISIS there are 2 target stations. The first target station receives 160 kW proton beam at tungsten plates. The second one is a low power one and is still under development.

A promising spallation source is currently being developed in Lund in Sweden [28]. It is designed to leave behind both current spallation sources, as well as excel in terms of overall brilliance in comparison to reactor sources, which as of the moment remain unbeatable. The first neutrons are expected to be available in 2019, while the facility is expected to be functional in full capability around 2025. The accelerator is designed to provide a 2.86 ms long proton pulse at 2 GeV at a repetition rate of 14 Hz which represents 5 MW of average beam power with a 4% duty cycle on target. The target is designed to be a 4-tonne helium-cooled tungsten wheel.

Reactor sources

While the best spallation sources can achieve a quite remarkable neutron flux of a pulse, they still struggle with overall brilliance. Until the European Spallation Source is operational, high-flux reactor-based sources will be the most powerful in terms of total flux. A source of neutrons in a reactor is a fission reaction. ^{235}U is used as a fuel. When

a nucleus absorbs a thermal neutron it becomes excited and breaks into a few heavy parts. At that time neutrons are also produced. On average, a single event creates about 2.5 neutrons and 1.5 neutrons are needed to sustain the reaction. The leftover one neutron can be used to feed instruments hooked up to the reactor.

One of the most brilliant sources of neutrons obtained in such way is the Institut Laue-Langevin (ILL) located in Grenoble in France [29]. Using highly enriched uranium as a fuel, combined with brilliant engineering work it provides its users with a flux of 1.5×10^{15} neutrons/s/cm^2 while the reactor operates at a thermal power of 58.3 MW. Usually during the year it operates in 4 cycles, with each cycle lasting 50 days.

The obtained neutrons are too "hot" for most purposes, which means that they posses excessive kinetic energy. In order to slow them down moderators are used. In a reactor a heavy water tank not only moderates neutrons but reflects them as well. Neutrons obtain thermal equilibrium with the moderator and as such they change their energy spectrum. Change in energy means that the wavelength changes as well. At the ILL, apart from the majority of thermal neutrons – at equilibrium with 25°C, users have access to neutrons from a hot source which are at thermal equilibrium with a heated (by radiation within the reactor) piece of graphite $\sim$ 2000°C and ones from two cold sources where equilibrium is reached with liquid deuterium. Ultra cold neutrons are obtained by gravitationally and then mechanically even further slowing down neutrons from a cold source.

After moderation neutrons have a Maxwellian distribution of energy. Thus there is a need for a monochromator if the experiment requires a certain wavelength. However as neutrons are scarce, there is often a trade off in quality of monochromation for higher flux.

The scattering process

As in this work only scattering from powders is considered, the discussion here will also be limited to it i.e. to scattering averaged over all orientations in 3D space. The scattering process can be perceived as momentum transfer between an incident neutron and a scattered one [30]. As one can use different wavelengths in a continuous way,

it is quite important to make a transition from the 2θ space to the $\mathbf{Q}$ space in order to become wavelength-independent in data treatment. The $\mathbf{Q}$ vector is defined as the difference between two wave vectors: $\mathbf{k_0}$ – the incident one and $\mathbf{k_s}$ – the scattered one. It is visualised in Figure 3.1. In the case of an elastic scattering the magnitude of $k_0 = k_s = 2\pi/\lambda$ which leads to $Q = 4\pi \sin\theta/\lambda$ where the previously mentioned 2θ is the scattering angle and λ is the used wavelength.

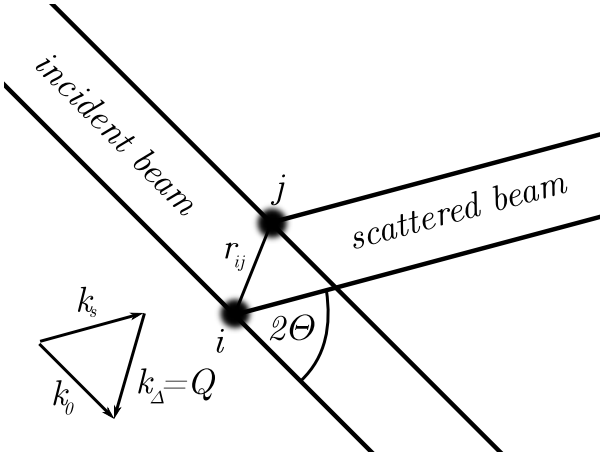

Figure 3.1: Representation of scattering on point like centres.

Intensity measured by a detector of solid angle $\mathrm{d}\Omega$ in such an event can be expressed as [31]:

$$I(Q) = \Phi \frac{\mathrm{d}\sigma}{\mathrm{d}\Omega}(Q)\mathrm{d}\Omega \tag{3.4}$$

where: Φ is the incident flux on the sample, $\dfrac{\mathrm{d}\sigma}{\mathrm{d}\Omega}(Q)$ is the differential scattering cross-section expressed as (3.5), while assuming perfect efficiency of detection $\epsilon(E_f) = 1$.

The previously mentioned differential scattering cross-section:

$$\frac{\mathrm{d}\sigma}{\mathrm{d}\Omega}(Q) = \left\langle \sum_{i,j}^{N} \overline{b_i b_j^*}\, e^{i\mathbf{Q}\cdot\mathbf{r_{ij}}} \right\rangle \tag{3.5}$$

where: N is the number of scattering centres, $\mathbf{Q}$ is the scattering vector, $\mathbf{r_{ij}}$ represents relative position of scattering centres i and j, and b is the scattering length of carbon.

The structure factor

In order to present data in reciprocal space, the structure factor $S(Q)$ can be calculated. As the scattering length b is angle-independent, there is less pressure to calculate

structure factors for neutron data. However it is still a valuable thing to do as it will allow us to compare directly the results obtained from the neutron scattering experiment with the X-ray one.

After intensity is corrected and normalized, the structure factor can be calculated as (monoatomic case):

$$S(Q) = 1 + \frac{I(Q) - \overline{b^2}}{\overline{b}^2} \tag{3.6}$$

where $I(Q)$ is the corrected intensity, b is the scattering length of carbon, $\overline{b^2}$ and $\overline{b}^2$ are defined below.

$$\overline{b^2} = \overline{b_i b_j^*} = \overline{b_i b_i^*} \quad i = j \quad \text{(same site)}$$

$$\overline{b}^2 = \overline{b_i b_j^*} = \overline{b_i}\,\overline{b_j^*} \quad i \neq j \quad \text{(different site)}$$

The pair distribution function

The small size of coherently scattering regions, as well as disorder within the sample make analysis of the diffraction data in reciprocal space (or in Q space) more difficult. A correlation function can be introduced in order to gain more information about the sample structure.

The one chosen in this work is the Pair Distribution Function (PDF). It is a function defined in real space correlated with $S(Q)$ through the sine Fourier transform as:

$$PDF = G(r) = \frac{2}{\pi}\int_0^{Q_{max}} Q[S(Q) - 1]\sin(Qr)\frac{\sin(\pi Q/Q_{max})}{\pi Q/Q_{max}}dQ \tag{3.7}$$

where Q_{max} is the maximum value of the scattering vector available in the experiment and the last term denotes the Lorch modification function that reduces effects arising from the finite value of the upper Q limit.

The function gives direct information about the inter-atomic distances within the sample. Each one of its peaks corresponds to an atom existing within the sample, with r being the atom-atom distance. Its physical visualisation is presented in Figure 3.2 [32].

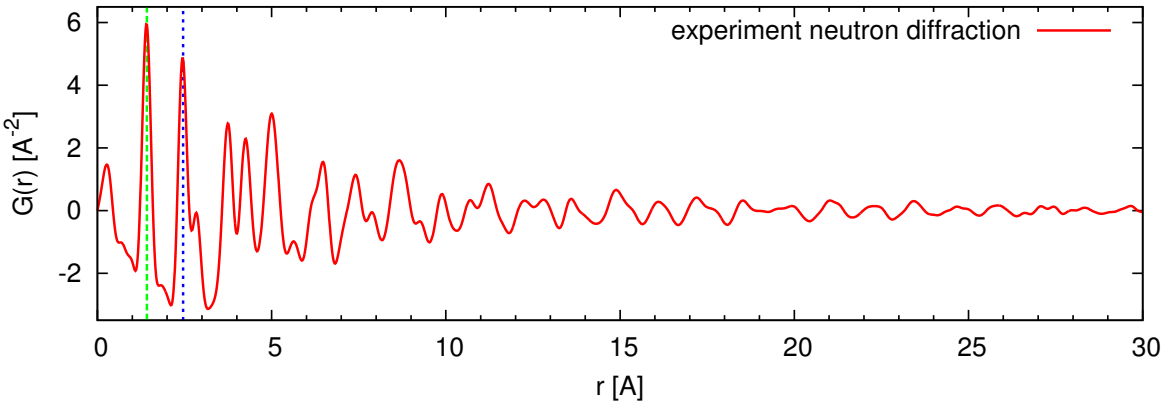

PDF calculated for data measured for graphene with 1.42 Å and 2.46 Å marked

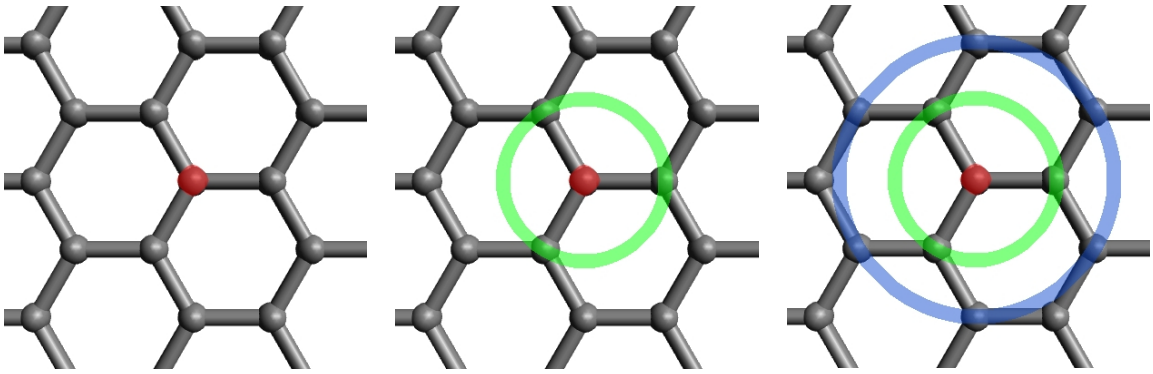

selected atom 1^{st} shell 1^{st} and 2^{nd} shell

Figure 3.2: Visualisation of a PDF, demonstrated on graphene data with first two coordination shells marked.

3.1.2 Wide Angle X-ray Scattering

The X-ray radiation, also known as Roentgen radiation, is a part of the electromagnetic spectrum with the wavelength range from 10 nm to 10 pm. Historically these parameters were chosen to describe the part of the spectrum produced by a moving electron whose energy changes due to collision with an anode (characteristic radiation) or deceleration (bremsstrahlung). Nowadays in science two types of X-ray sources are used: laboratory and synchrotron ones.

Laboratory sources

As the name suggests it is an easily accessible set-up in laboratories as a source of X-rays since synchrotrons are large scale facilities. At the heart of every one is an X-ray tube – a vacuum tube containing two key elements: a cathode and an anode. The cathode is a source of electrons while the anode works as a source of X-rays. The energy can be linked with voltage and wavelength through:

$$E = eV = \frac{hc}{\lambda}, \tag{3.8}$$

where e is the charge of the electron, V is the accelerating voltage, h is the Planck's constant, c is the speed of light and λ is the wavelength. Voltage applied to the tube is important for defining maximum energy loss, and thus minimum wavelength obtained:

$$\lambda = \frac{12.398}{V}[\text{Å, kV}], \tag{3.9}$$

where λ is the wavelength and V is the applied voltage. The continuous part of the spectrum which originates from energy loss due to deceleration of electrons within the anode is called white radiation or bremsstrahlung. Characteristic X-rays are emitted when the incident accelerated electron ejects an inner shell electron and the resulting vacancy is filled by am outer shell electron releasing X-rays in a pattern that is characteristic to each element. Thus, by changing the material of the anode, one can highlight different wavelengths in the spectrum. The electrons emitted in such a process are called Auger electrons. The wavelengths for a couple of elements are compared in Table 3.1.

Table 3.1: Approximate principal emission lines for different kinds of anode target [33].

Anode	Cu	Mo	Cr	Fe	Co	Ag	W
$\lambda(K\alpha)$ [Å]	1.54	0.71	2.29	1.94	1.79	0.56	0.21

Synchrotron light sources

A more rare type of X-ray source is the synchrotron. Synchrotrons are classified as large-scale facilities. There, ultrarelativistic electrons accumulated in a ring emit radiation due to the change in the direction of their movement. As they travel perpendicular to the applied magnetic field, the Lorentz force acts upon them. Synchrotron radiation is highly collimated due to the relativistic effects which narrow the solid angle in which radiation is emitted. Users of synchrotrons have the advantage of a very high flux at the sample as well as wide range of wavelengths available. Due to units usually chosen, the relationship between energy and wavelength can be represented as:

$$\lambda = \frac{12.398}{E}[\text{Å, keV}]. \tag{3.10}$$

The high level of polarization (linear, elliptical or circular) is also accessible. In modern synchrotron facilities radiation is emitted not only in bending magnet regions but also in the straight sections due to the presence of wigglers and/or undulators. Simplifying, both devices force electrons to travel through oscillating paths, and thus to emit radiation. Radiation origination in such devices is even stronger collimated than from a bending magnet, and its intensity is also significantly increased. A great example of such a facility is the European Synchrotron Radiation Facility (ESRF). A few facts about the ESRF are presented in Table 3.2.

The scattering process

Similarly to the case of neutron scattering, X-ray scattering involves a momentum transfer [35, 36]. Here, instead of an interaction of a neutron with a nucleus, a

Table 3.2: A few numbers about the ESRF [34].

storage ring circumference	844 [m]
energy of electrons	6 [GeV]
No. of straight sections	32
No. of curved sections	32
minimum delay between injected bunches	50 [ms]
pre-accelerator length	300 [m]
Horizontal Emittance	4 [nm]
Vertical Emittance	4 [pm]
wavelength – short (range of id15A)	0.016 – 0.41[Å]
wavelength – long (range of id32)	7.7 – 41 [Å]

photon interacts with electrons forming the matter. In the case of WAXS, we are interested in elastic scattering of photons i.e. without any energy loss. As mentioned in Chapter 3.1.1, it is beneficial to make the transition to the Q space, becoming energy/wavelength-independent. Similarly to neutrons, one has to consider how radiation interacts with scattering centres. Here, instead of scattering lengths one uses scattering factors f. The intensity can be described similarly as in (3.4), but instead of (3.5) one has to consider:

$$\frac{\mathrm{d}\sigma}{\mathrm{d}\Omega}(Q) = \left\langle \sum_{i,j}^{N} \overline{f_i f_j^*}\, e^{i\mathbf{Q}\cdot\mathbf{r_{ij}}} \right\rangle \tag{3.11}$$

where: N is the number of scattering centres, $\mathbf{Q}$ is the scattering vector, $\mathbf{r_{ij}}$ represents the relative position of the scattering centres i and j, and f is the scattering factor of carbon.

The structure factor

Apart from the obvious fact that while considering neutron scattering one has to take into account a different type of interaction, a very important role is played by the fact that the f factor is angle-dependent. This makes it crucial to calculate the structure factor for disordered samples. However, as if one considers pure the mono atomic case, there is no longer any inconvenience coming from the fact that there are different atomic isotopes within the sample and the structure factor can be simplified to:

$$S(Q) = \frac{I(Q)}{f^2} \tag{3.12}$$

where $I(Q)$ is the corrected, normalised intensity and f is the scattering factor for carbon.

The pair distribution function

Since (3.7) is calculated from $S(Q)$ only and the structure factor is independent of the technique involved, the function is calculated exactly in the same way as for neutron's case.

3.1.3 High Resolution Transmission Electron Microscopy

In order to bypass the limitations of visible light microscopy one can use a different wavelength. Since electron's de Broglie wavelength is shorter than visible light it can be used to observe much smaller objects. With electron's energy of 54 MeV, its wavelength is of the order of 1.7 Å The electron's wavelength can be linked with voltage V used to accelerate it through the following formula, in which relativistic corrections need to be taken into account due to voltages used in *TEM*:

$$\lambda = \frac{h}{\sqrt{2m_0eV\left(1 + \frac{eV}{2m_0c^2}\right)}} \tag{3.13}$$

where h is Planck's constant, m_0 is the rest mass of the electron, e is its charge and V is the accelerating voltage.

A *TEM* image is created when an electron beam passes through an extremely thin sample, interacts with it, and subsequently is recorded. A wolfram filament is frequently used as a source of electrons. CCD cameras are nowadays commonly used, however fluorescent screens and photographic film are still in use. It is important to remember, that however alluring it may seem, increasing the energy of electrons carries a risk of damaging and/or changing the structure of the sample. Even though it is a difficult task and top-notch equipment is needed, images can be obtained at atomic resolution [21].

Various phenomena lay behind the contrast of the *TEM* image [37]. One of most utilized modes of operation is the bright field imagining mode. The image is created directly by the loss of electrons passing through. In this mode brighter places correspond to less dense regions of the sample. As a first order approximation, the image can be deciphered with Beer's law [38] as a two dimensional projection of the sample down the optic axis. Almost a negative of this image is one obtained in dark field mode. There, the image is created from scattered electrons so that brighter spots correspond to places where the scattering process was stronger. In high resolution *TEM* images the phase contrast originating in the interference of the electron wave plays an important role. *TEM* measurement can be coupled with other techniques such as electron energy loss spectroscopy, electron diffraction or Auger electron spectroscopy.

3.1.4 Raman spectroscopy

Raman scattering

One way to explain the phenomenon of Raman scattering is through quantum mechanics. To put it simply, a Raman scattering is an event of an inelastic photon scattering. This can be obtained in two ways – a photon can either gain or lose energy.

While a molecule is in the ground state, it can be excited by a photon to a virtual state and then a photon can be emitted leaving the molecule in an excited state. This event results in the so called Stokes Raman scattering. The emitted energy is equal to the energy of the scattered photon minus the difference between the energies of the ground and excited states.

Otherwise, the molecule is already in an excited state and by absorbing the photon and emitting one, it returns to the ground state. This event is called the Anti-Stokes Raman scattering. In this case the energy of the emitted photon is equal to the energy of the scattered one plus the difference between energies of the ground and excited state.

Both situations are shown in Figure 3.3 along with a case of Rayleigh scattering where the emitted photon is of the same energy as the absorbed one.

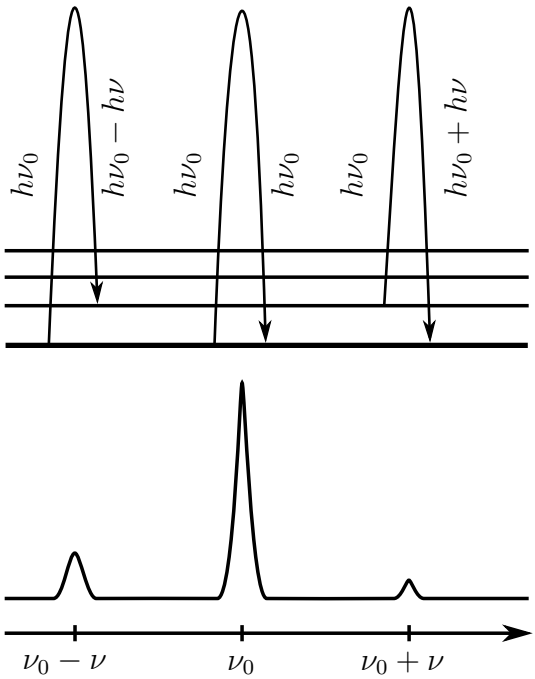

Figure 3.3: Stokes, Rayleigh and Anti-Stokes scattering.

The Raman scattering is only observed when:

$$\left(\frac{d\alpha}{dq}\right)_{q=0} \neq 0 \tag{3.14}$$

which forces the changes in polarization with normal coordinates. As changes in polarization are necessary in order to observe Raman scattering one can employ Placzek's polarization theorem. It is applicable for visible light frequencies. The polarizability of a molecule (α) is related to the induced dipole moment caused by electromagnetic radiation. It can be calculated as:

$$\mu_{ind} = \alpha E_0 \cos 2\pi\nu_0 t \tag{3.15}$$

In order to obtain α there is a need to expand it in a Maclaurin series as a function of the normal coordinate q.

$$\alpha(q) = \alpha_{q=0} + \left(\frac{d\alpha}{dq}\right)_{q=0} q + \left(\frac{d^2\alpha}{dq^2}\right)_{q=0} q^2 + ... \tag{3.16}$$

q is given by:

$$q = A\cos 2\pi\nu t \tag{3.17}$$

Limiting ourselves to only the first 2 terms of the Maclaurin series we get:

$$\alpha(q) = \alpha_0 + \left(\frac{d\alpha}{dq}\right)_{q=0} A\cos 2\pi\nu t \tag{3.18}$$

If we combine it with the formula for the induced dipole we will get:

$$\mu_{ind} = \alpha_0 E_0 \cos 2\pi\nu_0 t + \left(\frac{d\alpha}{dq}\right)_{q=0} AE_0 \cos 2\pi\nu_0 t \cos 2\pi\nu t \tag{3.19}$$

It can be shown that:

$$\mu_{ind} = \alpha_0 E_0 \cos 2\pi\nu_0 t + \frac{1}{2}\left(\frac{d\alpha}{dq}\right)_{q=0} AE_0 \cos 2\pi t(\nu_0 - \nu) + \frac{1}{2}\left(\frac{d\alpha}{dq}\right)_{q=0} AE_0 \cos 2\pi t(\nu_0 + \nu) \tag{3.20}$$

The last equation describes the Raman scattering process:

- ν_0 is the frequency of the original electromagnetic wave – Rayleigh's scattering (elastic),
- $\nu_0 - \nu$ is the frequency of a Stokes electromagnetic wave,
- $\nu_0 + \nu$ is the frequency of an anti-Stokes electromagnetic wave.

The intensity of the Stokes band is about 1000 times lower than the Rayleigh's one.

By engaging Raman scattering as an experimental technique one can gain information about vibrational, rotational, and other low-frequency modes in a system. Through this information one can speculate about the structure of the investigated sample by either comparing obtained spectra to theoretical calculations or by comparing to previously obtained data.

Case of carbon

In Raman spectroscopy of graphitic materials there are two main observable modes (first order) Graphitic – G and Disorder – D [39, 40]. In a perfect graphite crystal only the G mode remains active. When disorder is introduced to the structure, whether in the form of defects or a finite crystallite size, the D mode becomes active. The G mode in graphite is localized near 1581 cm^{-1} and has E_{2g} symmetry, while the D mode is around 1355 cm^{-1}. The latter is a breathing mode of A_{1g} symmetry. Both modes are visualised in Figure 3.4.

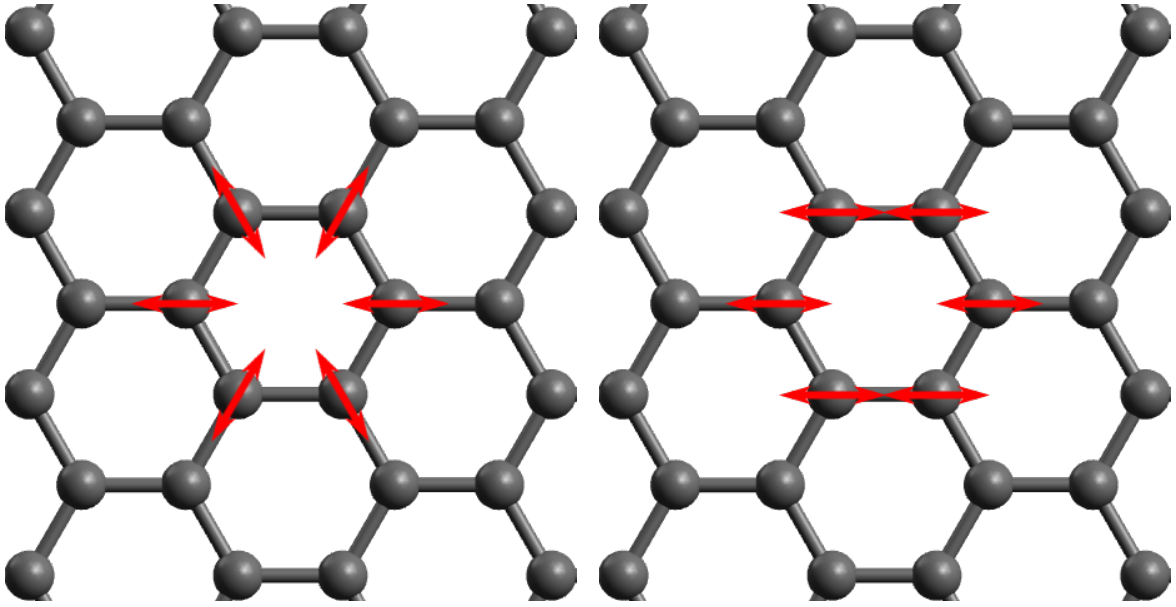

A_{1g} D mode E_{2g} G mode

Figure 3.4: Visualisation of Raman D and G modes. D mode is a breathing one, while in G mode the neighbouring atoms in chains oscillate in opposite directions.

Tuinstra and Koenig [39] showed that the ratio of the intensities of these two modes can be linked with the inverse of the crystallite size along the basal plane (L_a), taking into account an empirical constant dependent on the wavelength used ($C(\lambda)$):

$$\frac{I(D)}{I(G)} = \frac{C(\lambda)}{L_a} \tag{3.21}$$

The empirical constant for $\lambda = 514$ nm is equal to $C(\lambda) = 4.4$ nm [39, 41, 42].

In highly disordered systems additional modes can be observed [43–45]. Those include: $D' \sim 1620$ cm^{-1} $D'' \sim 1500$ cm^{-1} and $D''' \sim 1180$ cm^{-1},

3.2 Computer simulations

In order to extract valuable structural information from $S(Q)$ and PDFs atomic models were computer-generated [46–49]. Comparison of the model-based simulation with the experimental data will be used as a tool for checking the model validity.

3.2.1 Microcrystalline model

The microcrystalline model is the simplest explanation one can find as a reason behind the broadening of the measured peaks in the diffractogram. It is a small cut from the perfect crystal of the investigated material. In case of this work graphitic structure is assumed.

3.2.2 Turbostratic model

As the name suggests, the turbostratic model represents the atomic arrangement in turbostratic carbon as described in Chapter 2.1.2. It is similar to that of graphite, however without stacking order. The correlation between layers within the structure can be broken through translation and/or rotation of the consecutive layers. This makes it possible to test if there is a need for additional distortion within the honeycomb lattice.

3.2.3 Paracrystalline model

Drawing a clear line between liquids, amorphous materials and crystalline matter even though tempting, is impossible. On the borderline between those two worlds, the paracrystalline model was introduced. In the paracrystalline model one softens the constraints existing on lattice vectors, introducing them in a way into a distribution, so they can vary a bit. Each cell vector $\mathbf{a_i}$ gets its own distribution function $H_i(x)$, which represents the probability of $a_i = x$. By representing it in terms of basis vectors $\mathbf{a_i}$ we can introduce the relative distortion factor g_{ik} (3.22) [50, 51].

$$g_{ik} = \frac{\Delta a_{ik}}{a_k} \tag{3.22}$$

Table 3.3: Microparacrystals constituting an intermediate stage between crystalline and amorphous materials [50].

Microparacrystal	g[%]
Crystals	0
Ammonia catalysts	1
So-called „single crystals" of polymers	2
Bulk polymers, biopolymers	3
Graphite of tar coal	6
SiO_2 glass	12
Molten metals	15
Boltzmann gas	100

Δa_{ik} represents the statistical deviation of the lattice constant a_k from its "average" value in the direction of i^{th} axis ($i = 1, 2, 3$). The paracrystalline distortion can be also specified by the factor g_{hkl} related to the statistical changes of the inter-planar distance d_{hkl} between the neighbouring netplanes as:

$$g_{hkl} = \sqrt{\frac{\overline{d_{hkl}^2}}{\overline{d}_{hkl}^2} - 1} \tag{3.23}$$

where the overlines indicate the statistical average.

Naturally when all $g_{ik} = 0$ we are back to a perfect, undisturbed crystal.

A range of exemplary values of g is shown in Table 3.3.

Disorder within a paracrystal propagates with the square root of distance. It can be expressed with a standard deviation of the inter-atomic distances σ_{ij} defined as:

$$\sigma_{ij} = \sigma_0 \sqrt{r_{ij}} \tag{3.24}$$

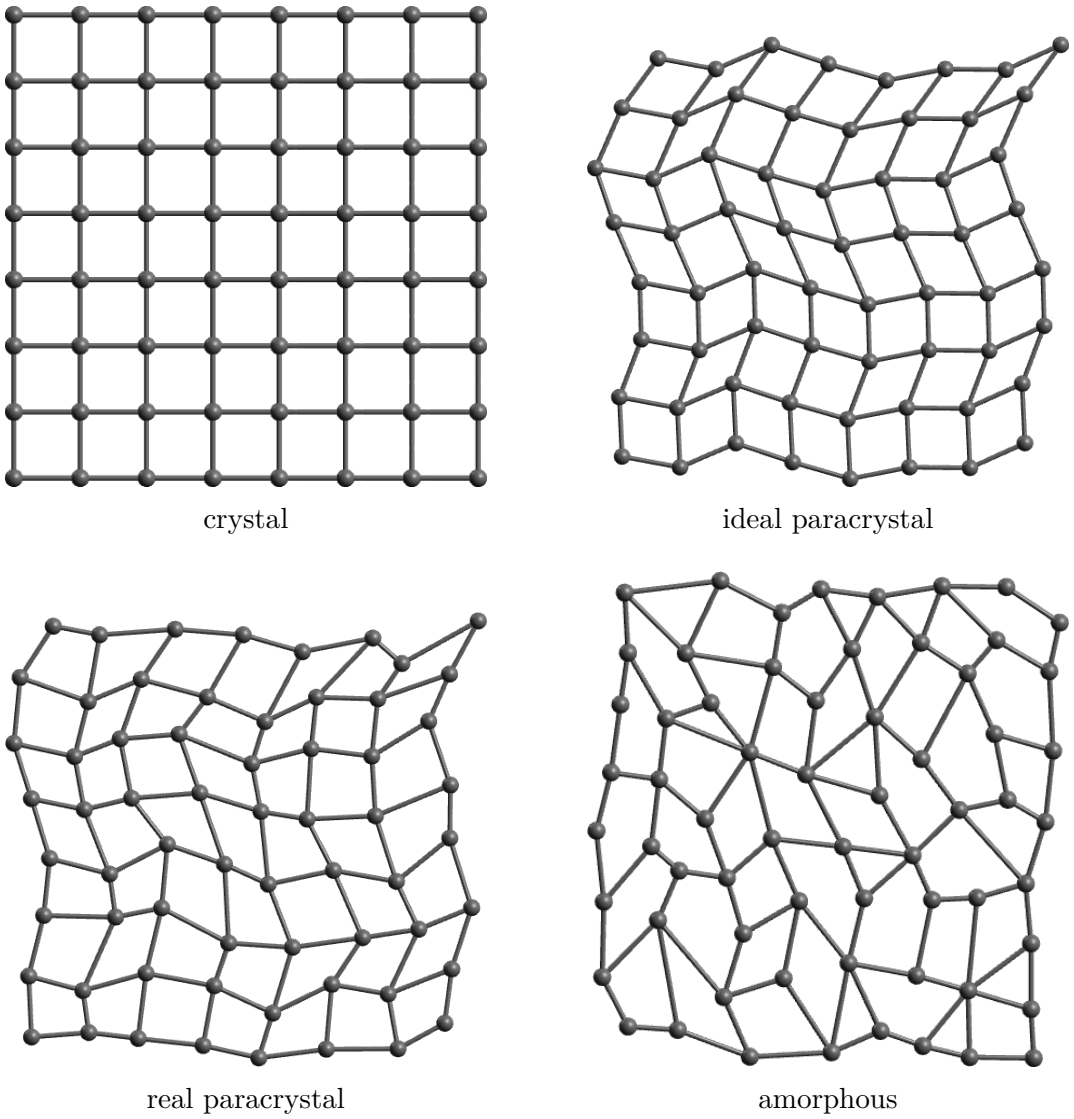

Figure 3.5: Schematic representation of different types of point lattice in two dimensions.

where r_{ij} is the distance between the i^{th} and the j^{th} atoms.

Visually, differences between crystal, ideal and real paracrystal, and an amorphous 2D lattice are easily spotted (see Figure 3.5).

In an ideal paracrystal the degree of order is only slightly bent from one in a crystal. Cells are arranged in rows, they are parallelepiped-shaped, they are however not repeatable. In a real paracrystal we lose yet another degree of order, yet cells are still somehow ordered in rows, while looking for order in an amorphous material seems like a lost cause.

3.2.4 Molecular dynamics

With the development of more and more powerful computing machines computational methods thrived. At the time of its invention the paracrystalline model had a huge advantage as it was possible to calculate $I(Q)$ directly with a simple method requiring just pen and paper (and a brilliant mind along). Its main disadvantage is the lack of a firm physical origin of the introduced disorder. With more computational power available, Molecular Dynamics simulations are a useful tool in obtaining models – atomic positions of real systems. They are not ideal – they were calculated with some simplifications, however we are still limited by available computing power and those simplifications allow us to bypass it and increase the simulation's length and/or the number of simulated atoms. In MD one does not go as deep as quantum mechanics, but calculates interactions between given atoms using Newtonian equations. In order to calculate forces between interacting atoms one has to assume a form of a potential. In this work two are used: the Lennard-Jones potential and the second generation of Reactive Empirical Bond Order (*REBO2*) [52]. The first one is responsible for interactions between atoms laying within two consecutive layers. *REBO2* describes behaviour of atoms laying within the same honeycomb carbon layer.

Potentials used

Lennard-Jones potential is also sometimes refereed to as the 6-12 potential based on its exponents. Its named after John Lennard-Jones by whom it was first proposed. It describes the interaction between a pair of neutral objects. It can be written as:

$$V_{LJ} = 4\epsilon \left[\left(\frac{\sigma}{r} \right)^{12} - \left(\frac{\sigma}{r} \right)^{6} \right] \tag{3.25}$$

where ϵ is the depth of the potential well the σ stands for its diameter and r represents the distance between given particles. The first term accounts for short range repulsive behaviour while the second one represents attraction over longer distances.

***REBO2* potential** This potential, while still very efficient, performs much better than the Lennard-Jones potential when describing covalent bonded atoms. Tersoff [53–55]

basing on works of Abell [56] had a first "try" at *REBO* potential introducing an energy function for multi-body systems, where energy is calculated based on atom surroundings and only for nearest neighbours. This potential accurately describes single, double and triple bonds in carbon systems. In order to improve accuracy when dealing with influence of valence angles and predictions of deformation of systems Brenner [57] introduced the second generation of *REBO* potential. In his work he included efforts put into another version of *REBO* potential – *AIRREBO* created by Stuart [58]. Considering the *REBO2* potential one can describe the binding energy of two carbon atoms as:

$$E_b = \sum_i \sum_{j>i} f_c(r_{ij})[V_R(r_{ij}) - b_{ij} V_A(r_{ij})], \tag{3.26}$$

where r_{ij} is the distance between i^{th} and j^{th} atom, and $f_c(r_{ij}) = \begin{cases} 1 & \text{for the nearest neighbours} \\ 0 & \text{for others} \end{cases}$ is the switching function. The $V_R(r_{ij})$ is responsible for inter-atomic repulsion coming from from valence electrons and $V_A(r_{ij})$ accounts for the attractive interaction. The b_{ij} describes the bond order function depending on local surroundings of the atom – its coordination and the bond angles. Thanks to that the *REBO2* potential leads to a realistic description of the bond lengths of the carbon-carbon bonds, both single and multiple ones.

Considered defects

All considered structural defects were point type defects (0 dimensional).

The mono vacancy The mono vacancy [59] is the simplest type of defect – one atom is missing. As a result, in a honeycomb lattice one nonagon and one pentagon forms. Its energy of formation $E_f \approx 7.5\,\text{eV}$ and the migration barrier is about 1.3 eV [60]. The graphical representation is shown in Figure 3.6a.

The di vacancy In a di vacancy [59, 61] two atoms are missing forcing two pentagons and one octagon to appear in the lattice. Its energy of formation is approximately $E_f \approx 8\,\text{eV}$ [60]. The graphical representation is shown in Figure 3.6b.

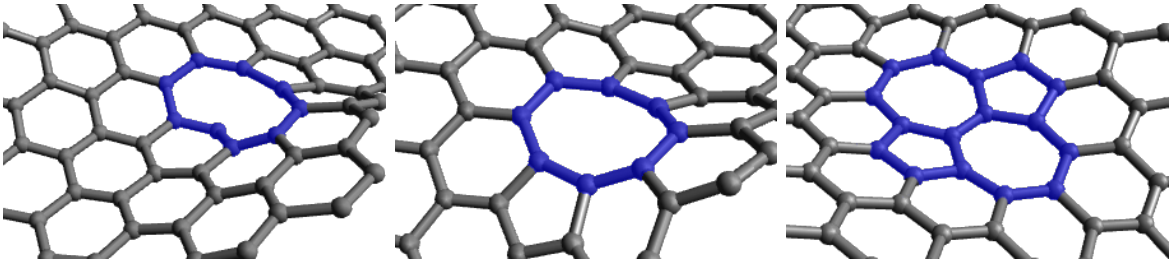

(a) Mono vacancy (b) Di vacancy (c) STW

Figure 3.6: Different types of defects (outlined in blue).

The Stone-Thrower-Wales The Stone-Thrower-Wales type of defect [62–64] needs one rotated C-C bond to occur. Rotation by 90° leads to the appearance of two pentagons and two heptagons within lattice. Its formation energy is around $E_f \approx 5\,\text{eV}$ [60]. The graphical representation is shown in Figure 3.6c.

4 Results and discussion

4.1 General description

4.1.1 Experimental details

Wide Angle Neutron Scattering

The measurements were carried out at the Institute Laue-Langevin in Grenoble, France. The D4 diffractometer dedicated for liquids and amorphous materials [65] was used. The D4 is especially well suited for such tasks as it has a wide 2θ range, uses hot neutrons, and collimation before detectors ensures extremely low background. Schematics for the diffractometer are presented in Figure 4.1. A closed vanadium can of $\phi = 7$ mm was used as a sample holder. Measurements were performed under ambient temperature and under vacuum conditions. The wavelength used in the experiment was $\lambda = 0.4975$ Å. The 2θ range of the diffractometer along with the used λ allowed to obtain $Q_{max} = 23.5\,[\text{Å}^{-1}]$. The $Cu\,220$ face of the monochromator and a Rh $\lambda/2$ filter were used. For the beam collimation a pair of slits were set: a horizontal one – 13 mm, and a vertical one – 50 mm. For the purpose of the data treatment, measurements of an empty belljar and an empty can were carried out. Later on they were used to subtract the background from the sample. Using the measured packing fraction and a recorded vanadium rod diffraction pattern, the sample's diffraction intensity was normalised to an absolute scale. Additionally, multiple scattering and absorption corrections were used throughout the data analysis. In order to do so, the CORRECT program was employed [66].

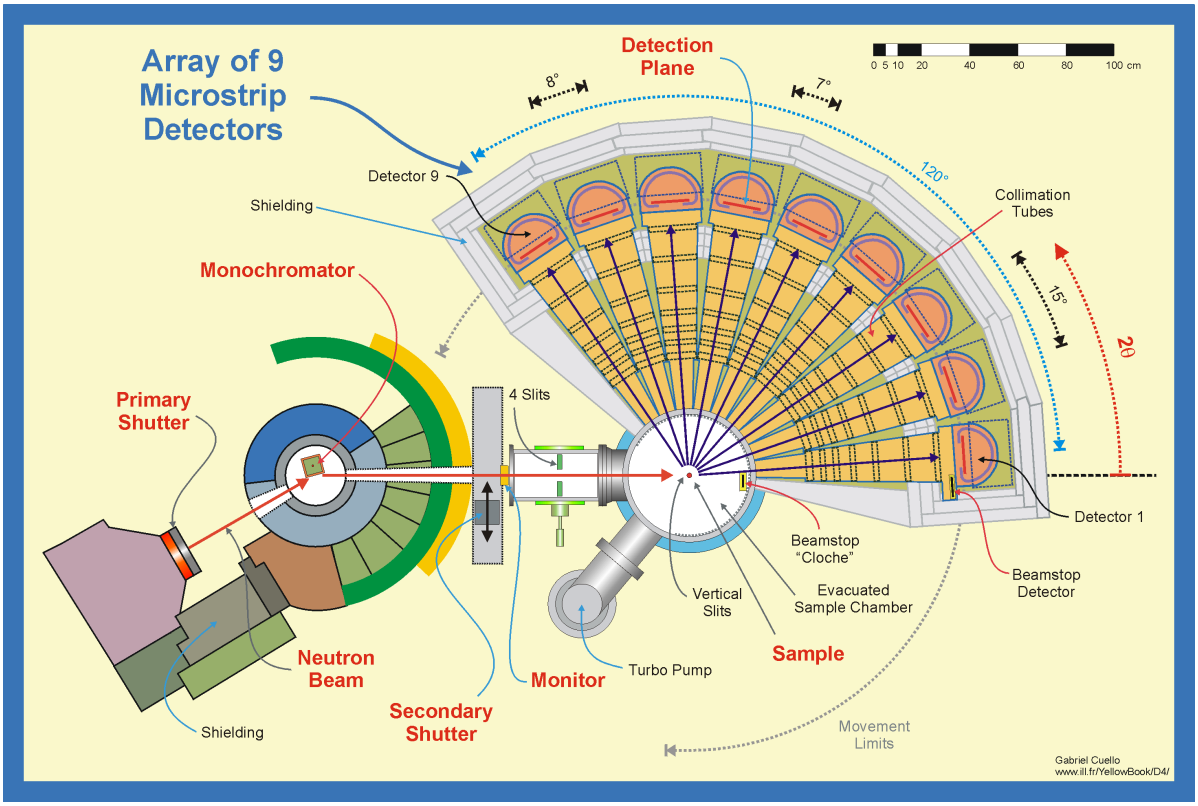

Figure 4.1: Schematics of the D4 diffractometer [65].

Wide Angle X-ray Scattering

Most of the Wide Angle X-ray diffraction data was obtained using a synchrotron source, however for the graphene sample a laboratory source was used.

The synchrotron The WAXS experiment using synchrotron radiation was performed at the ESRF in Grenoble, France. Measurements were performed at High-Energy X-ray Beamline – ID15B. They were done under ambient conditions while the samples were held in glass capillaries 2 mm. The beam energy was 86 keV, which along with a 2D flat MAR detector resulted in $Q_{max} = 21$ Å^{-1}. In order to reduce low energy fluorescence background, an Al plate was placed in front of the detector. For proper data treatment measurements of an empty capillary were carried out and subsequently subtracted from the measured data for the investigated samples. The obtained data was properly normalised and corrected according to the procedure developed for high-energy X-rays.

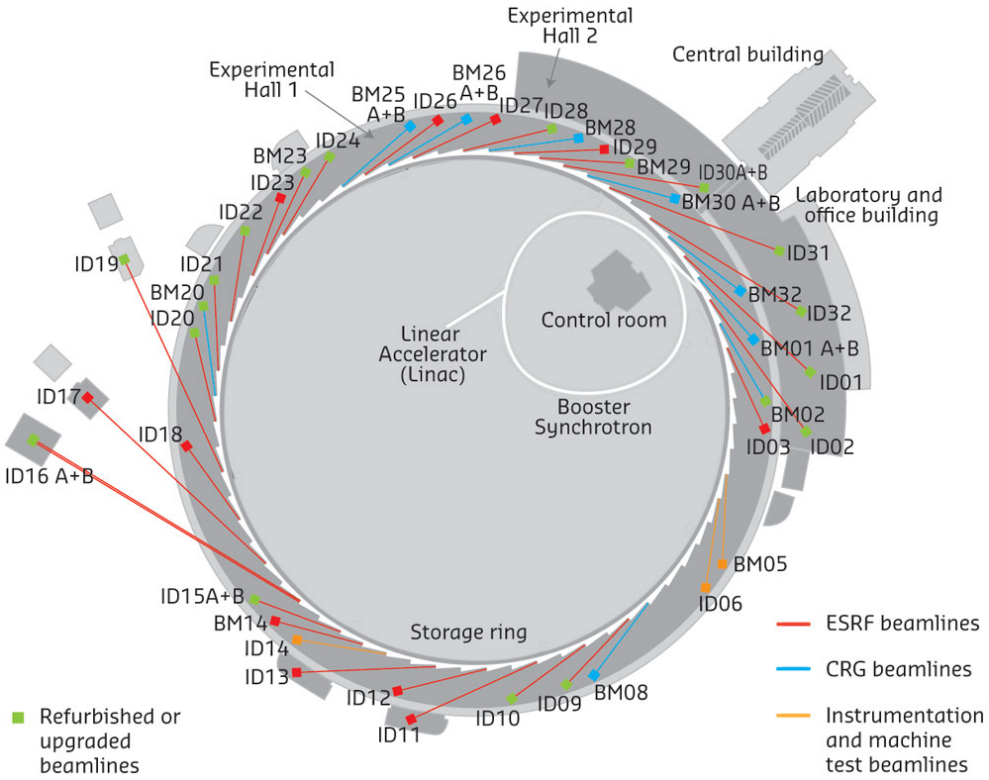

Figure 4.2: The beamlines at the ESRF [34]

The laboratory source The diffractometer used in this experiment was the Rigaku-Denki D/MAX RAPID II-R diffractometer Figure 4.3. The most important feature of the diffractometer used, which made it possible to compare the obtained data with the neutron and synchrotron one was the silver rotating anode. The used incident beam was a $Ag\ K\alpha$ tube ($\lambda = 0.5608$ Å). In order to obtain a monochromatic and collimated beam a (002) graphite monochromator was employed so the beam size at the sample was 0.3 mm. Combined with a wide 2θ range it resulted in $Q_{max} = 22\,\text{Å}^{-1}$. An image plate in the Debye-Scherrer geometry was used as a detector. The measurements were performed at room temperature and ambient pressure. A glass capillary (1.5 mm in diameter and 0.01 mm wall thickness) was the sample holder in this experiment. For background subtraction, a diffractogram of an empty capillary was collected. In order to convert two-dimensional diffraction patterns to diffractograms, software provided by Rigaku-Denki was used. The obtained intensity plots were properly corrected and normalized according to the procedure developed for high-energy X-rays.

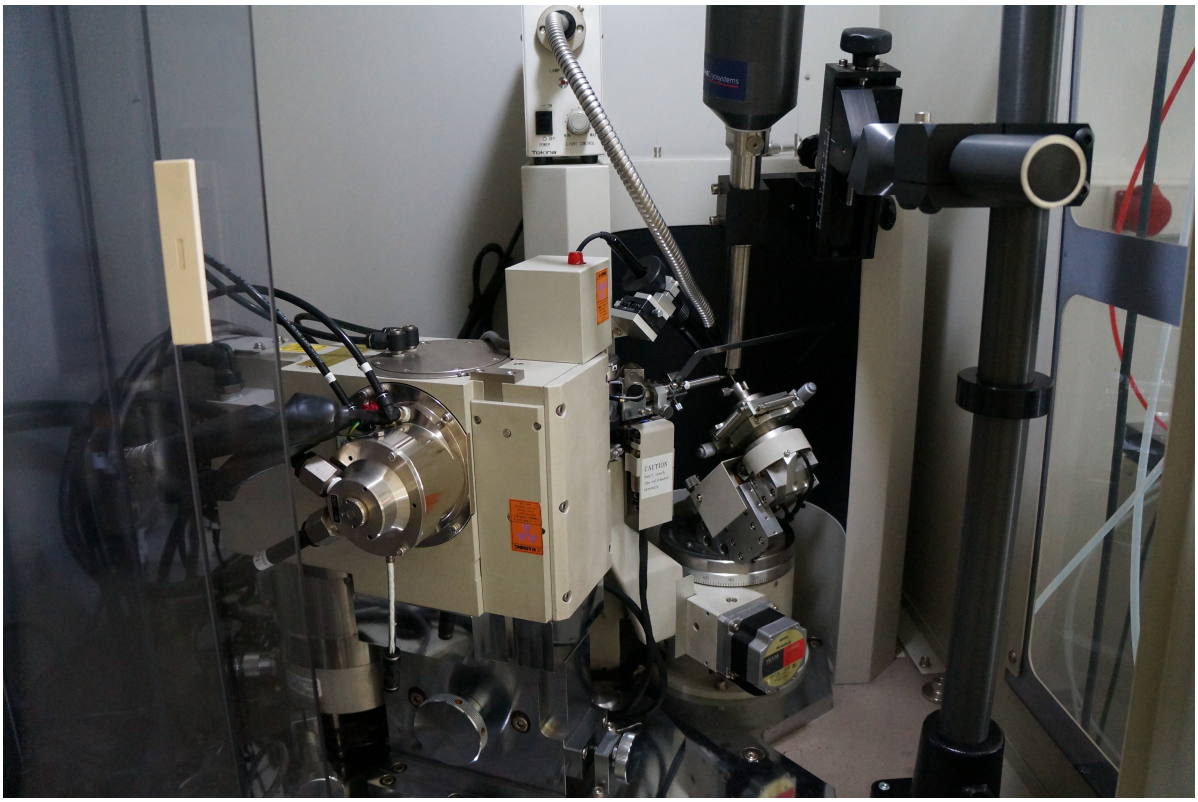

Figure 4.3: The diffractometer Rigaku-Denki D/MAX RAPID II-R.

High Resolution Transmission Electron Microscopy

For the HRTEM measurements samples were prepared by grinding them into fine powder and then mixed with ethanol in order to create a suspension to disperse onto amorphous carbon meshes. The HRTEM images were taken using a high resolution transmission electron microscope S/TEM TITAN 80-300.

Raman spectroscopy

The experiment was carried out at Universite du Maine in Le Mans. The multichannel Raman spectrometer Jobin-Yvon T64000 in single configuration was used, together with a nitrogen-cooled CCD detector. An argon-krypton laser (Coherent Spectrum) with a $514.5nm$ wavelength served as a light source. The laser power was set to 50 mW, which was previously proven not to cause sample damage. Data was acquired in two 300 s runs.

The background was removed from the acquired data, which was subsequently fitted with a combination of five functions. For consistency, all samples were treated in the same way. The D and G peaks were fitted with Lorentzian shapes while D', D'' and D''' with a Gaussian one. The positions of fitted peaks are gathered in tables in the respective sections of this chapter. Additionally, the D/G ratio is calculated for each measurement. From there, the crystallite size is calculated using (3.21).

4.1.2 Computer simulations

Constructing the best fitting model for the investigated samples was approached in multiple steps, divided in two parts: simple models with arbitrary calculated atom positions, and MD simulations. The first one was to check if the microcrystalline model was suitable and determine a basic set of parameters. Then, if necessary, the turbostratic model was introduced along with some more parameters. The final step (if required) in the first part was to calculate the paracrystalline model. The second part was to translate the findings from the simpler models into ones which accounted for forces acting upon the structure through MD simulations.

As a tool to quantitatively assess the calculated models the discrepancy factor was used. It is defined as:

$$R = \sqrt{\frac{\sum_i \left[PDF_{exp}(r_i) - PDF_{sim}(r_i)\right]^2}{\sum_i \left[PDF_{exp}(r_i)\right]^2}} \cdot 100\%. \tag{4.1}$$

where PDF_{exp} is a function representing the measured data while PDF_{sim} represents the calculated data.

Microcrystalline model

The relatively small size of coherently scattering domains in investigated carbons leads to broadening of diffraction peaks. Therefore in the first step the simulation results based on the microcrystalline graphitic model were compared with the experimental data. This way it is easy to assess if further distortion of the structure, if any, is needed in order to explain the measured diffraction data. The number of layers was chosen in a way to obtain best match for the amplitude of the first diffraction peak. The clue for the lattice parameter c was the position of the same peak, as it is influenced by inter-layer spacing which is half of its value. The models' diameter was assessed based on attenuation of the PDF function. The moment when peaks are no longer detectable corresponds to the longest distances between atoms within the coherently scattering regions. The lattice parameters a and b for a carbon honeycomb structure were used. The standard deviations of atom-atom distance – σ_{intra} and distances between atoms within two different layers – σ_{inter} were chosen to account for thermal movement of atoms away from their intended positions.

Turbostratic model

In the next step it is beneficial to check the turbostratic structure mentioned in Chapter 2.1.2. In this work it is realised by either transitional or rotational distortion of subsequent graphitic planes. The shape of the observed structure factor is very similar to ones presented in [4, 67, 68] with only (002) and (hk) type diffraction lines [69]. The aforementioned broken order along the c axis results in loss of the general (hkl) lines. Even though there are no long range correlations along the c axis, existing spatial

correlations within individual graphitic layers result in the (hk) reflections. Parameters successfully extracted from microcrystalline model are preserved in this one.

Paracrystalline model

After breaking long distance correlation along c axis in the model, next step lead to alternating atom positions within each layer. Moreover, since the paracrystalline model was applied additionally to broken A-B-A-B stacking disorder along the c axis gained a Q^2 dependency. As mentioned in Chapter 3.2.3, it is assumed that the fluctuation of distances between any atom to its nearest-neighbours are statistically independent which leads to the propagation of disorder with $\sqrt{r_{ij}}$. Switching to the reciprocal space it translates to a broadening of the diffraction peaks with increase of width with Q^2 according to [70–76]. The paracrystalline disorder was implemented in the model by the generalized Debaye-Waller factor. The Debaye-Waller factor for intra-layer correlations is defined as: $\sigma_{intra} = \sigma_0\sqrt{r_{ij}}$. In the case of inter-layer correlations it is defined as $\sigma_{inter} = \sigma_1\sqrt{\Delta n}$ where $\Delta n = n_i - n_j$; n_i and n_j labels layer positions in a sequence. Assuming a Gaussian distribution of the inter-layer distances, the structure was generated. For the final structure factor, a number of simulations were performed and their structure factors were averaged. Similarly as in the previous case, the parameters correctly predicted by the microcrystalline model are used in this one.

Molecular Dynamics

In order to establish origins of paracrystalline disorder the presence of topological defects is considered. In this work, point defects, as described in Chapter 3.2.4 are considered as such a source. Based on the results from the paracrystalline model, input models consisting of a Cartesian set of positions of atoms were constructed. Each model contained a different number and/or type of defect. Defects were randomly distributed within the individual layers. Subsequently the energy of each model was optimised using classical molecular dynamics at 300 K. The potentials employed were: the second generation reactive empirical bond order (*REBO2*) potential [57] for atoms lying in the same layer and the Lennard-Jones potential for inter-layer interactions [77]. Using

these potentials, forces were calculated in order to solve the Newtonian equations of motion. The predictor-corrector method was used with 10^5 time steps of 0.2 fs. The Berendsen [78] thermostat was used to stabilize temperature in the system. Considering the nature of simulations, the periodic boundary conditions were not needed in order to properly to reproduce edges of the system.

4.2 Graphene

4.2.1 Experimental measurements

Wide Angle Scattering data

Data for the graphene sample was acquired both with neutrons and a laboratory source. Both Figure 4.4 and Figure 4.5 show that acquired data is of good quality and in agreement between both techniques. The slight differences can be attributed e.g. to different spatial resolution of both diffractometers, calibration or the nature of the interaction of the probe with matter resulting in different data treatment. The peak positions are in excellent agreement despite these minor issues. Further analysis of the data is presented in Chapter 4.2.2.

High Resolution Transmission Electron Microscopy

In Figure 4.6, a few obtained images are presented. They show a very thin, slightly crumpled system. The curved surfaces are noticeable on images with higher magnification rates – Figure 4.6a and Figure 4.6b. There is no visible inhomogeneity within the sample. It seems to form larger planes of more complicated structure, however just from the pictures it is impossible to speculate about the sample's atomic structure or number of layers. The images are consistent with results obtained with other techniques.

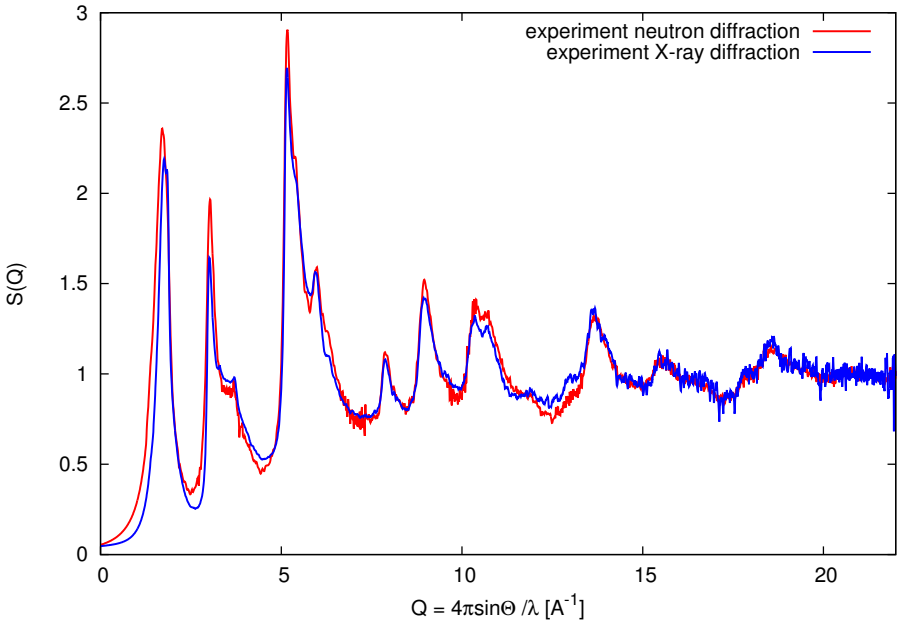

Figure 4.4: Comparison of structural factors for the neutron and X-ray experimental data for the graphene sample.

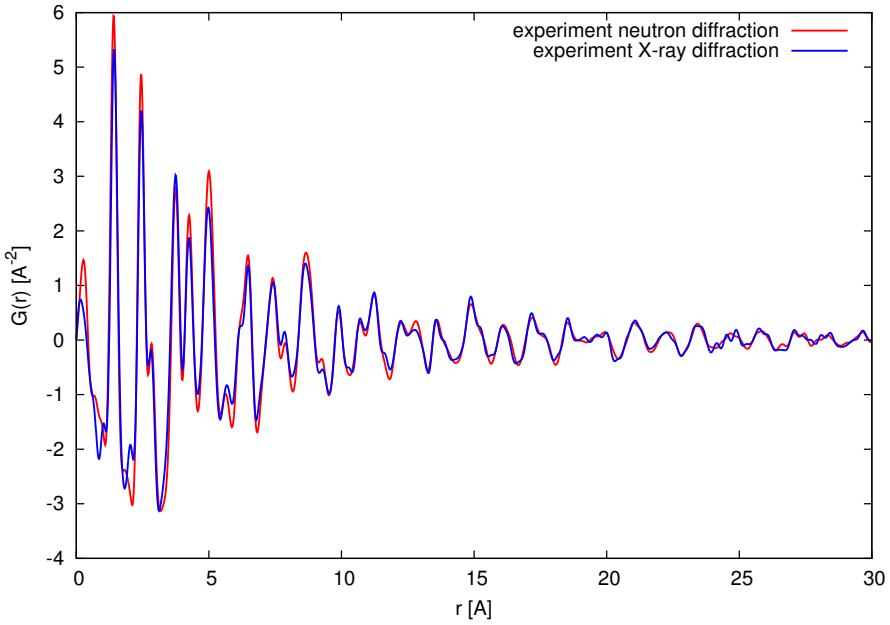

Figure 4.5: Comparison of PDFs for the neutron and X-ray experimental data for the graphene sample.

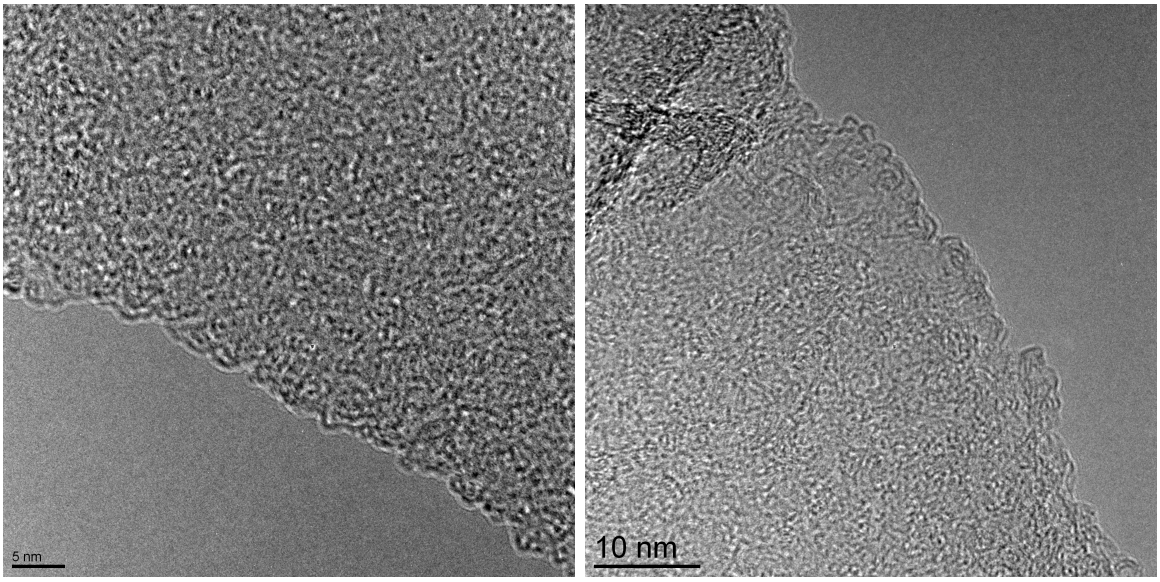

(a) (b)

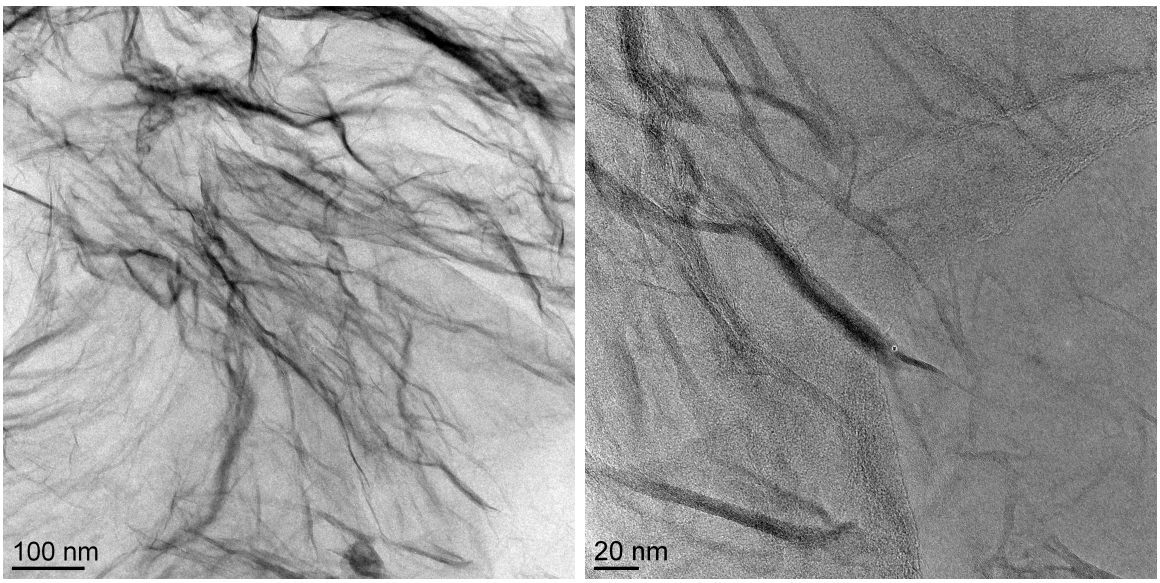

(c) (d)

Figure 4.6: HRTEM images of graphene.

Raman spectroscopy

The measured data is presented in Figure 4.7 while parameters obtained through fitting are gathered in Table 4.1. The gathered data is consistent in measurements from point to point. The position of G and D peaks remains stable, without much of a shift. The D', D'' and D''' display slightly more variation in their positions. The calculated D/G ratio suggests that the sample is homogeneous, which also implies that crystallite size remains stable within the sample.

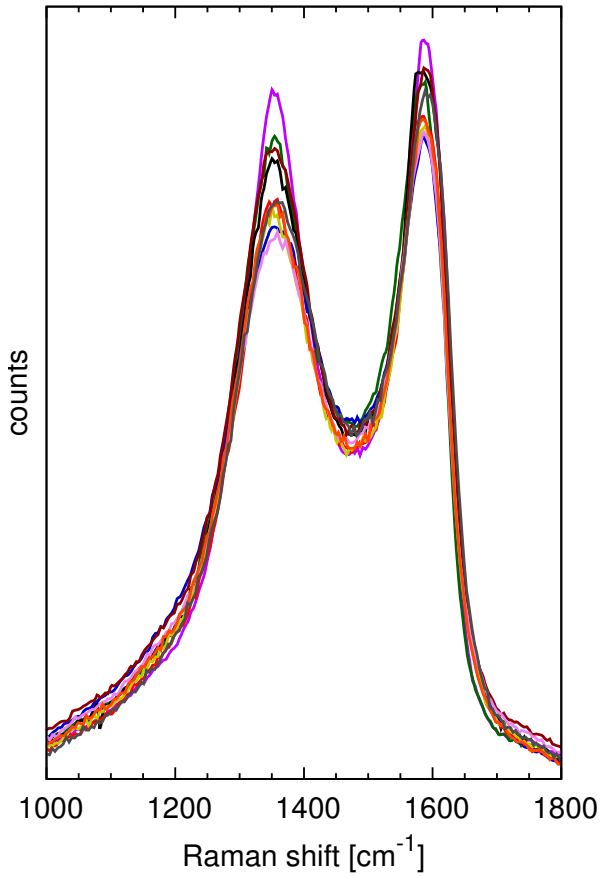

Figure 4.7: Visualisation of Raman scattering by the graphene sample. Data was modified in order to be in the same range in the figure.

Table 4.1: Peak positions, D/G ratio and crystallite size (L_a) for the graphene sample.

	G[cm^{-1}]	D[cm^{-1}]	D'[cm^{-1}]	D''[cm^{-1}]	D'''[cm^{-1}]	D/G	L_a[Å]
1	1582	1353	1614	1505	1190	1.02	43
2	1581	1357	1612	1505	1183	0.98	45
3	1583	1354	1614	1513	1185	1.05	42
4	1583	1355	1613	1507	1185	1.04	42
5	1582	1354	1616	1503	1188	0.99	44
6	1582	1355	1616	1507	1198	1.06	42
7	1582	1354	1616	1503	1185	0.99	44
8	1578	1353	1612	1509	1194	1.11	40
9	1583	1356	1616	1523	1189	1.18	37
10	1583	1353	1614	1505	1195	1.02	43
avg.	**1582**	**1354**	**1614**	**1508**	**1189**	**1.04**	**42**

4.2.2 Computer simulations

Microcrystalline model

The model parameters are gathered in Table 4.2. Both experimental structural factors are compared to the simulated model in the top panel of Figure 4.8, Figure 4.10. The respective *PDFs* are shown on Figure 4.9 and Figure 4.11. This comparison clearly shows that the model based on the perfect graphite structure does not reconstruct the measured data. The computed functions exhibit too much of a structure, which is visible in $S(Q)$ as clearly visible peaks up to $Q = 22$ Å, and in *PDFs* where sharp peaks up to 30 Å are noticeable. It suggests that the microcrystalline model is too ordered and additional disorder should be introduced. This conclusion is further reinforced by the high value of the discrepancy factor R listed in Table 4.6.

Turbostratic model

The model parameters are gathered in Table 4.3. All measured data are compared to the calculated model in: Figure 4.8, Figure 4.10, Figure 4.9 and Figure 4.11. It is important to note at this point that all peak positions can be explained assuming only correlations within the layer. However, their amplitudes remain too high suggesting that the model is still too ordered and the implemented changes in the graphitic structure are not sufficient to account for all features of the experimental data. Just the constant value of the Debye-Waller factor is not enough to account for decay of the amplitude of the experimental structure factors along with increase of their widths with increasing Q. Values of Table 4.6 shows that even though agreement between the calculated model and experimental data is clearly better than in the previous case, it is still unacceptable.

Paracrystalline model

The model parameters are gathered in Table 4.4. The values of the σ_0 and σ_1 parameters were adjusted in order to obtain the best agreement with the experimental data. Figure 4.8, Figure 4.10, Figure 4.9 and Figure 4.11 present a comparison between

Table 4.2: Parameters for microcrystalline model for the graphene sample.

No. of layers	3
ϕ of system	36 Å
lattice parameters a & b	2.456 Å
lattice parameter c	7.0 Å
σ_{intra}	0.03 Å
σ_{inter}	0.03 Å

Table 4.3: Parameters for turbostratic model for the graphene sample.

No. of layers	3
ϕ of system	36 Å
lattice parameters a & b	2.456 Å
lattice parameter c	7.0 Å
range of rotation angles	0^o-30^o
σ_{intra}	0.03 Å
σ_{inter}	0.03 Å

Table 4.4: Parameters for paracrystalline model for the graphene sample.

No. of layers	3
ϕ of system	36 Å
lattice parameters a & b	2.456 Å
lattice parameter c	7.0 Å
range of rotation angles	0^o-30^o
σ_0	0.045 Å
σ_1	0.05 Å
No. of averaged structures	100

the calculated and measured data. The figures are respectively: $S(Q)_{neutrons}$, $S(Q)_{X-ray}$, $PDF_{neutrons}$, and PDF_{X-ray}. In comparison to previous models, it is clearly visible that the paracrystalline model reconstructs the measured data more accurately. The R factor follows the improvements visible in the above figures. Its values are gathered in Table 4.6.

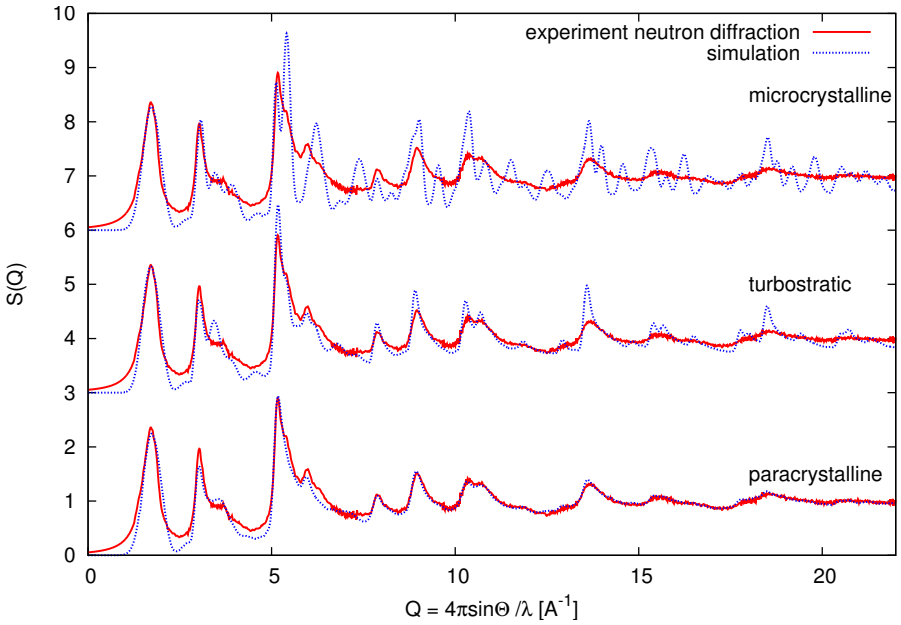

Figure 4.8: Comparison of the structural factors for: paracrystalline, turbostratic and microcrystalline models with the neutron experimental data for the graphene sample.

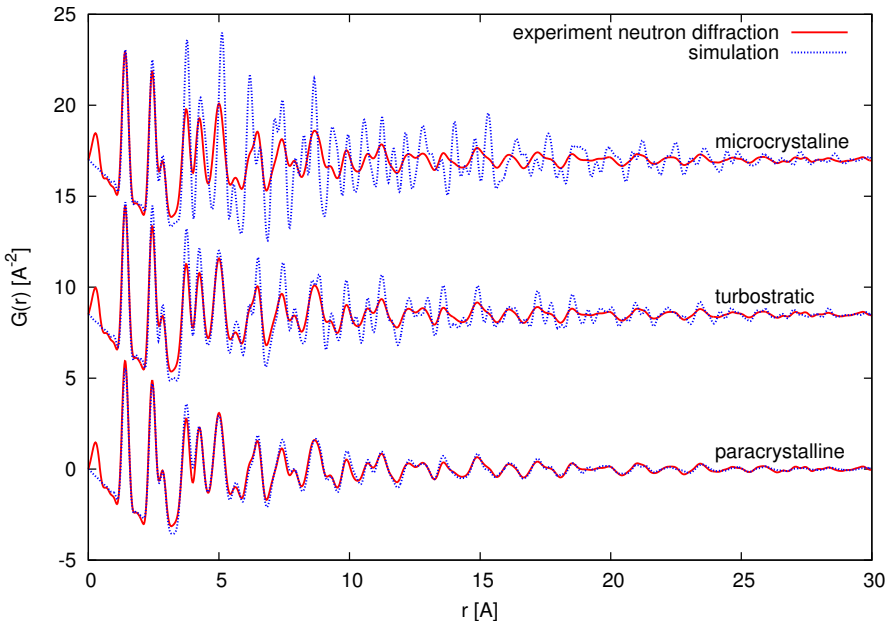

Figure 4.9: Comparison of the PDFs for: paracrystalline, turbostratic and microcrystalline models with the neutron experimental data for the graphene sample.

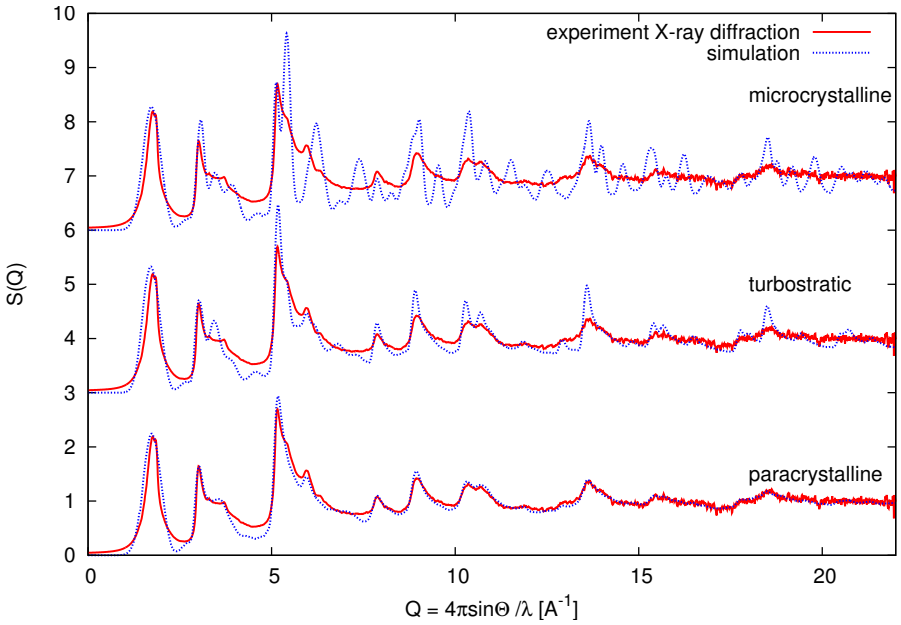

Figure 4.10: Comparison of the structural factors for: paracrystalline, turbostratic and microcrystalline models with the X-ray experimental data for the graphene sample.

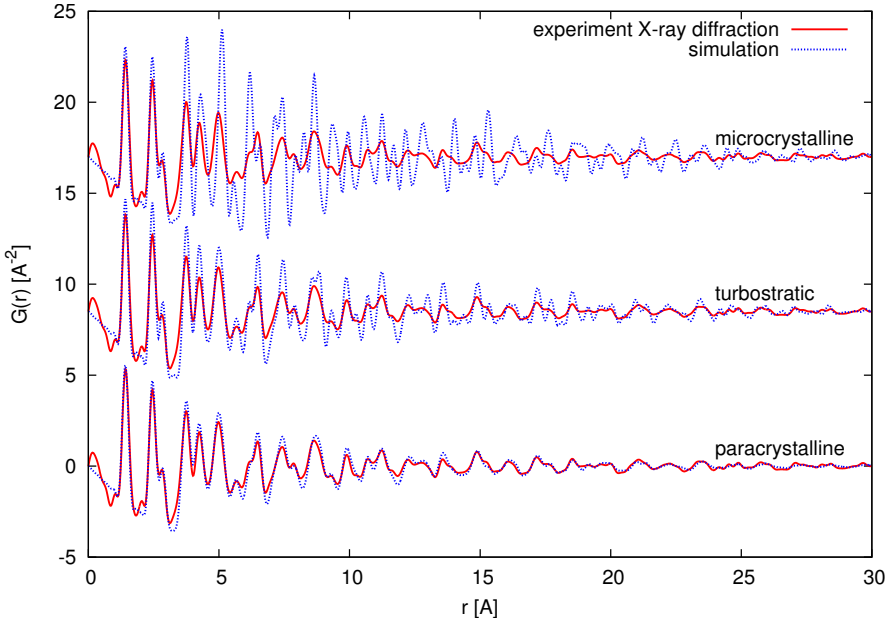

Figure 4.11: Comparison of the PDFs for: paracrystalline, turbostratic and microcrystalline models with the X-ray experimental data for the graphene sample.

Molecular dynamics

The model parameters are gathered in Table 4.5. The $S(Q)$ calculated for all considered defects are presented in Figure 4.12 – for neutrons and Figure 4.14 – for X-rays. The *PDFs* are presented in Figure 4.13 and Figure 4.15 in the same order. Based on these plots one can conclude that the proposed models reconstruct all key experimental features over all $S(Q)$ and *PDFs*. Taking into consideration values presented in Table 4.6 one can assume that the model with di-vacancy defects is favourable as it has the lowest value of the discrepancy factor. The di-vacancies are preferred both for X-ray scattering data and for neutron ones. There is a difference in calculated values of R for X-ray data and neutron data, which can be explained by slight differences between both sets of data, the lower values for neutron data could arise from better statistics of the dataset. The insets in Figure 4.13 show the distributions of the C-C bond lengths in the constructed models. These histograms show that the randomly introduced defects cause paracrystalline-like distortion of the model structure. In comparison to the graphitic 1.42 Å nearest-neighbour inter-atomic distance, one can observe the appearance of shorter and longer C-C bonds. The presence of non-hexagonal rings in the structure can explain their origin – single (longer) and double (shorter) C-C bonds. Those defects are also responsible for the curvature of the graphene layers, visible in Figure 4.16, where the final model with the di-vacancy defects is displayed.

Table 4.5: The parameters for MD model for the graphene sample.

No. of layers	3
ϕ of system	36 Å
No. of mono-vacancies per layer	5
No. of di-vacancies per layer	3
No. of STW type of defect per layer	$2^1/_3$

Table 4.6: Discrepancy factors between models and experimental data for the graphene sample.

model	R_{x-ray}	$R_{neutrons}$
microcrystalline	127.5%	110.2%
turbostratic	61.4%	48.7%
paracrystalline	28.8%	20.3%
mono-vacancy	28.5%	19.5%
di-vacancy	27.9%	18.6%
STW type defect	30.9%	22.4%

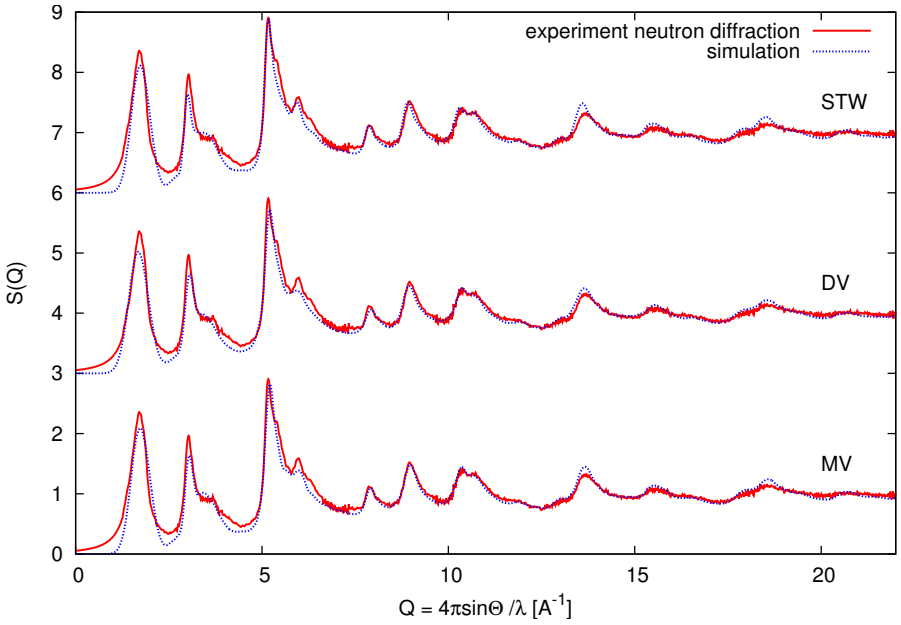

Figure 4.12: Comparison of the structural factors for theoretical models containing: mono-, di- vacancies and STW type defects with the neutron experimental data for the graphene sample.

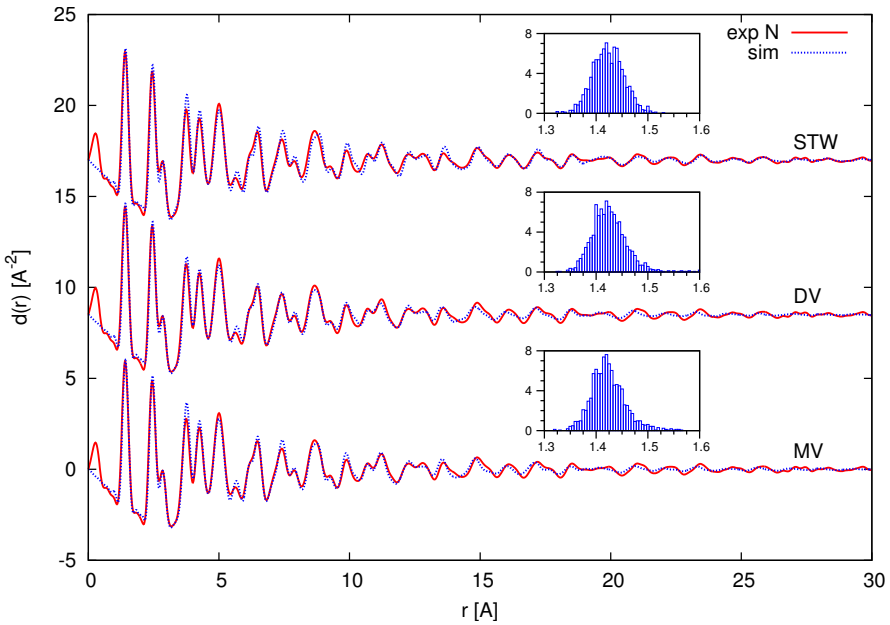

Figure 4.13: Comparison of the PDFs for theoretical models containing: mono-, di-vacancies and STW type defects with the neutron experimental data for the graphene sample. Along each PDF there is histogram plot embedded. The X axis shows C-C bond length [Å], while Y axis distribution of C-C bond length [%].

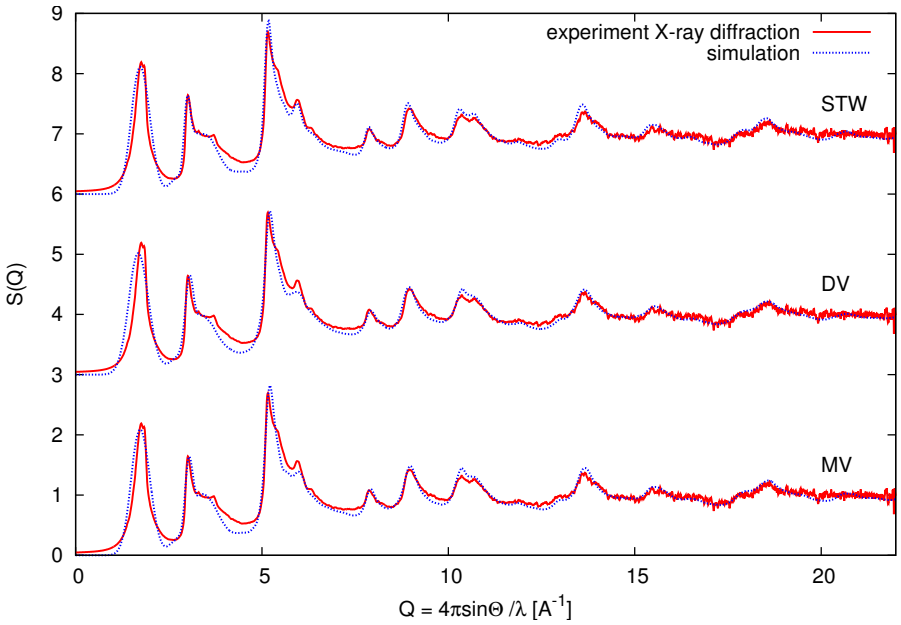

Figure 4.14: Comparison of the structural factors for theoretical models containing: mono-, di- vacancies and STW type defects with the X-ray experimental data for the graphene sample.

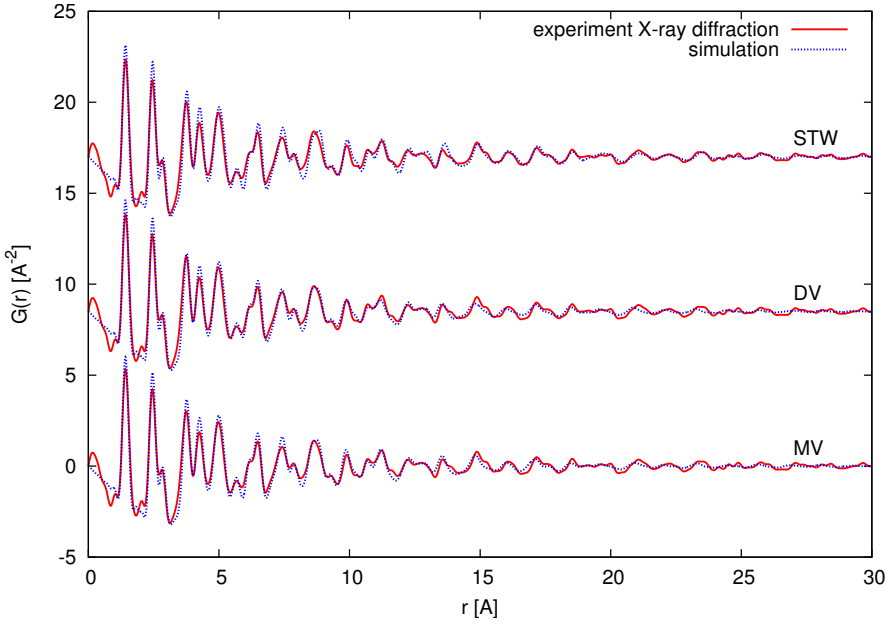

Figure 4.15: Comparison of the PDFs for theoretical models containing: mono- and di-vacancies and STW type defects with the X-ray experimental data for the graphene sample.

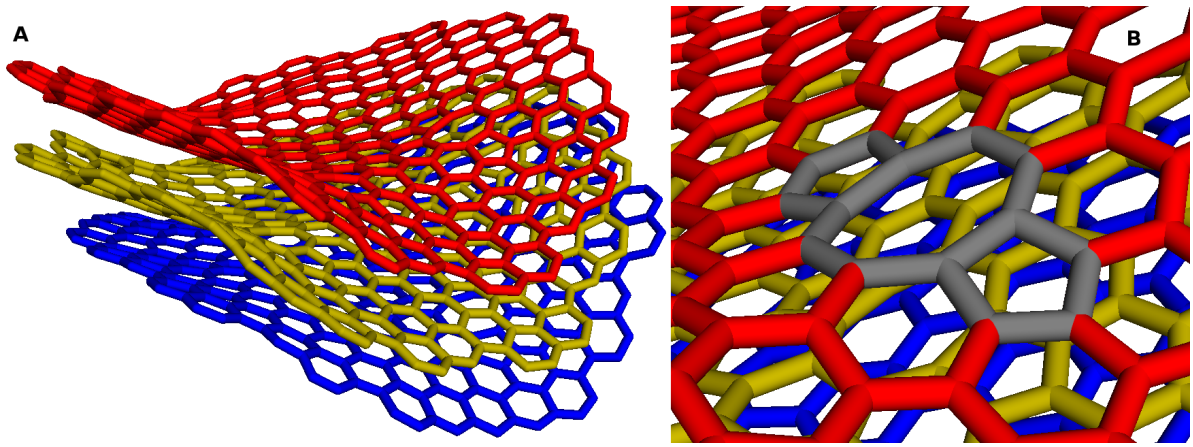

Figure 4.16: Visualisation of the best fitting model – di-vacancies (a) along with magnification of the area of the defect(b) for the graphene sample.

4.2.3 Summary

Results obtained with all techniques are consistent and suggest a thin, highly disordered system. Images from *HRTEM* might offer a suggestion why the crystallite size calculated based on Raman spectroscopy data overestimates the size when compared to the one obtained from computer simulations and Wide Angle Scattering techniques. The Raman spectroscopy suggested on average 42 Å. From the diffraction method a diameter of 36 Å was derived. The *HRTEM* shows bigger interlinked system than both Raman spectroscopy and diffraction techniques directly predict. The diffraction data does not exclude the possibility of formation of bigger interlinked structures, however it would be challenging or straightforwardly impossible to simulate that kind of system with the *MD* method. Those linking areas as well as the presence of other "chips" linked might lead to the higher value obtained from the empirical formula used in the interpretation of Raman scattering data. The curved shapes visible in the *HRTEM* images can be explained by the presence of defects in the honeycomb structure which leads to the distortion of the flat graphene layer as shown by *MD* simulations.

4.3 Saccharose samples

4.3.1 Experimental measurements

Wide Angle Scattering data

The Wide Angle Scattering data was collected both with neutrons and synchrotron source. The comparison of the measured data is presented in Figure 4.17, Figure 4.18 for the carbonized sample and Figure 4.19, Figure 4.20 for the activated one. All acquired data is of good quality and consistent within both techniques. There are some differences which can be accounted for by e.g. different spatial resolution of both diffractometers, calibration or differences of interactions between matter and neutrons or photons. The differences in interaction result also in the required data treatment being different. For the activated sample the most important difference is visible in the 1^{st} peak – graphitic 002, in the synchrotron data, there is an extra sharp peak overlapping the main one. This can be explained by the better resolution in reciprocal space of X-ray scattering data. It is also the reason behind sharpening of the 2^{nd} peak. Apart from those discrepancies, peak positions are in agreement for both data sets. Further analysis of the data is presented in Chapter 4.3.2.

High Resolution Transmission Electron Microscopy

In Figure 4.21 and Figure 4.22, there are a few images obtained for the carbonized and activated samples respectively. The carbonized sample presents a more solid structure of deformed layers, sometimes (Figure 4.21a, Figure 4.21c) in an onion-like shape. In Figure 4.21a one can spot structures resembling bigger pores, however they are not common within the sample. The structure seems to be thin, crumpled and overlapping. While the exact number of layers is impossible to predict from the pictures, it is clear than there is no visible multi-layered regions. The pictures of the activated sample confirm that the activation process was successful since pores are clearly visible. The sample is less homogeneous, there are regions which seem to have a higher number of layers, mostly in regions of walls of pores. However, in general the sample presents a

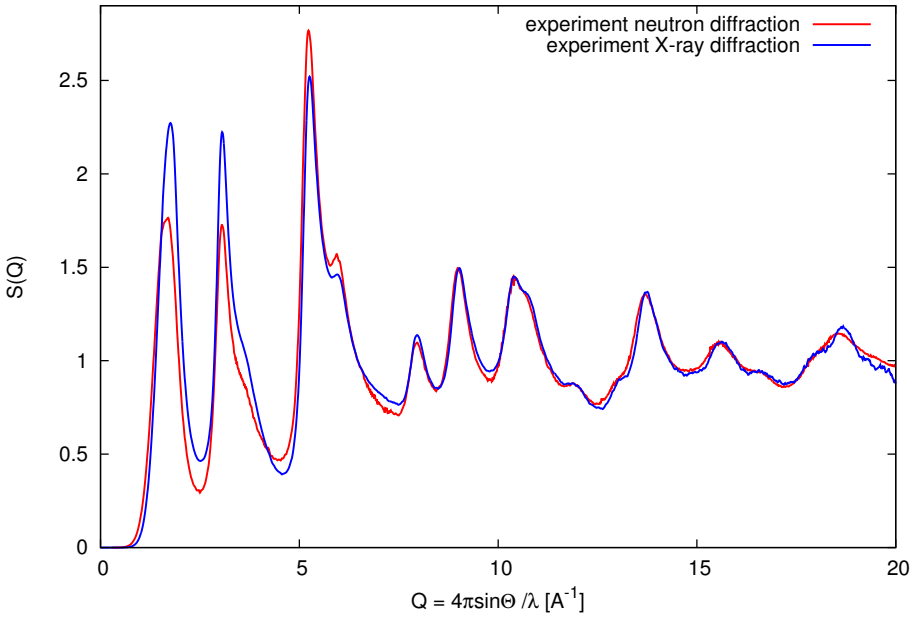

Figure 4.17: Comparison of the structural factors for the neutron and X-ray experimental data for carbonized saccharose.

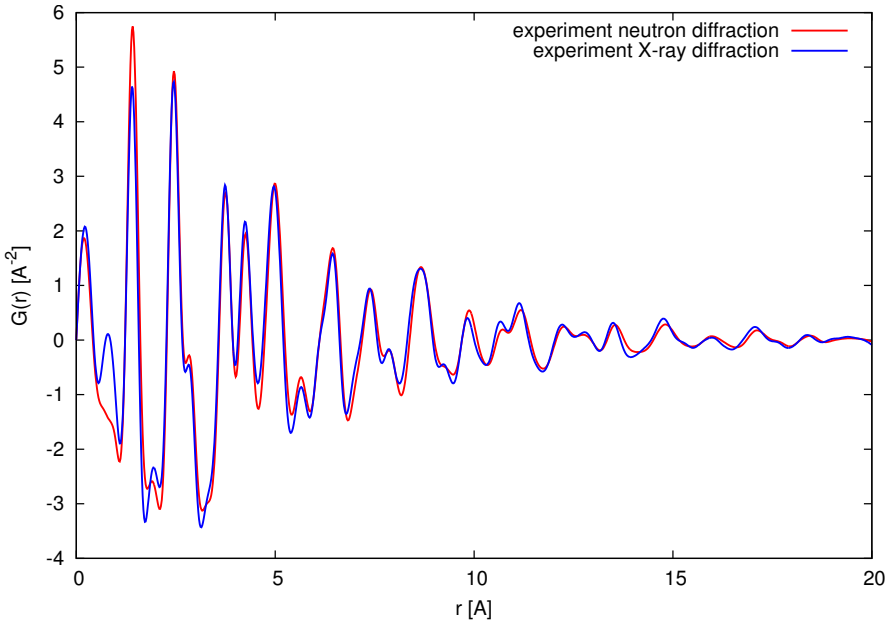

Figure 4.18: Comparison of the PDFs for the neutron and X-ray experimental data carbonized saccharose.

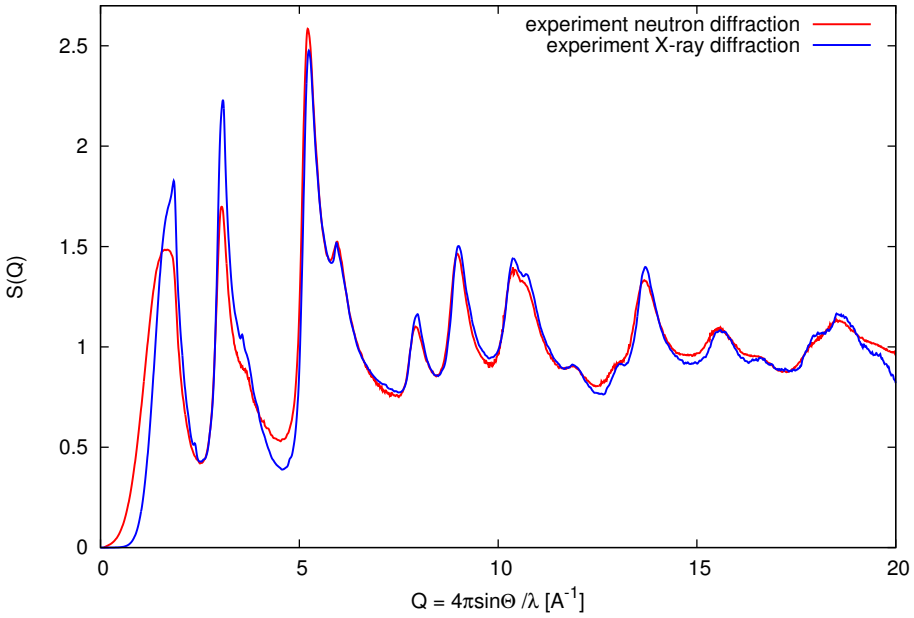

Figure 4.19: Comparison of the structural factors for the neutron and X-ray experimental data for activated saccharose.

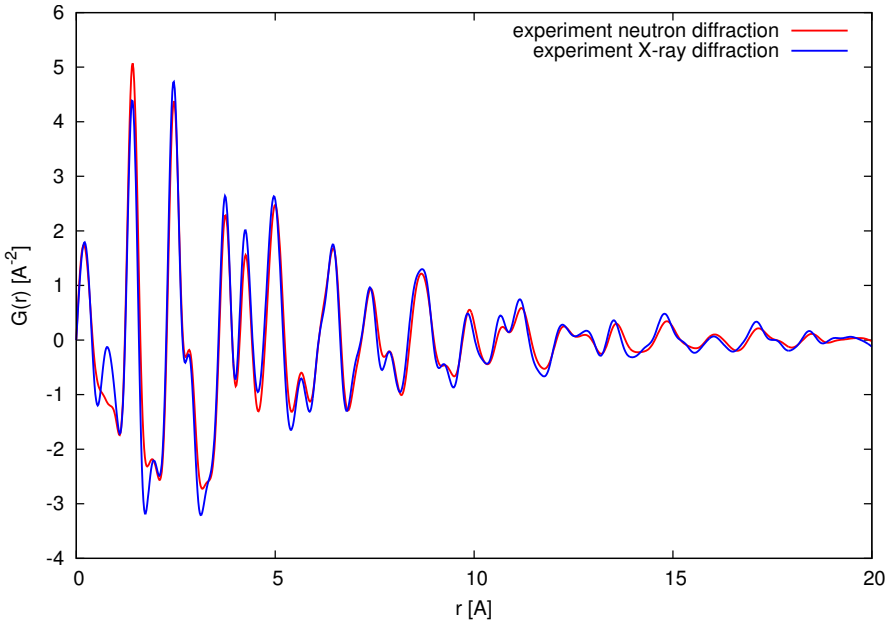

Figure 4.20: Comparison of the PDFs for the neutron and X-ray experimental data activated saccharose.

lower number of layers. In Figure 4.22b, in the thicker wall of the bigger pore, smaller, needle shaped ones appear. On the smaller scale the layers are curved, distorted – it is nicely visible at the edge of Figure 4.22c where the sample is the thinnest. The obtained results are consistent with the other findings.

Raman spectroscopy

In the tables: Table 4.7 and Table 4.8 results from fitting the data obtained through Raman scattering of carbonized and activated samples respectively are gathered. The original data is presented in the same order in Figure 4.23a and Figure 4.23b. The data for the carbonized sample is consistent from point to point of measurements, while the activated sample varies between measurements. The conclusions drawn from pictures of raw data are backed by the calculated D/G ratios which suggest that the carbonized sample is homogeneous while the activated one varies, which is directly linked with its stable, and in the second case, varying crystallite size. The peak positions vary slightly more for the activated sample.

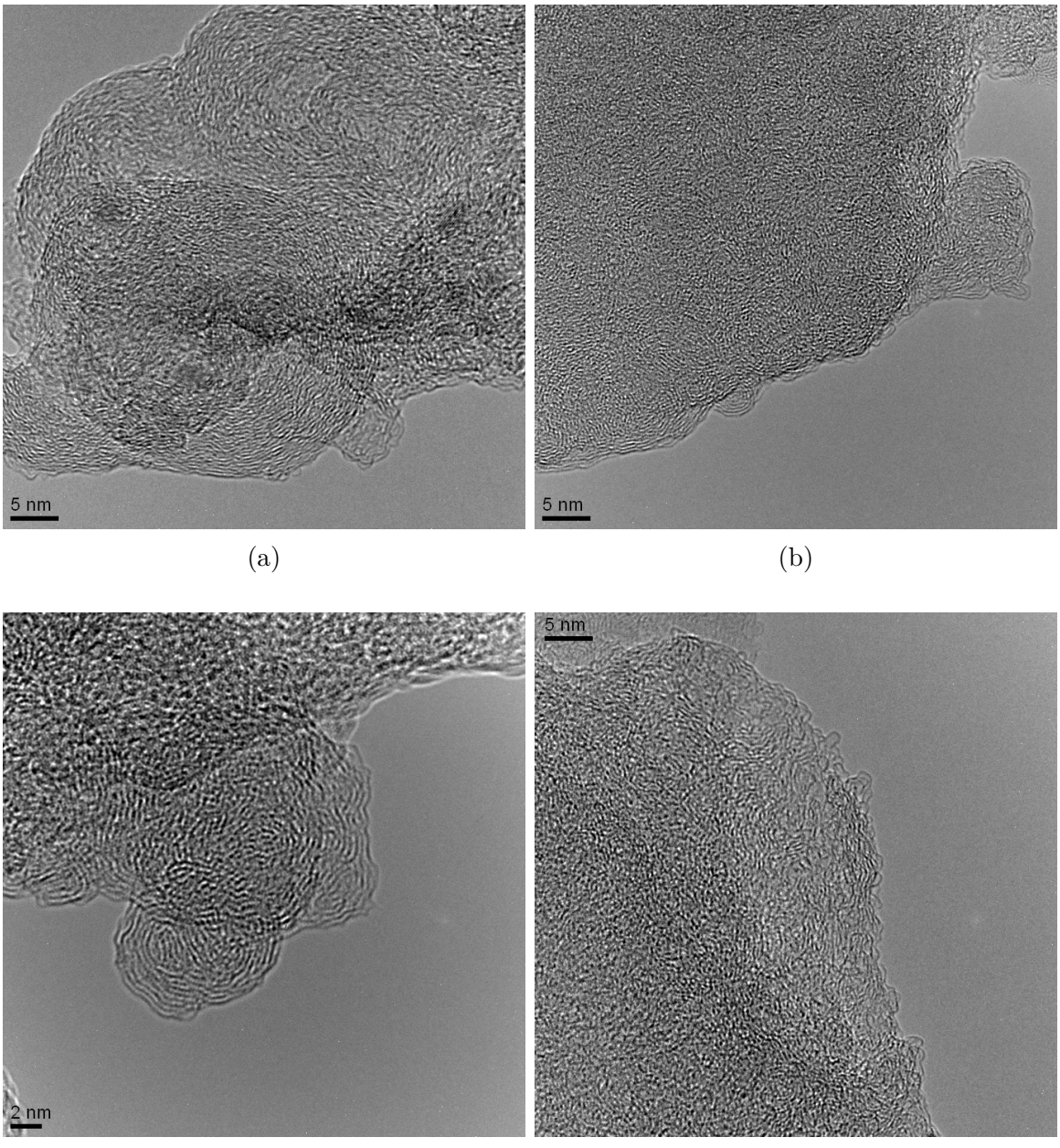

(a) (b)

(c) (d)

Figure 4.21: HRTEM images of carbonized saccharose.

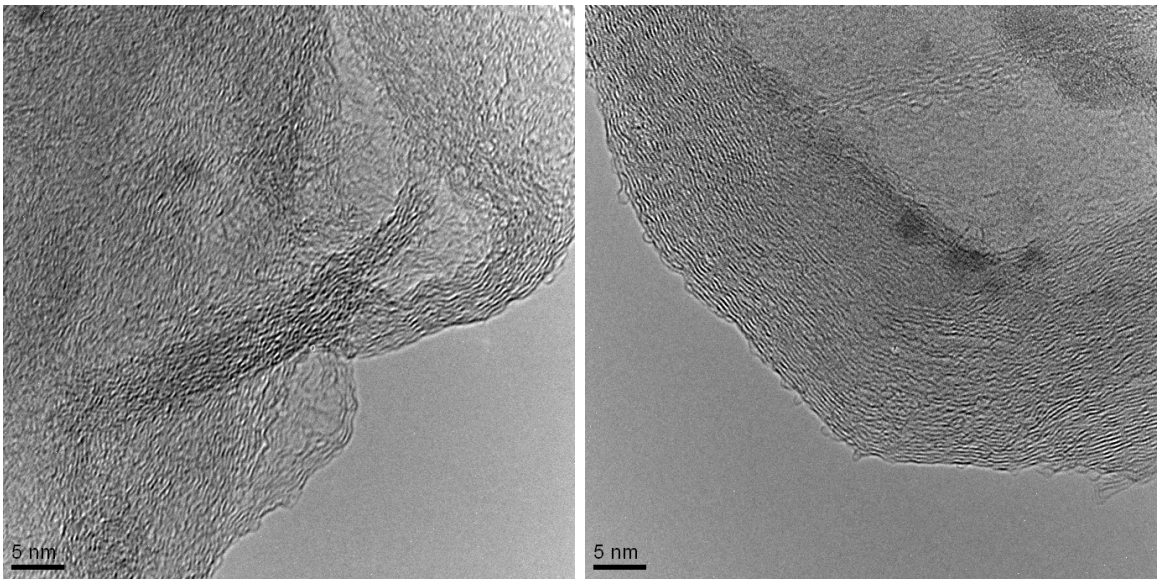

(a) (b)

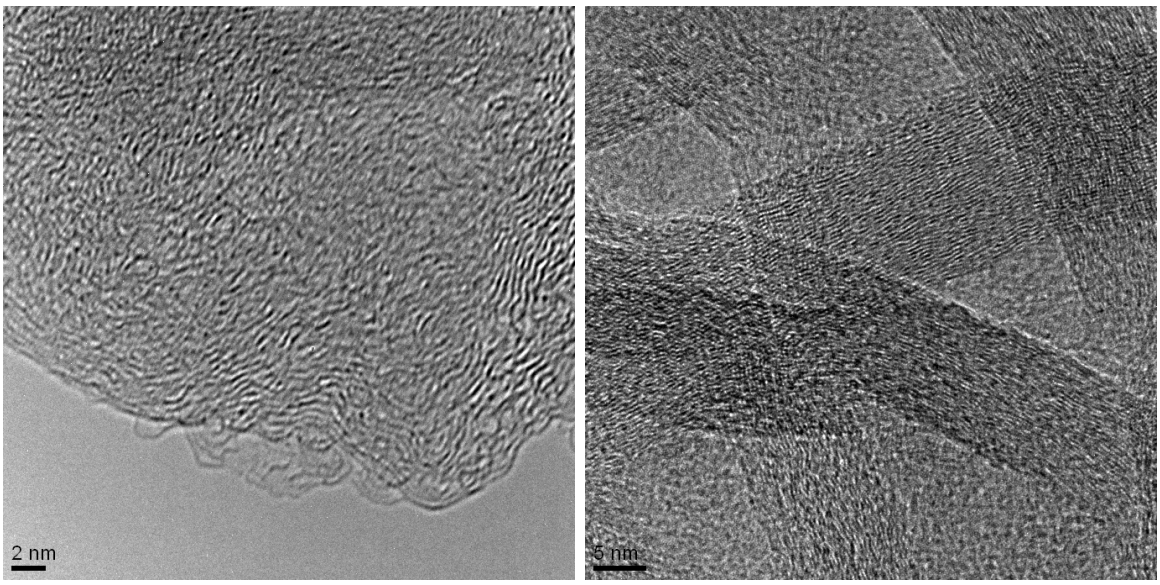

(c) (d)

Figure 4.22: HRTEM images of activated saccharose.

Table 4.7: Peak positions, D/G ratio and crystalline size (L_a) for the carbonized saccharose sample.

	G[cm^{-1}]	D[cm^{-1}]	D'[cm^{-1}]	D''[cm^{-1}]	D'''[cm^{-1}]	D/G	L_a[Å]
1	1590	1352	1619	1513	1182	1.51	29
2	1589	1352	1619	1518	1183	1.62	27
3	1588	1351	1618	1518	1187	1.74	25
4	1589	1352	1619	1517	1184	1.60	28
5	1589	1349	1619	1517	1184	1.53	29
6	1588	1348	1617	1517	1184	1.55	28
7	1588	1349	1617	1518	1183	1.62	27
8	1587	1349	1617	1518	1185	1.60	27
9	1588	1348	1617	1517	1184	1.59	28
10	1590	1352	1618	1513	1185	1.54	28
avg.	**1589**	**1350**	**1618**	**1517**	**1184**	**1.59**	**28**

Table 4.8: Peak positions, D/G ratio and crystalline size (L_a) for the activated saccharose sample.

	G[cm^{-1}]	D[cm^{-1}]	D'[cm^{-1}]	D''[cm^{-1}]	D'''[cm^{-1}]	D/G	L_a[Å]
1	1585	1348	1619	1505	1186	1.41	31
2	1585	1349	1619	1505	1189	1.33	33
3	1588	1348	1619	1510	1187	1.49	30
4	1586	1347	1619	1505	1185	1.45	30
5	1579	1348	1616	1487	1190	0.38	115
6	1582	1346	1619	1505	1185	1.07	41
7	1578	1349	1616	1481	1180	0.27	161
8	1587	1347	1619	1512	1183	1.55	28
9	1578	1348	1616	1483	1188	0.39	113
10	1574	1344	1613	1488	1183	0.31	141
avg.	**1582**	**1347**	**1617**	**1498**	**1186**	**0.97**	**72**

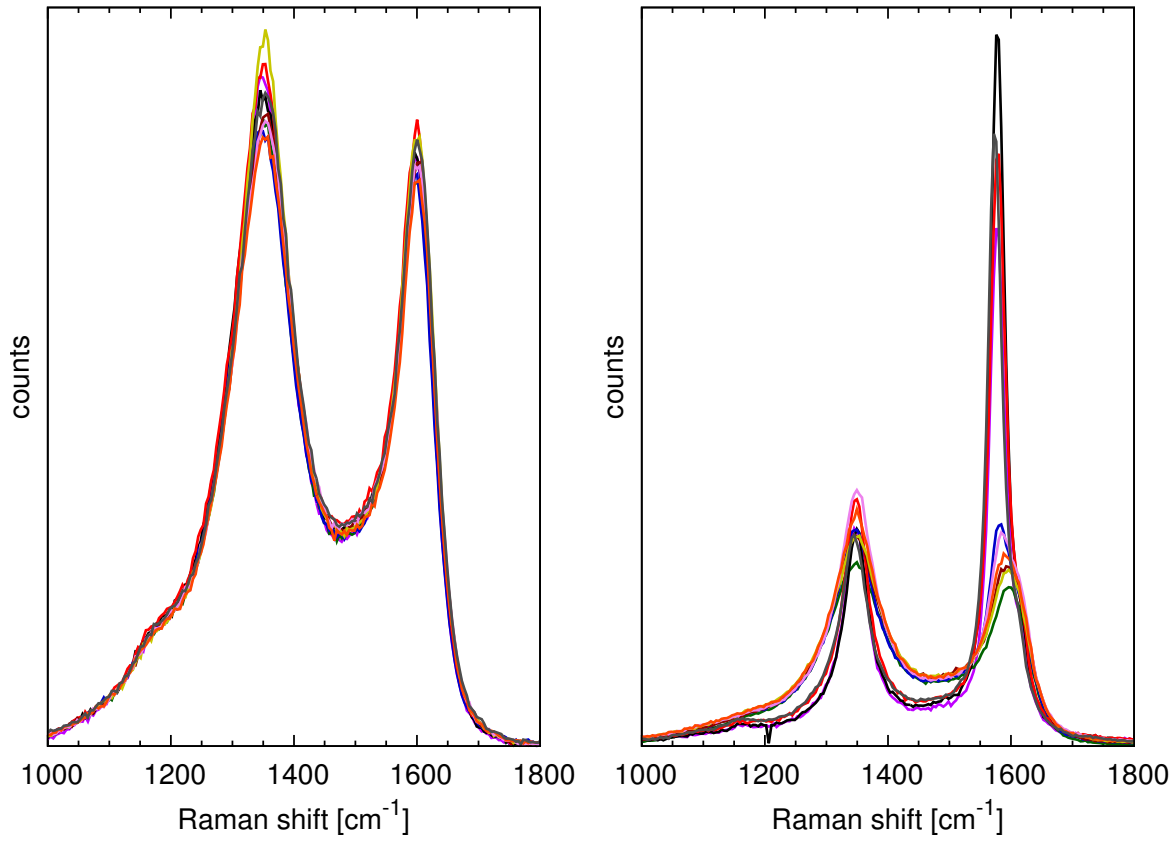

(a) carbonized sample

(b) activated sample

Figure 4.23: Visualisation of Raman scattering by the saccharose samples. Data was modified in order to be in the same range in the figure.

4.3.2 Computer simulations

Microcrystalline model

The model parameters are gathered in Table 4.9. The model for the carbonized sample is shown at the top of figures: Figure 4.26 – $S(Q)$ compared to X-ray scattering data, Figure 4.24 – $S(Q)$ compared to neutron scattering data, Figure 4.27 – PDF compared to X-ray scattering data, Figure 4.25 – PDF compared to neutron scattering data. For the activated sample model is shown at the top of: Figure 4.28, Figure 4.30, Figure 4.29, Figure 4.31 in the same order. In both cases it is clearly visible that proposed models do not reproduce features of measured data, additional peaks are visible moreover the observed peaks are also too pronounced. Since there is no disorder introduced within

Table 4.9: Parameters for the microcrystalline model for saccharose samples.

parameter	carbonized	activated
No. of layers	4	3
ϕ of system	24 Å	24 Å
lattice parameters a & b	2.438 Å	2.445 Å
lattice parameter c	7.1 Å	7. Å
σ_{intra}	0.03 Å	0.03 Å
σ_{inter}	0.03 Å	0.03 Å

the system height of the 1^{st} peak seems to be off. Because it was obvious that additional disorder introduced within the model is necessary to explain samples structures it was not considered as a shortcoming of the models. It was also determined unnecessary to complicate the activated sample's model any further to explain the sharp feature appearing in the (002) peak. It will be taken into account at later stages of the analysis. The values of discrepancy factor R are gathered in Table 4.13.

Turbostratic model

The model parameters are gathered in Table 4.10. The calculated model along with measured data for the carbonized sample is presented in figures: Figure 4.26 – $S(Q)$ for X-ray scattering data, Figure 4.24 – $S(Q)$ for neutron X-ray scattering data, Figure 4.27 – *PDF* for the X-ray scattering data, Figure 4.25 – *PDF* for the neutron scattering data. In the same sequence figures for activated sample are presented: Figure 4.28, Figure 4.30, Figure 4.29, Figure 4.31. Despite breaking order along c axis through introducing rotation of layers, peaks in both models are still too sharp to properly reproduce measured data. Similarly to the previous model (microcrystalline), it was

Table 4.10: Parameters for turbostratic model for saccharose samples.

parameter	carbonized	activated
No. of layers	4	3
ϕ of system	24 Å	24 Å
lattice parameters a & b	2.438 Å	2.445 Å
lattice parameter c	7.1 Å	7. Å
range of rotation angles	0^o–21^o	0^o–21^o
σ_{intra}	0.03 Å	0.03 Å
σ_{inter}	0.03 Å	0.03 Å

determined that building a more complicated model for the activated sample in order to explain the additional peak overlapping the 1^{st} one was unnecessary at this point. These models also prove that it would be beneficial to correlate the disorder with atom-atom distance as it is done in the paracrystalline model instead of using a constant value of the Debye-Waller factor. The agreement between calculated models and measured data is presented in Table 4.13 in the form of the discrepancy factor R.

Paracrystalline model

The model parameters are gathered in Table 4.11. For the carbonized sample the $S(Q)$ and the *PDFs* are gathered in (neutron, X-ray data): Figure 4.24, Figure 4.26, Figure 4.25, Figure 4.27. The same is valid for activated sample for figures: Figure 4.28, Figure 4.30, Figure 4.29, Figure 4.31. In both cases in order to determine the number of layers the height of the 1^{st} peak provided by the X-ray scattering measurement was regarded as more trustworthy. For the activated sample the final model is constructed as a weighted sum of two separate paracrystalline models: with lower and higher number

Table 4.11: Parameters for paracrystalline model for saccharose samples.

parameter	carbonized	activated (low)	activated (high)
No. of layers	4	3	15
% of layers	100%	90 %	10%
ϕ of system	24 Å	24 Å	24 Å
lattice parameters a & b	2.438 Å	2.445 Å	2.445 Å
lattice parameter c	7.1 Å	7. Å	6.78 Å
range of rotation angles	0^o–21^o	0^o–21^o	0^o–21^o
σ_0	0.043 Å	0.045 Å	0.045 Å
σ_1	0.32 Å	0.34 Å	0.23 Å
No. of averaged structures	100	100	100

of layers. This was required to explain the overlapping feature of the 1^{st} peak. In order not to overcomplicate the final models, most of the parameters were kept the same for the two components. At first the lower-layered model was finalized, which provided most of the parameters for the other component. The adjusted parameters were the lattice parameter c as it affects the position of the 1^{st} peak, σ_1 and the number of layers which affect its width and height. The values of the discrepancy factor (Table 4.13) even further reinforce the findings that the constructed models properly reproduce features of measured data.

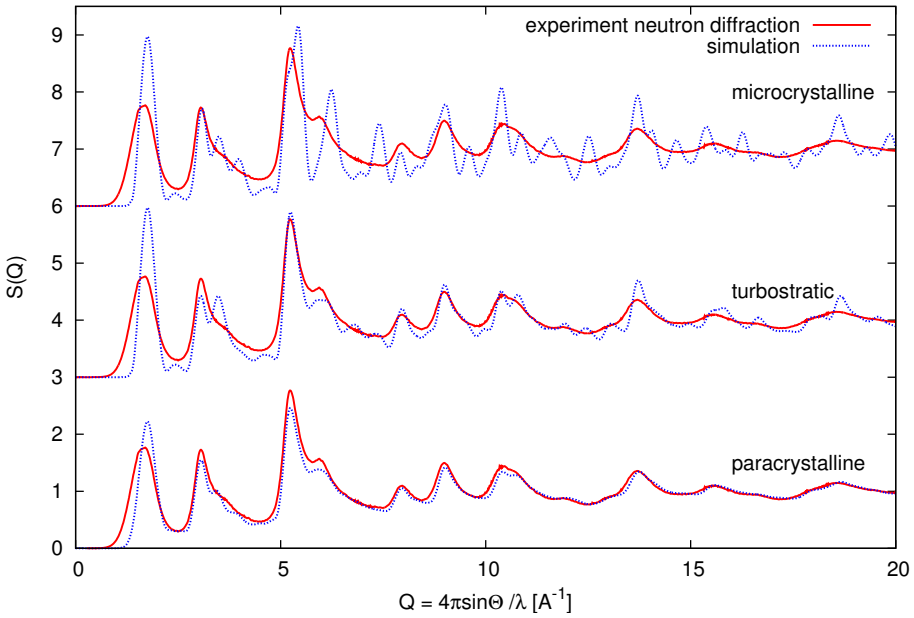

Figure 4.24: Comparison of the structural factors for: paracrystalline, turbostratic and microcrystalline models with the neutron experimental data for carbonized saccharose.

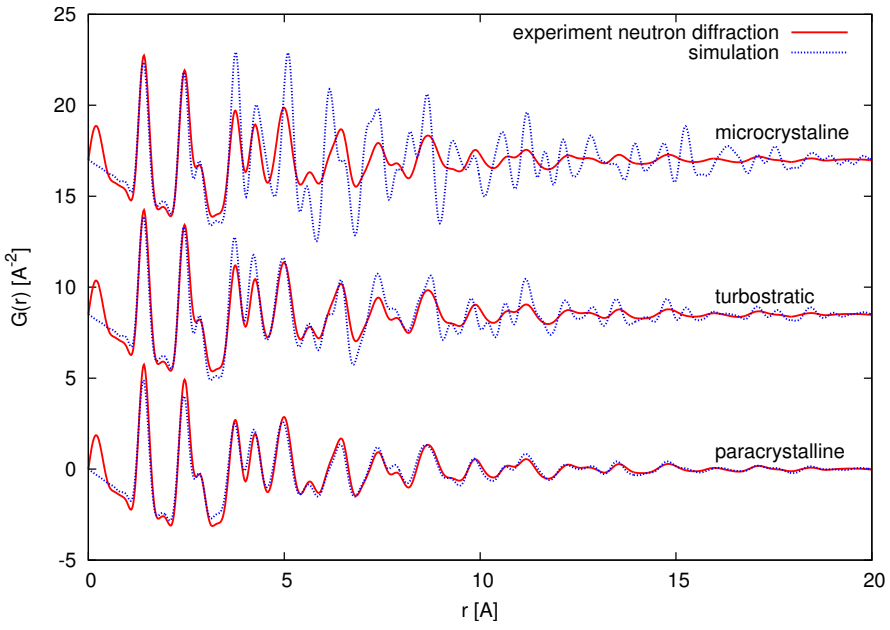

Figure 4.25: Comparison of the PDFs for: paracrystalline, turbostratic and microcrystalline models with the neutron experimental data for carbonized saccharose.

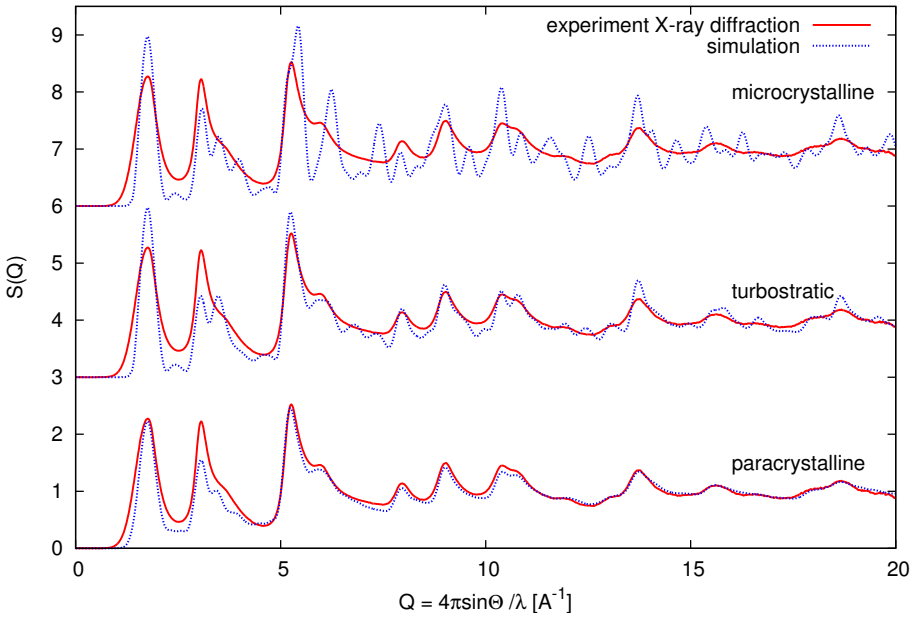

Figure 4.26: Comparison of the structural factors for: paracrystalline, turbostratic and microcrystalline models with the X-ray experimental data for carbonized saccharose.

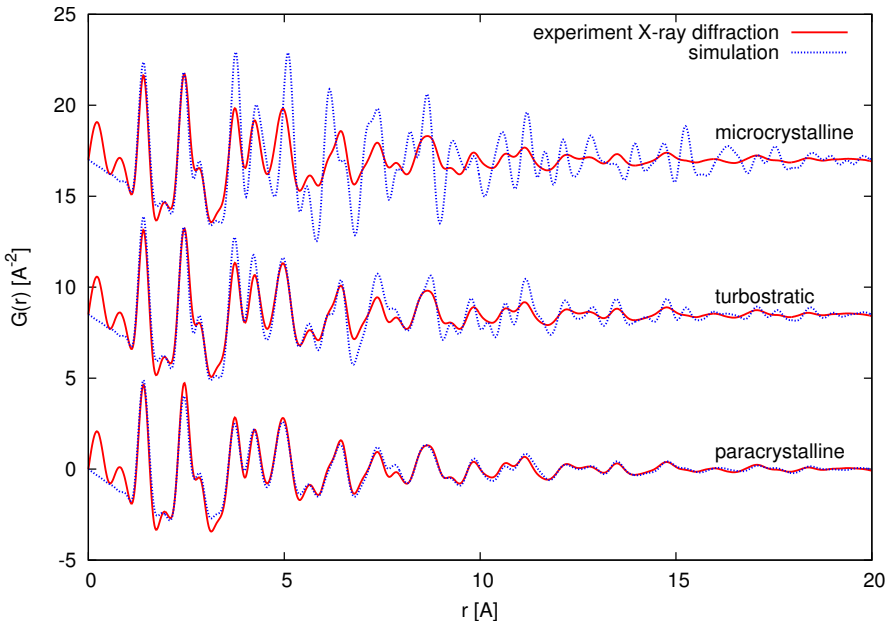

Figure 4.27: Comparison of the PDFs for: paracrystalline, turbostratic and microcrystalline models with the X-ray experimental data for carbonized saccharose.

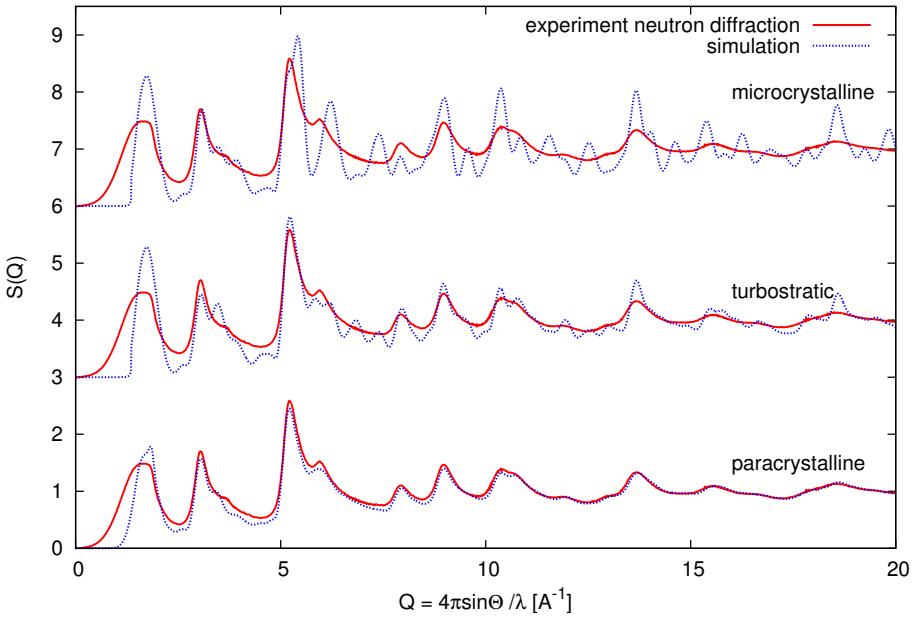

Figure 4.28: Comparison of the structural factors for: paracrystalline, turbostratic and microcrystalline models with the neutron experimental data for activated saccharose.

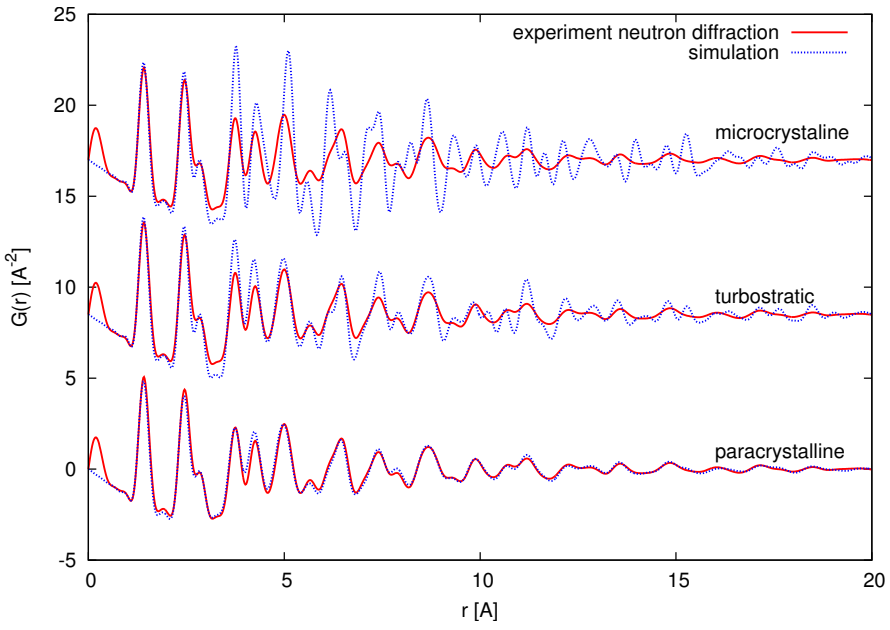

Figure 4.29: Comparison of the PDFs for: paracrystalline, turbostratic and microcrystalline models with the neutron experimental data for activated saccharose.

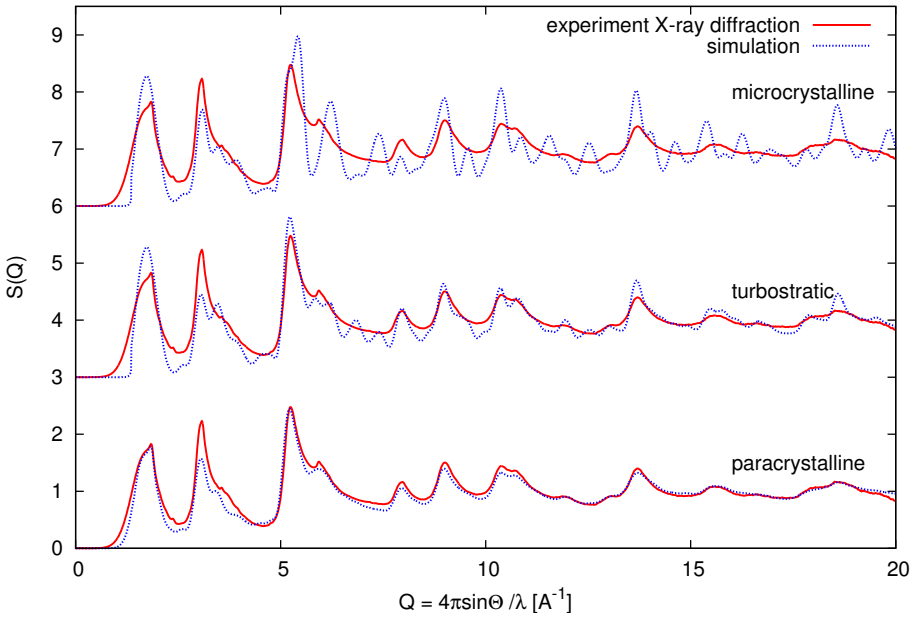

Figure 4.30: Comparison of the structural factors for: paracrystalline, turbostratic and microcrystalline models with the X-ray experimental data for activated saccharose.

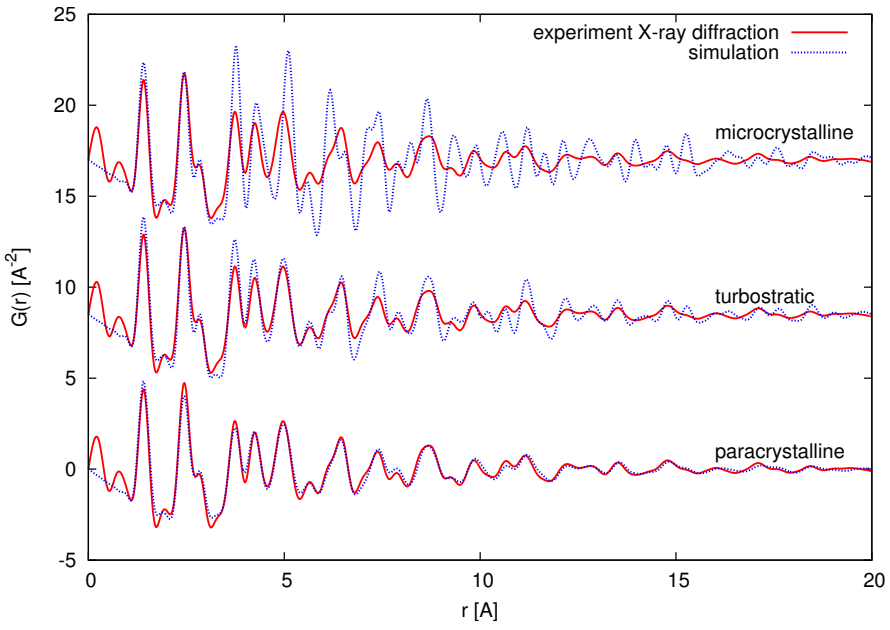

Figure 4.31: Comparison of the PDFs for: paracrystalline, turbostratic and microcrystalline models with the X-ray experimental data for activated saccharose.

Molecular dynamics

The models parameters are gathered in Table 4.12. For the carbonized sample, the calculated $S(Q)$ and *PDFs* for selected models are compared to the measured data in the figures: Figure 4.32, Figure 4.34, Figure 4.33, Figure 4.35. For the activated sample the same is done in the figures: Figure 4.36, Figure 4.38, Figure 4.37, Figure 4.39. In order to account for the features of the 1^{st} peak of the activated sample, models for it were calculated as a weighted sum of two components. Because calculating models with 15 layers would involve more than 2700 atoms, it was decided to use the paracrystalline model as a high-layered addition to the computed MD models for the activated sample. The paracrystalline addition after taking into account its percentage contributes mostly to the 1^{st} peak without disruption to the further data. Another advantage of such an approach was precise control over the required peak position since in MD simulations only potentials influence interlayer distance. Moreover, layers tend to shift creating voids which leads to lower peak amplitude. The ratio between higher-layered and lower-layered systems are kept the same as for paracrystalline model. Based on presented $S(Q)$ and *PDFs* along with values presented in the Table 4.13 one can discard the STW type of defect as the one having significantly higher R values. It is more pronounced with neutron diffraction data, most likely due to its better resolution in the real space. It is more difficult to distinguish between mono- and di-vacancies since the differences are more subtle in those cases. For the carbonized sample, mono-vacancies have slightly lower R values for both X-ray and neutron data. In the case of the activated sample, for the X-ray data the difference in favour of mono-vacancies is more obvious than the preference for di-vacancies in the case of the neutron data – 0.1% which leads to the conclusion that mono-vacancies are more likely to dominate the sample structure without excluding di-vacancies from the overall structure mix. In both cases it is more realistic that the wholesome structure includes both mono- and di-vacancies. The visualisations of proposed models containing mono- and di- vacancies for both samples are presented in Figure 4.40.

Table 4.12: The parameters for MD models for saccharose samples.

parameter	carbonized	activated
No. of layers – low	4	3
% of layers – low	100 %	90 %
No. of layers – high	–	15
% of layers – high	–	10 %
No. of mono-vacancies per layer	$3^1/_4$	$3^1/_3$
No. of di-vacancies per layer	1	$1^1/_3$
No. of STW type of defect per layer	1	$1^1/_3$

Table 4.13: Discrepancy factors between models and experimental data.

model	carbonized		activated	
	R_{x-ray}	$R_{neutrons}$	R_{x-ray}	$R_{neutrons}$
microcrystalline	103.0%	97.6%	102.0%	106.0%
turbostratic	47.3%	45.8%	46.4%	50.3%
paracrystalline	31.9%	29.6%	29.3%	26.0%
mono-vacancy	33.4%	25.5%	30.4%	25.2%
di-vacancy	35.0%	25.8%	32.8%	25.1%
STW type defect	38.8%	32.1%	36%	32.3%

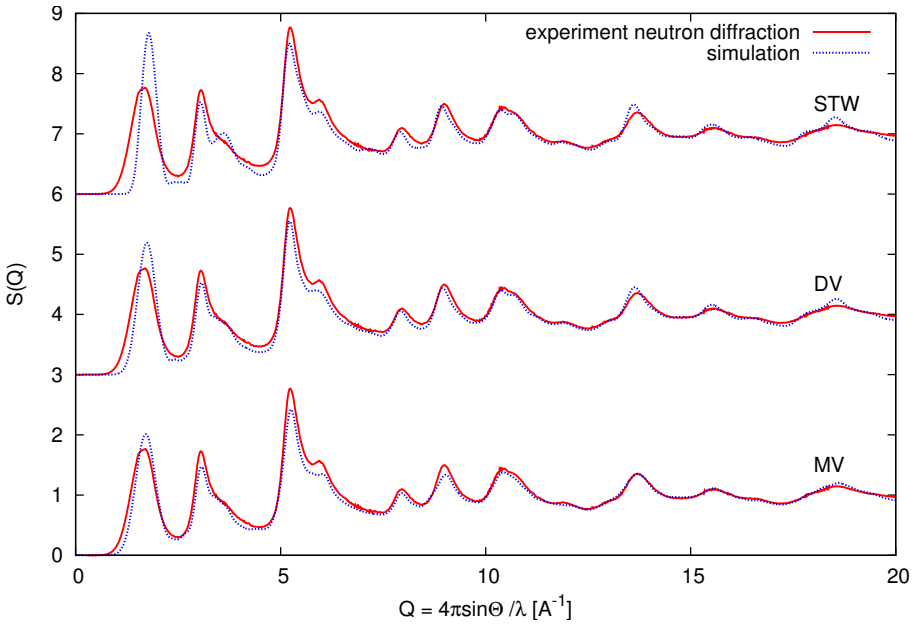

Figure 4.32: Comparison of the structural factors for theoretical models containing: mono-, di- vacancies and STW type defects with the neutron experimental data for carbonized saccharose.

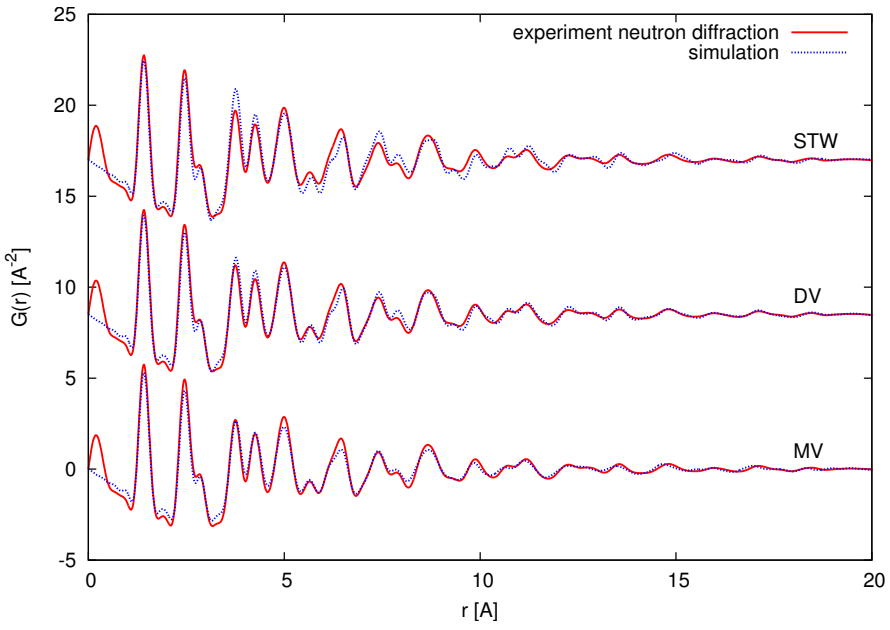

Figure 4.33: Comparison of the PDFs for theoretical models containing: mono-, di-vacancies and STW type defects with the neutron experimental data for carbonized saccharose.

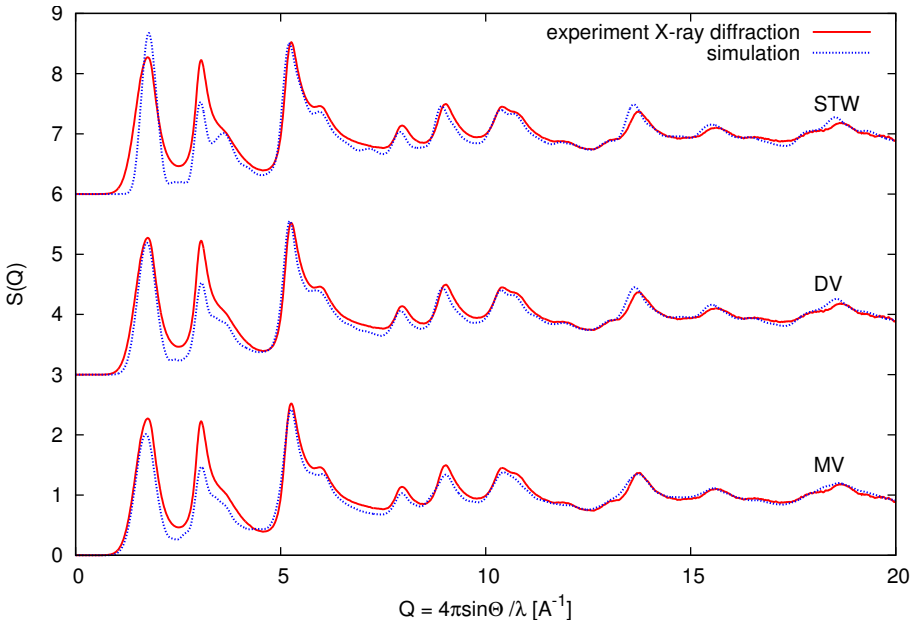

Figure 4.34: Comparison of the structural factors for theoretical models containing: mono-, di- vacancies and STW type defects with the X-ray experimental data for carbonized saccharose.

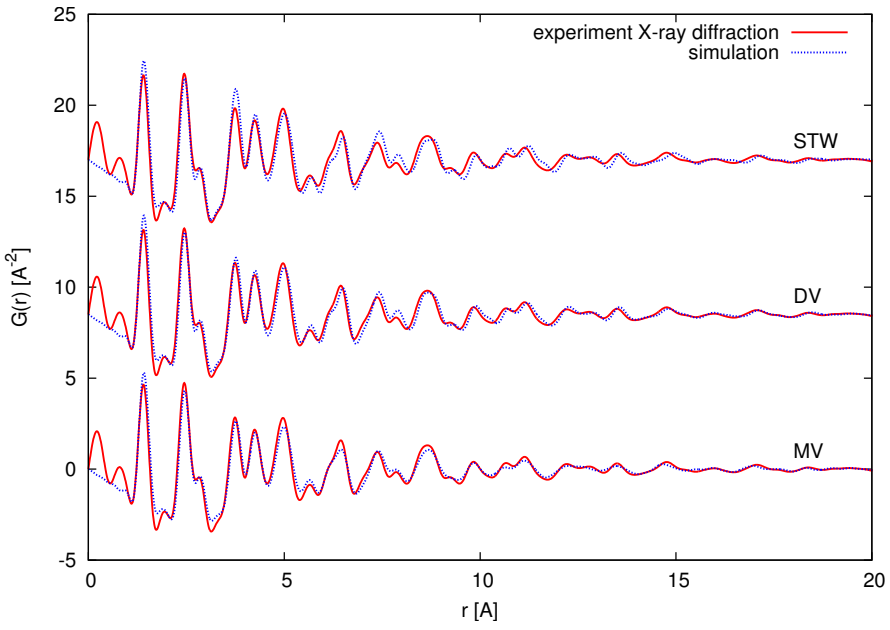

Figure 4.35: Comparison of the PDFs for theoretical models containing: mono- and di- vacancies and STW type defects with the X-ray experimental data for carbonized saccharose.

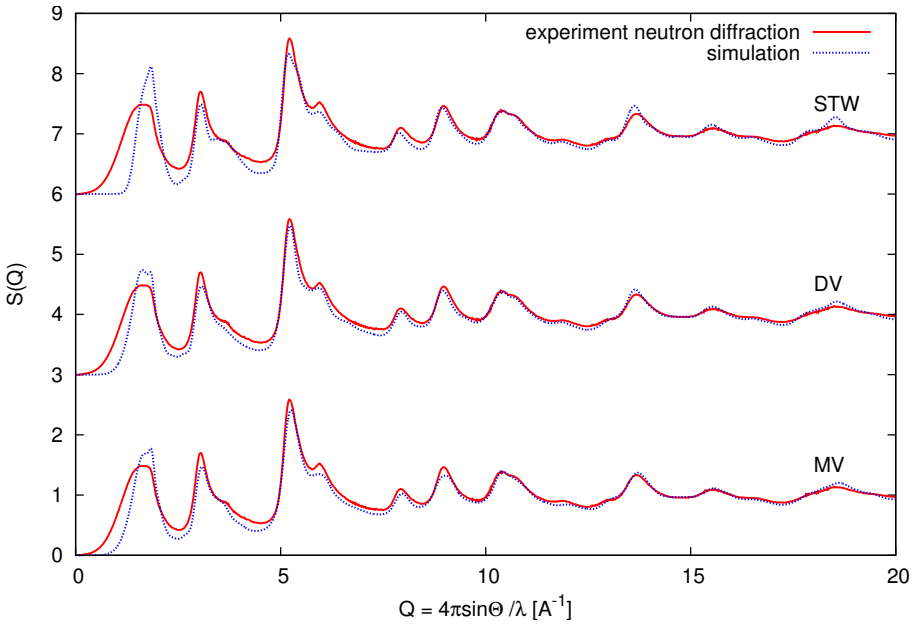

Figure 4.36: Comparison of the structural factors for theoretical models containing: mono-, di- vacancies and STW type defects with the neutron experimental data for activated saccharose.

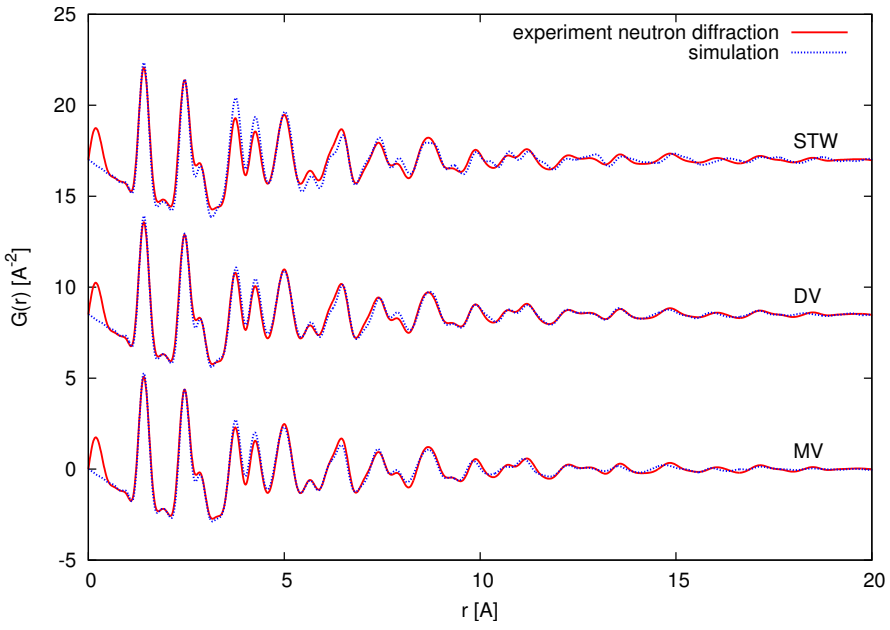

Figure 4.37: Comparison of the PDFs for theoretical models containing: mono-, di-vacancies and STW type defects with the neutron experimental data for activated saccharose.

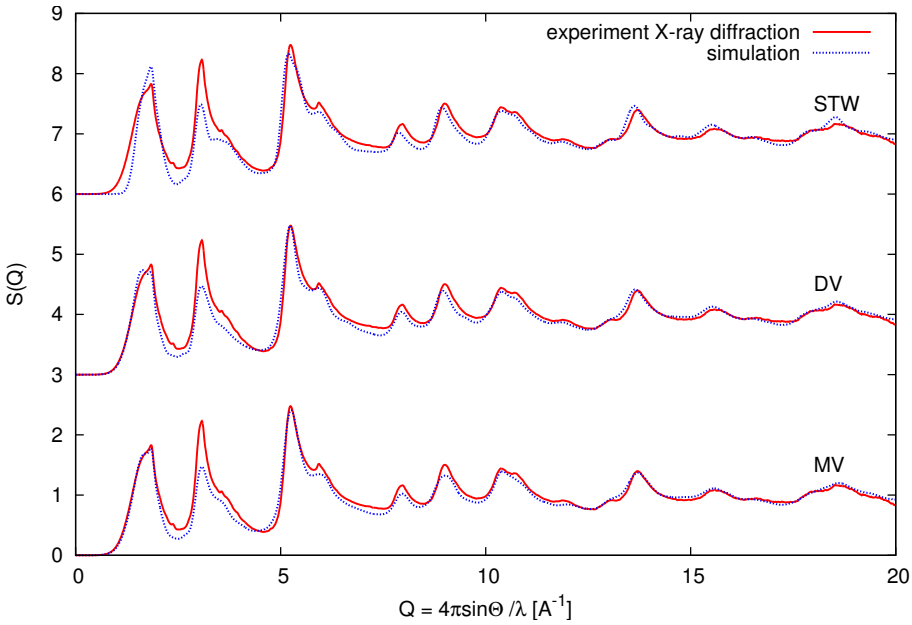

Figure 4.38: Comparison of the structural factors for theoretical models containing: mono-, di- vacancies and STW type defects with the X-ray experimental data for activated saccharose.

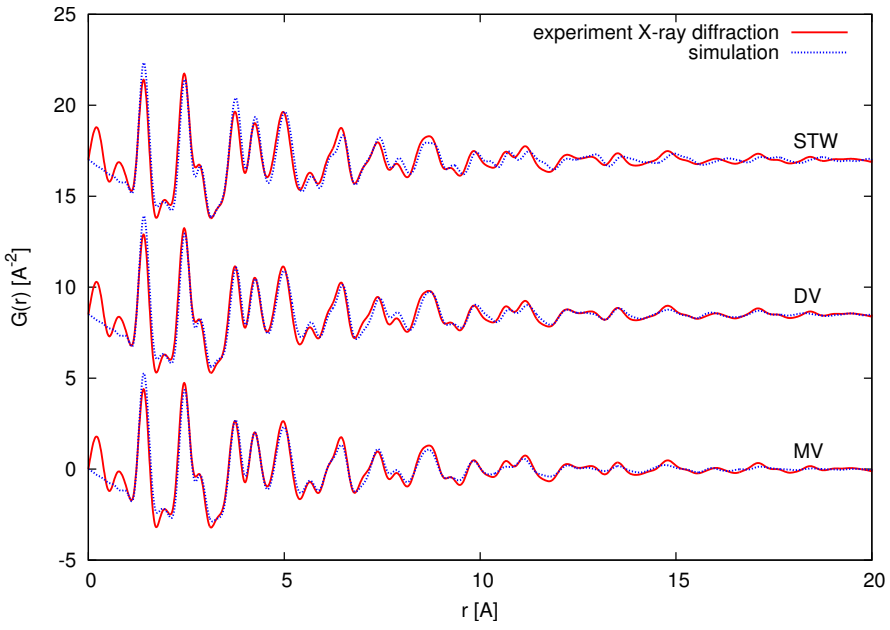

Figure 4.39: Comparison of the PDFs for theoretical models containing: mono- and di- vacancies and STW type defects with the X-ray experimental data for activated saccharose.

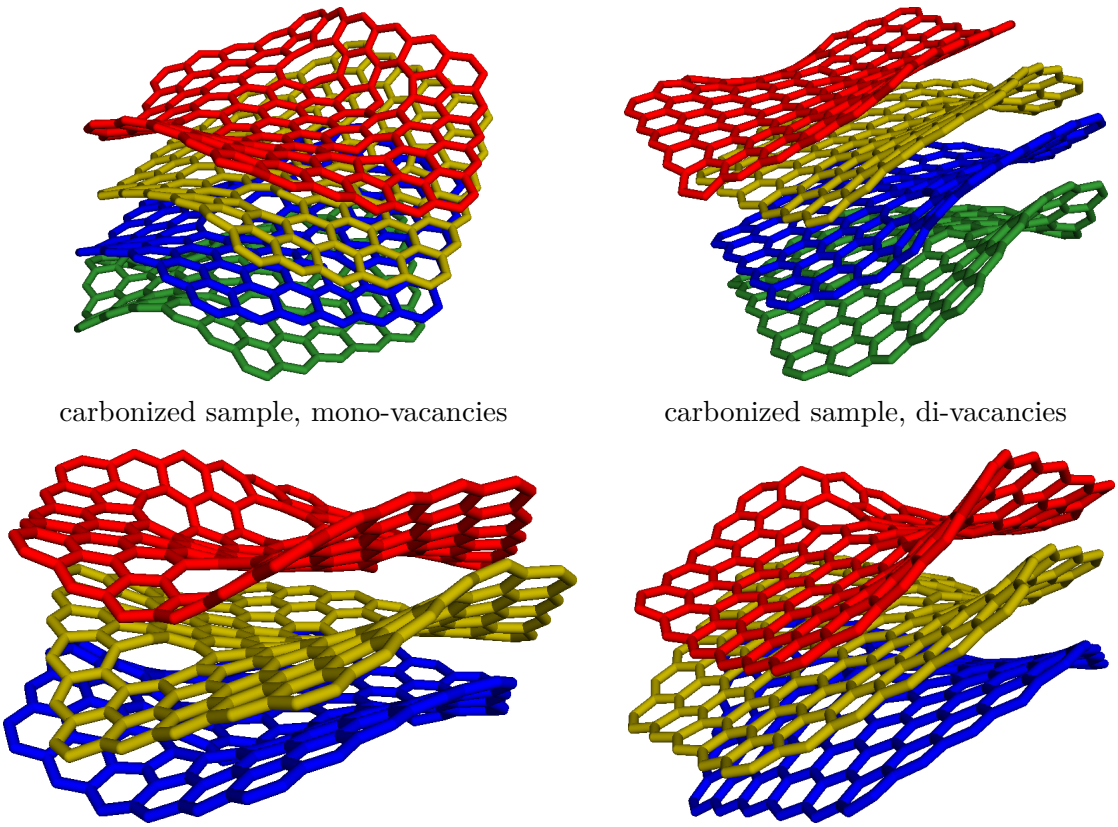

carbonized sample, mono-vacancies

carbonized sample, di-vacancies

activated sample, mono-vacancies

activated sample, di-vacancies

Figure 4.40: Visualisation of MD simulations for saccharose sample containing mono- and di- vacancies.

4.3.3 Summary

For both saccharose samples the obtained results are self-consistent.

For the carbonized sample they paint a picture of a relatively homogeneous structure constructed from small, distorted, graphene-like pieces. From Raman measurements, an average value of $L_a = 28$ Å was obtained, while the X-ray/neutron scattering techniques combined with computer simulations gave a value of 24 Å. The obtained value for Raman scattering is from an empirical formula. The difference between 24 Å and 28 Å might arise from smaller regions with carbon honeycomb structure – the answer from diffraction measurements – are interlinked with each other giving the foundation for a bigger value obtained from Raman measurements. The performed calculations suggest that the system mostly consists of 4-layered pieces.

In case of the activated sample, the image changes already based on *HRTEM* pictures. It is a good sign as it proves that the activation process was performed properly. All techniques confirm that the sample is less homogeneous and during the activation process multi-layered regions were created. From calculations backed by measurements it was determined to be mostly a mix of 3- and 15-layered pieces in a ratio of 1 : 9. Similarly to the carbonized sample, the results obtained for crystallite size vary a bit between methods. From Raman scattering the average 72 Å was obtained, while diffraction provided 24 Å. The obtained values (Raman) were in the range from 28 Å up to 161 Å. With such a huge spread of values, combined with very small number of measurements compared to the volume of the sample investigated by scattering techniques they should be viewed more as a confirmation of inhomogeneity of the sample's structure rather than interpreting the average as a precise value. In this case, the value obtained from Raman scattering is a little less trustworthy as the measurement varied a lot from point to point.

The results obtained for both samples suggest that during the activation process the number of layers was mostly lowered, however on the pore walls multi-layered structures were created.

4.4 Cellulose samples

4.4.1 Experimental measurements

Wide Angle Scattering data

For the cellulose samples data was collected at a neutron reactor as well as at a synchrotron. The comparison of the measured data is presented in Figure 4.41, Figure 4.42 for the carbonized sample and Figure 4.43, Figure 4.44 for the activated one. The data is consistent within both sets and of very good quality. One can notice only slight differences, probably coming from the different way of interaction of matter with probes: neutrons and photons, which also lead also to different data treatment. The sharpening of first peaks of the activated sample in the data obtained from the synchrotron source, especially pronounced at the additional peak overlapping the 1st peak (i.e. the 002 one), can be accounted for by better spatial resolution of the synchrotron data. The corresponding peak positions are in great agreement despite the aforementioned issues. In Chapter 4.4.2 further analysis of the data is presented.

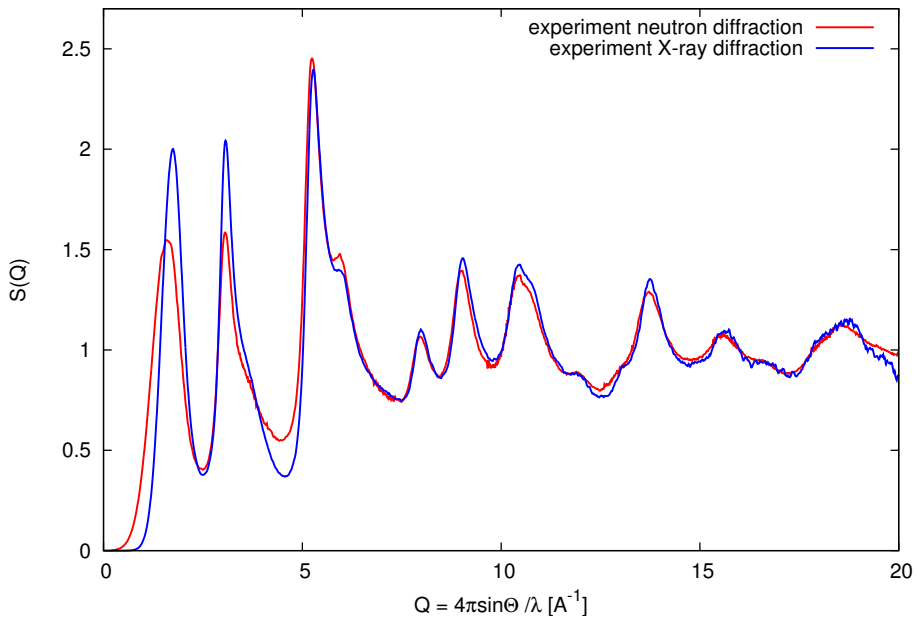

Figure 4.41: Comparison of the structural factors for the neutron and X-ray experimental data for carbonized cellulose.

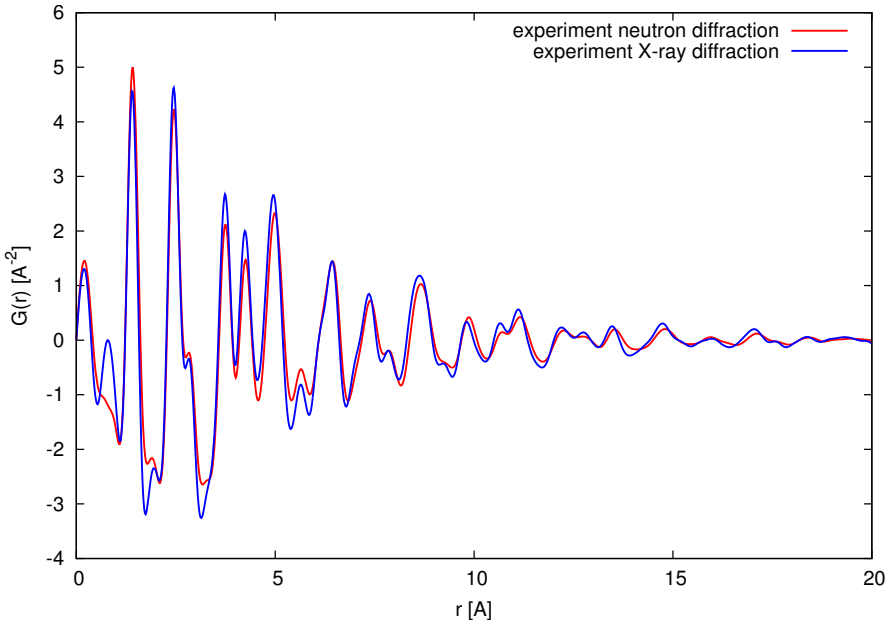

Figure 4.42: Comparison of the PDFs for the neutron and X-ray experimental data carbonized cellulose.

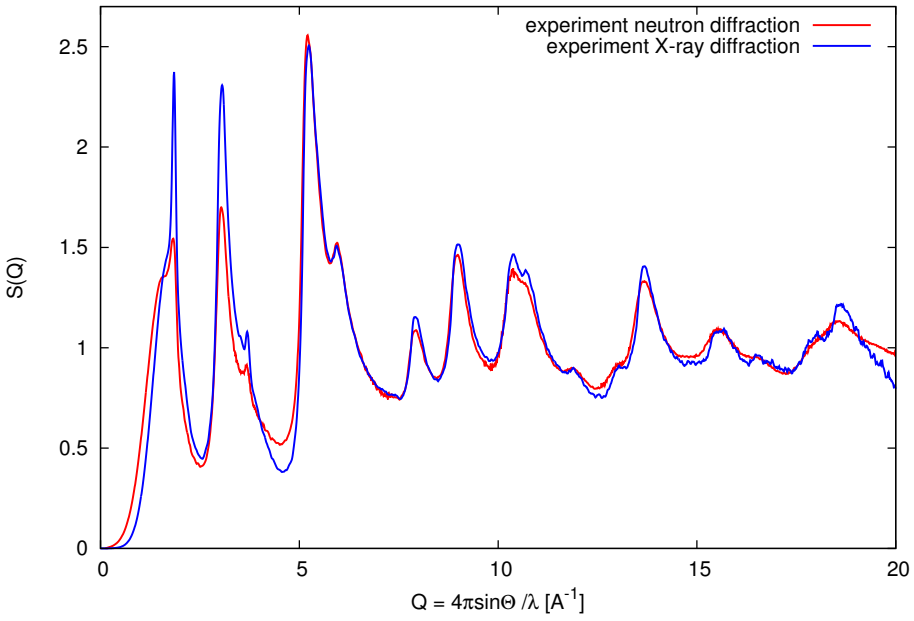

Figure 4.43: Comparison of the structural factors for the neutron and X-ray experimental data for activated cellulose.

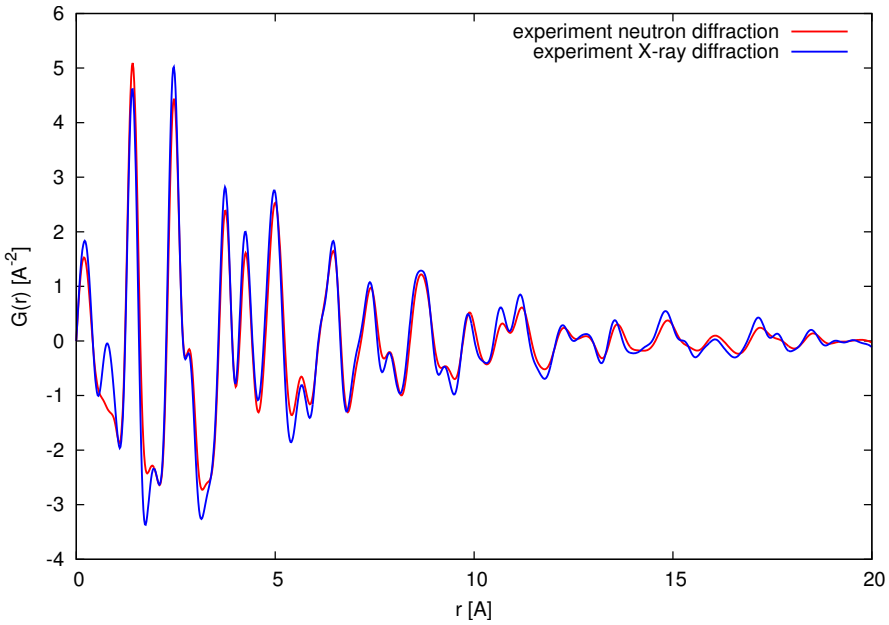

Figure 4.44: Comparison of the PDFs for the neutron and X-ray experimental data activated cellulose.

High Resolution Transmission Electron Microscopy

Selected images from *HRTEM* are presented in Figure 4.45 for the carbonized sample and for the activated one in Figure 4.46. In the pictures representing the carbonized sample one can notice the relatively compact structure built from a dense mesh of short distorted carbon layers. Rarely one can spot a pore-like structure like in the Figure 4.45d. The increase of disorder within the sample leading to appearance of nanopores as well as bigger pores confirms successful development of the specific surface of the sample. The smaller pores are clearly visible on the edge of the bigger one in the Figure 4.46b. Apart from more the disordered structure, the activated sample presents some regions with a higher number of layers, especially at the borders of pores. The conclusions drawn from obtained images are consistent with other findings.

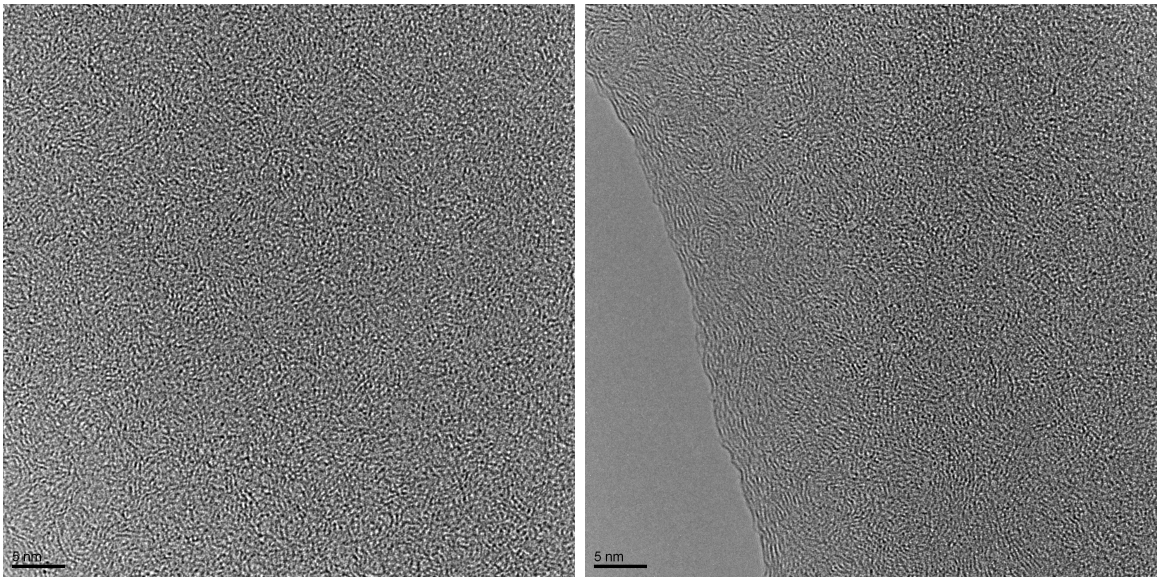

(a) (b)

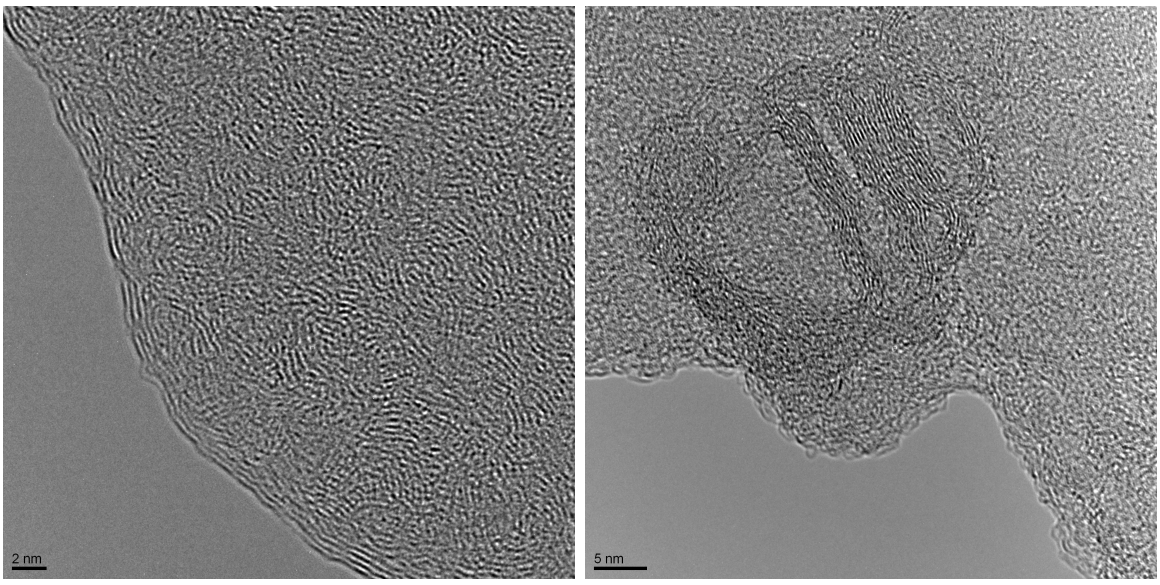

(c) (d)

Figure 4.45: HRTEM images of carbonized cellulose.

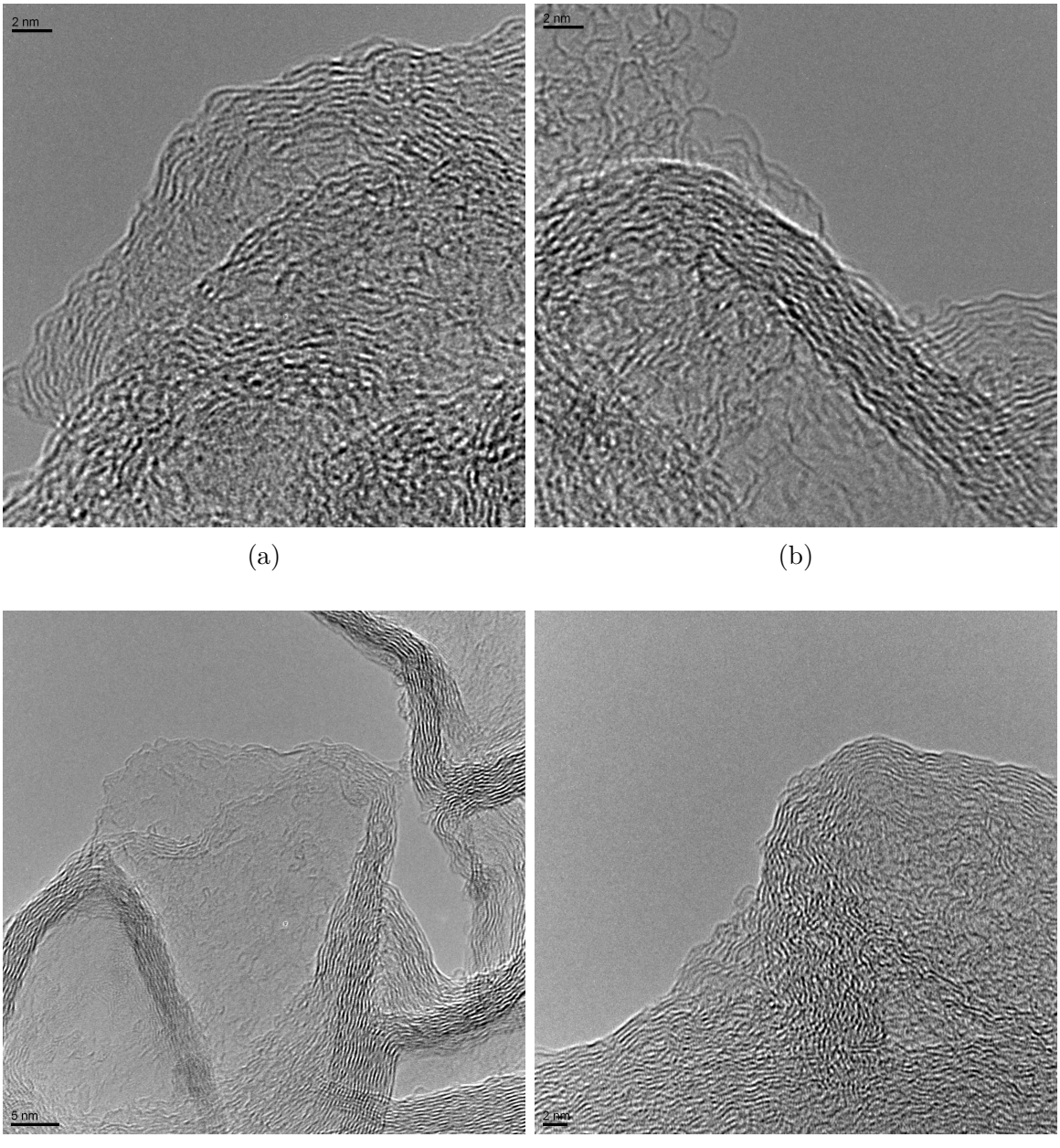

(a) (b)

(c) (d)

Figure 4.46: HRTEM images of activated cellulose.

Raman spectroscopy

The Table 4.14 (carbonized sample) and Table 4.15 (activated one) present a compilation of results obtained from the fitting of the Raman scattering data. The scattering data is presented in Figure 4.47a and Figure 4.47b. Similarly as in the case of saccarose, the carbonized sample remains consistent in D/G ratio through different measurements, while the activated one varies from quite disordered through more ordered – the presence of a sharply pronounced G peak. As the D/G ratio changes in the activated case, the crystallite size changes too, but for the carbonized sample it remains stable.

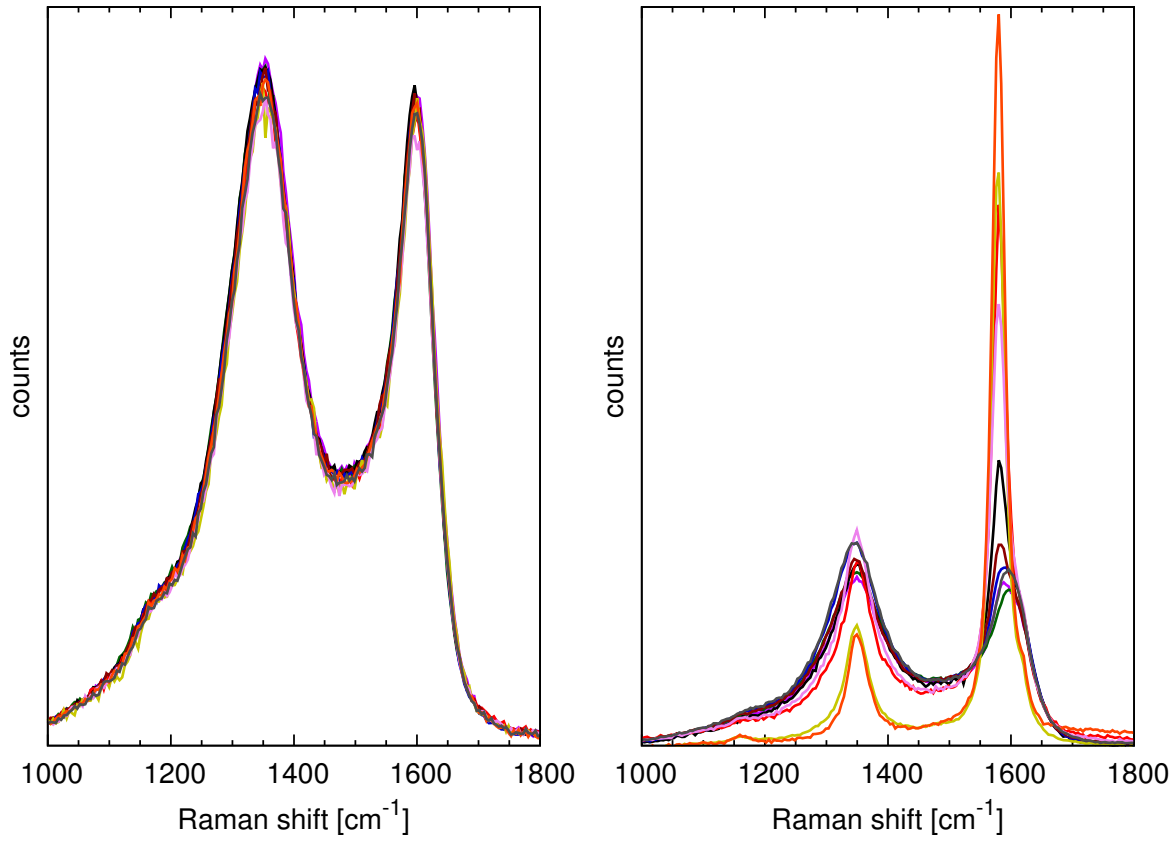

(a) carbonized sample

(b) activated sample

Figure 4.47: Visualisation of Raman scattering by the cellulose samples. Data was modified in order to be in the same range in the figure.

Table 4.14: Peak positions, D/G ratio and crystalline size (L_a) for the carbonized cellulose sample.

	G[cm^{-1}]	D[cm^{-1}]	D'[cm^{-1}]	D''[cm^{-1}]	D'''[cm^{-1}]	D/G	L_a[Å]
1	1587	1349	1617	1515	1190	1.56	28
2	1587	1349	1618	1516	1183	1.58	28
3	1587	1352	1617	1517	1184	1.64	27
4	1588	1348	1618	1516	1183	1.47	30
5	1587	1349	1619	1515	1184	1.50	29
6	1587	1349	1617	1523	1186	1.64	27
7	1587	1348	1617	1515	1184	1.50	29
8	1587	1347	1618	1515	1183	1.47	30
9	1588	1351	1619	1515	1183	1.55	28
10	1585	1349	1616	1515	1187	1.68	26
avg.	**1587**	**1349**	**1618**	**1516**	**1185**	**1.56**	**28**

Table 4.15: Peak positions, D/G ratio and crystalline size (L_a) for the activated cellulose sample.

	G[cm^{-1}]	D[cm^{-1}]	D'[cm^{-1}]	D''[cm^{-1}]	D'''[cm^{-1}]	D/G	L_a[Å]
1	1580	1351	1620	1461	1161	0.14	308
2	1580	1349	1618	1499	1198	0.46	96
3	1579	1349	1618	1483	1211	0.20	223
4	1581	1347	1615	1511	1205	1.18	37
5	1581	1350	1616	1495	1217	0.32	139
6	1584	1346	1618	1514	1180	1.46	30
7	1582	1348	1619	1505	1187	0.72	62
8	1586	1347	1618	1511	1184	1.71	26
9	1585	1348	1619	1510	1184	1.36	32
10	1584	1346	1619	1506	1184	1.11	40
avg.	**1582**	**1348**	**1618**	**1499**	**1191**	**0.86**	**99**

4.4.2 Computer simulations

Microcrystalline model

The model parameters are gathered in Table 4.16. The model for the carbonized sample is shown at the top of figures: Figure 4.50 – $S(Q)$ compared to X-ray scattering data, Figure 4.48 – $S(Q)$ compared to neutron scattering data, Figure 4.51 – *PDF* compared to X-ray scattering data, Figure 4.49 – *PDF* compared to neutron scattering data. For the activated sample model is shown at the top of: Figure 4.52, Figure 4.54, Figure 4.53, Figure 4.55 in the same order. For both carbonized and activated samples it is obvious that the proposed models do not fit the measured data properly which is a sign that structural models need to be adjusted. The simulated functions present additional peaks, and the intensity of all visible peaks is too high as well. The difference in height of the 1^{st} peak, as well as the missing overlapping peak for the activated sample were not considered as features needing to be addressed at this stage since whole models suggest that additional disorder is necessary to properly represent the sample structure. The discrepancy factor R is presented in Table 4.20

Turbostratic model

The model parameters are gathered in Table 4.17. The computed model along with measured data for the carbonized sample is presented in figures: Figure 4.50 – $S(Q)$ for X-ray scattering data, Figure 4.48 – $S(Q)$ for neutron scattering data, Figure 4.51 – *PDF* for X-ray scattering data, Figure 4.49 – *PDF* for neutron scattering data. In the same fashion figures for activated sample are compiled: Figure 4.52, Figure 4.54, Figure 4.53, Figure 4.55. It is visible in the presented figures that despite introducing additional disorder through breaking correlations along the c axis through introducing rotation, the peaks presented in both models are still too pronounced to be regarded as properly reproducing the measured data. Based on the same reasoning, discrepancies for the (002) peak were disregarded since additional models needed to be constructed. As the R values were the model's validating feature they are gathered in Table 4.20

Table 4.16: Parameters for microcrystalline model for cellulose samples.

parameter	carbonized	activated
No. of layers	3	3
ϕ of system	19.6 Å	22 Å
lattice parameters a & b	2.442 Å	2.442Å
lattice parameter c	6.92 Å	6.92Å
σ_{intra}	0.03 Å	0.03 Å
σ_{inter}	0.03 Å	0.03 Å

Table 4.17: Parameters for the turbostratic model for the cellulose samples.

parameter	carbonized	activated
No. of layers	3	3
ϕ of system	19.6 Å	22 Å
lattice parameters a & b	2.442 Å	2.442Å
lattice parameter c	6.92 Å	6.92Å
range of rotation angles	0^o–20^o	0^o–22^o
σ_{intra}	0.03 Å	0.03 Å
σ_{inter}	0.03 Å	0.03 Å

Paracrystalline model

The model parameters are gathered in Table 4.18. For the carbonized sample the $S(Q)$ and the *PDFs* are gathered in (neutron, X-ray data): Figure 4.48, Figure 4.50, Figure 4.49, Figure 4.51. The same is valid for activated sample for figures: Figure 4.52, Figure 4.54, Figure 4.53, Figure 4.55. In order to account for the previously disregarded features of the 1^{st} peak of the activated sample, the final model was constructed as a weighted sum of two separate paracrystalline models: with a lower and a higher number of layers. In order not to overcomplicate the final model most of the parameters were kept the same for the two components. The first one to be finalized was the lower-layered component since it has a bigger impact on the overall model. The parameters of that component were used as the starting point for the higher-layered component. The lattice parameter c, the σ_1 and the number of layers were subsequently adjusted in order to recreate the overlapping feature of the measured data. The validation of this approach is clearly visible through values of the discrepancy factor gathered in Table 4.20.

Table 4.18: Parameters for the paracrystalline model for the cellulose samples.

parameter	carbonized	activated (low)	activated (high)
No. of layers	3	3	18
% of layers	100 %	80 %	20 %
ϕ of system	19.6 Å	22 Å	22 Å
lattice parameters a & b	2.442 Å	2.442Å	2.442Å
lattice parameter c	6.92 Å	6.92Å	6.81Å
range of rotation angles	0^o–20^o	0^o–22^o	0^o–22^o
σ_0	0.044 Å	0.044 Å	0.044 Å
σ_1	0.28 Å	0.25 Å	0.19 Å
No. of averaged structures	100	100	100

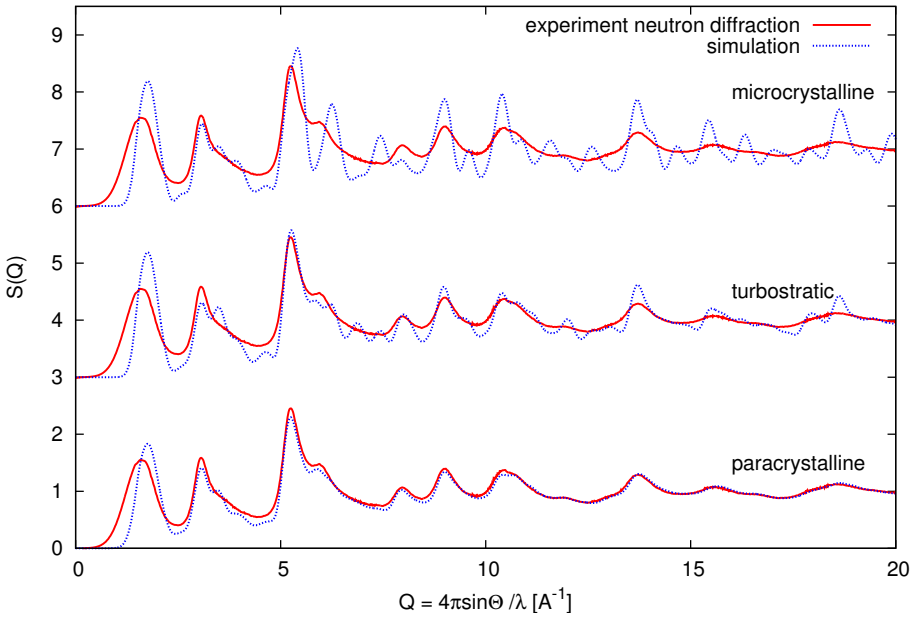

Figure 4.48: Comparison of the structural factors for: paracrystalline, turbostratic and microcrystalline models with the neutron experimental data for carbonized cellulose.

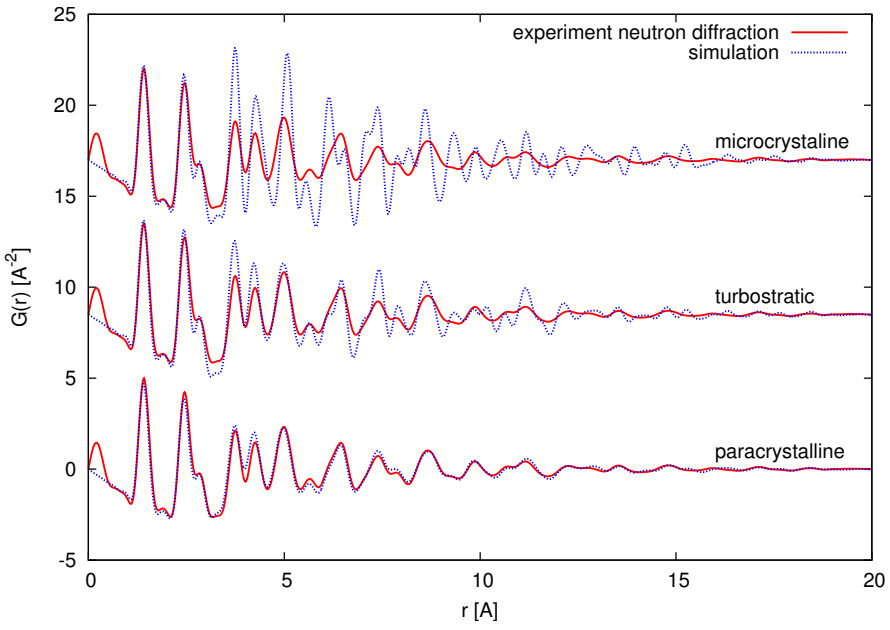

Figure 4.49: Comparison of the PDFs for: paracrystalline, turbostratic and microcrystalline models with the neutron experimental data for carbonized cellulose.

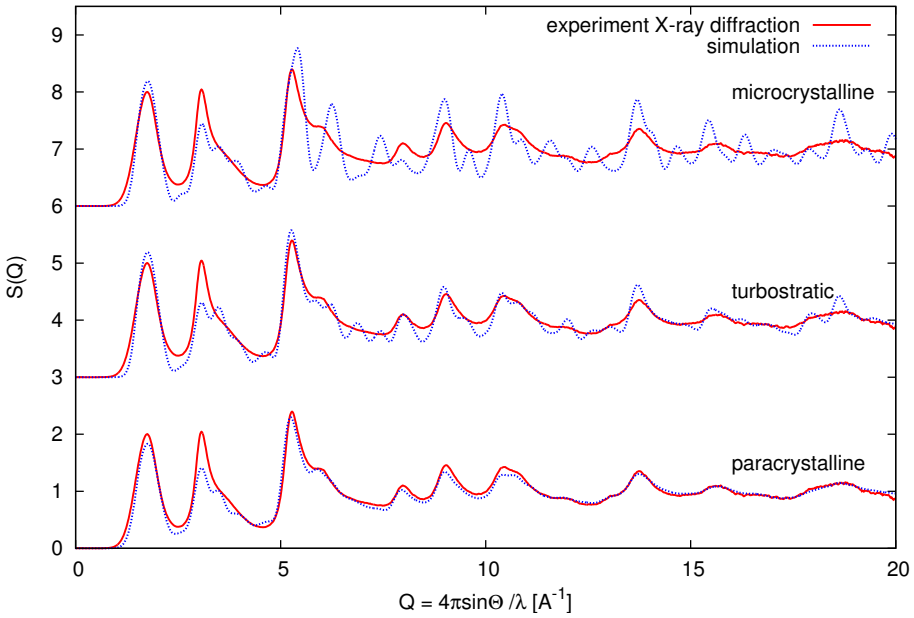

Figure 4.50: Comparison of the structural factors for: paracrystalline, turbostratic and microcrystalline models with the X-ray experimental data for carbonized cellulose.

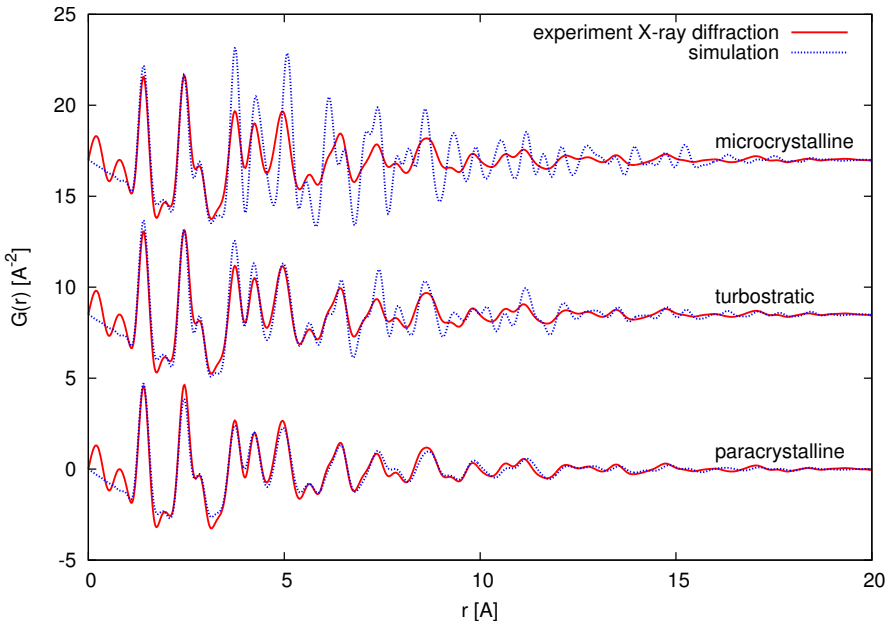

Figure 4.51: Comparison of the PDFs for: paracrystalline, turbostratic and microcrystalline models with the X-ray experimental data for carbonized cellulose.

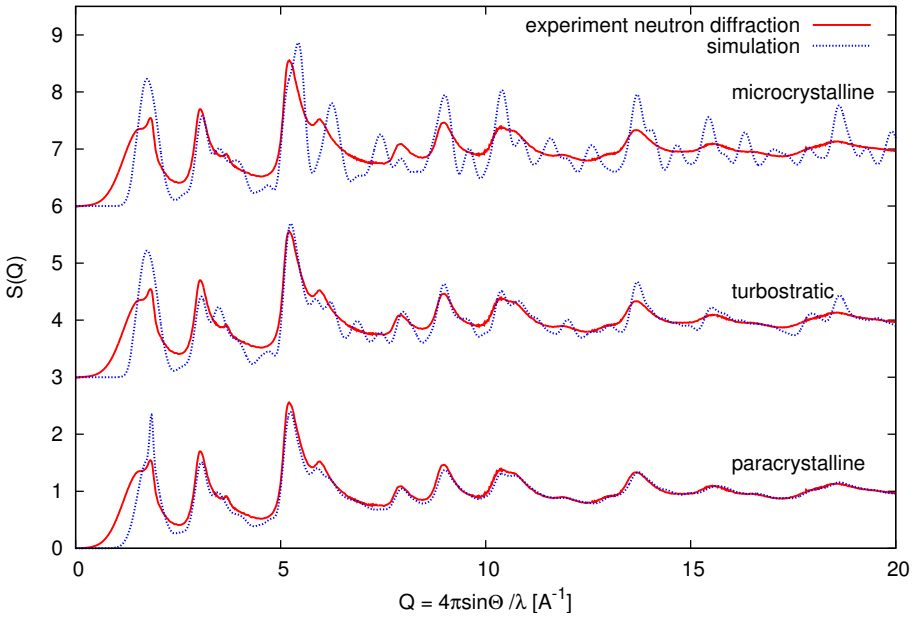

Figure 4.52: Comparison of the structural factors for: paracrystalline, turbostratic and microcrystalline models with the neutron experimental data for activated cellulose.

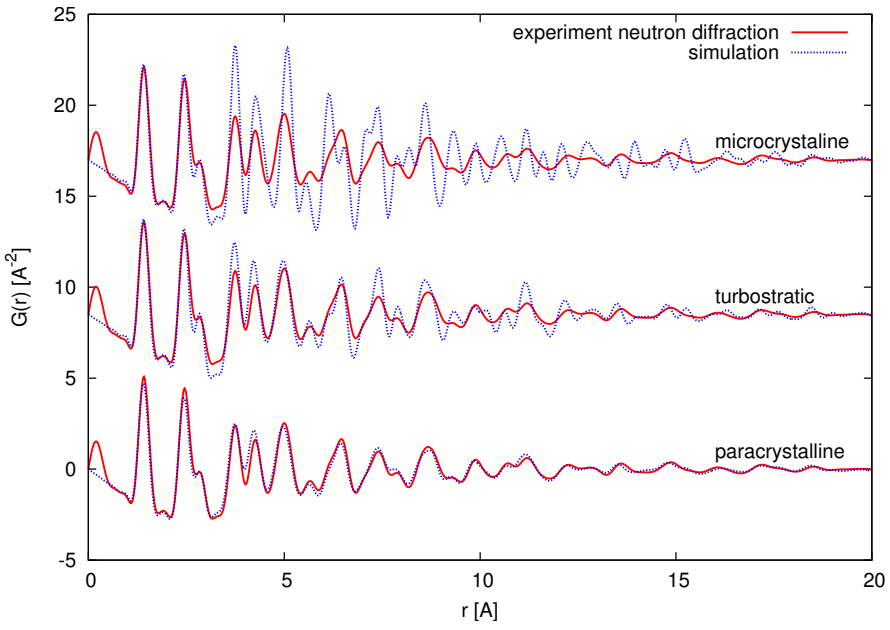

Figure 4.53: Comparison of the PDFs for: paracrystalline, turbostratic and microcrystalline models with the neutron experimental data for activated cellulose.

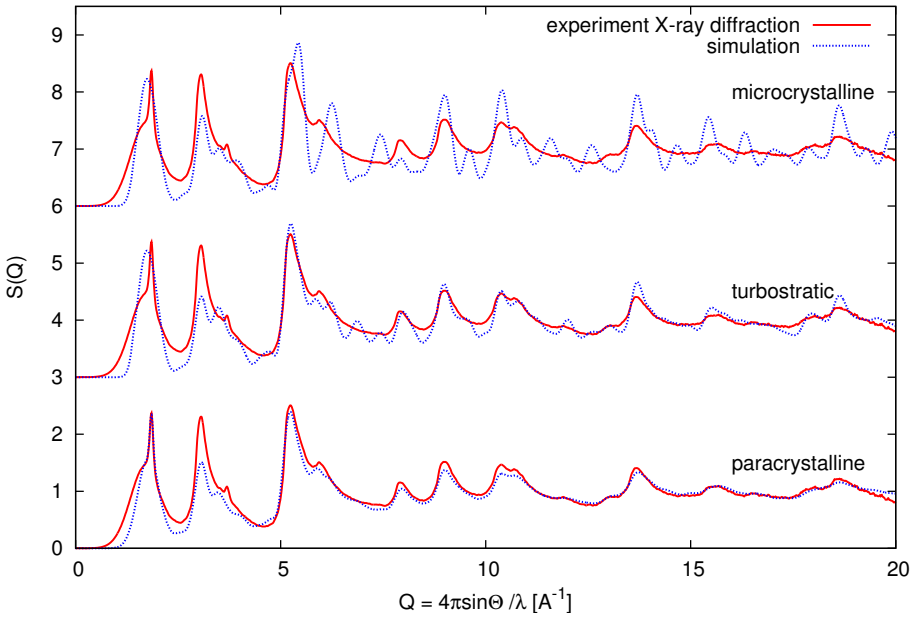

Figure 4.54: Comparison of the structural factors for: paracrystalline, turbostratic and microcrystalline models with the X-ray experimental data for activated cellulose.

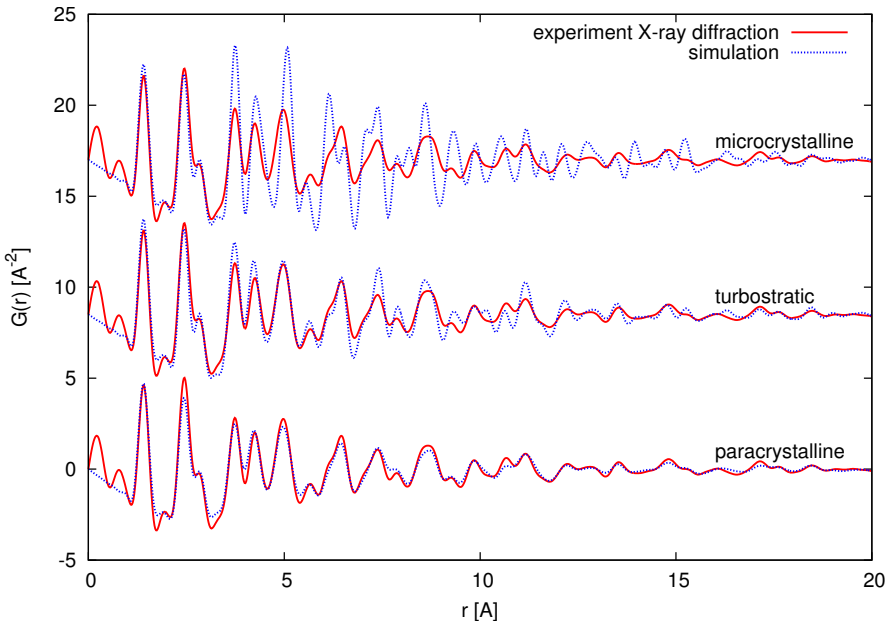

Figure 4.55: Comparison of the PDFs for: paracrystalline, turbostratic and microcrystalline models with the X-ray experimental data for activated cellulose.

Molecular dynamics

The models parameters are gathered in Table 4.19. For the carbonized sample the calculated $S(Q)$ and *PDFs* for selected models are compared to the measured data in the figures: Figure 4.56, Figure 4.58, Figure 4.57, Figure 4.59. For the activated sample the same is done in the figures: Figure 4.60, Figure 4.62, Figure 4.61, Figure 4.63. For the activated sample the final model is a weighted sum of two components. Since calculating models with 18 layers would involve more than 2800 atoms, it was decided as being more reasonable to use the paracrystalline model as a high-layered component for the final model for the activated sample. Additionally, such a procedure made it possible to have more precise control over the required peak position than would be possible with a pure MD simulation since in MD simulations only potentials influence interlayer distance, which can also lead to shifts between layer positions, creating voids and leading to lower peak amplitude. Such an approach was validated by a low percentage paracrystalline addition as well as the fact that after taking into account the weight of the paracrystalline component it has almost no influence in areas other than the 1^{st} peak. The ratio between the two components was preserved as calculated for the paracrystalline model. Judging by the presented $S(Q)$ and *PDFs* and taking into account the values of the discrepancy factor Table 4.20, one can discredit STW type of defect in both cases. For the carbonized sample both neutron and X-ray data present a better agreement with the model containing mono vacancies. In the case of the activated sample it is more difficult to unambiguously distinguish between models containing mono and di vacancies. This situation arises possibly due to the fact that even though both methods: neutrons and X-ray scattering are similar, they have slightly different sensitivities to various factors. Moreover models considered in this work are simplified in comparison to the true sample structure and are based on averaged data, which can lead to the conclusion that both mono and di vacancies are present in the structure. The Figure 4.64 shows visualisations of proposed models containing mono- and di- vacancies for both samples.

Table 4.19: The parameters for MD models for cellulose samples.

parameter	carbonized	activated
No. of layers – low	3	3
% of layers – low	100 %	80 %
No. of layers – high	–	18
% of layers – high	–	20 %
No. of mono-vacancies per layer	2	$2^2/_3$
No. of di-vacancies per layer	$1^1/_3$	$2^1/_3$
No. of STW type of defect per layer	1	$2^1/_3$

Table 4.20: Discrepancy factors between models and experimental data.

model	carbonized		activated	
	R_{x-ray}	$R_{neutrons}$	R_{x-ray}	$R_{neutrons}$
microcrystalline	94.0%	103.5%	92.7%	101.1%
turbostratic	41.8%	50.1%	42.0%	47.0%
paracrystalline	27.3%	27.0%	31.1%	27.1%
mono-vacancy	30.7 %	24.6%	31.1%	23.8 %
di-vacancy	32.6%	24.9%	32.1%	23.4 %
STW type defect	37.7%	34.2%	33.8%	27.4 %

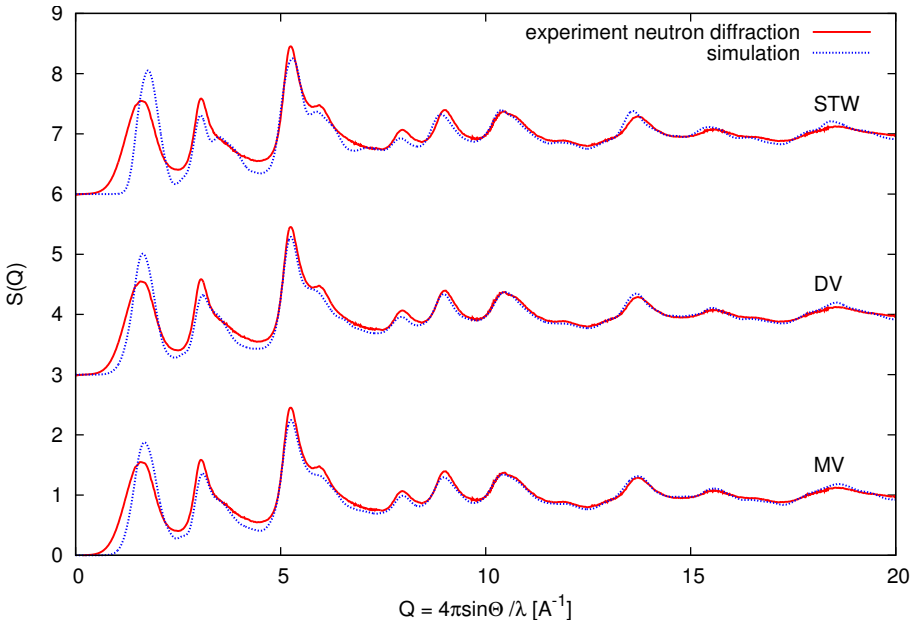

Figure 4.56: Comparison of the structural factors for theoretical models containing: mono-, di- vacancies and STW type defects with the neutron experimental data for carbonized cellulose.

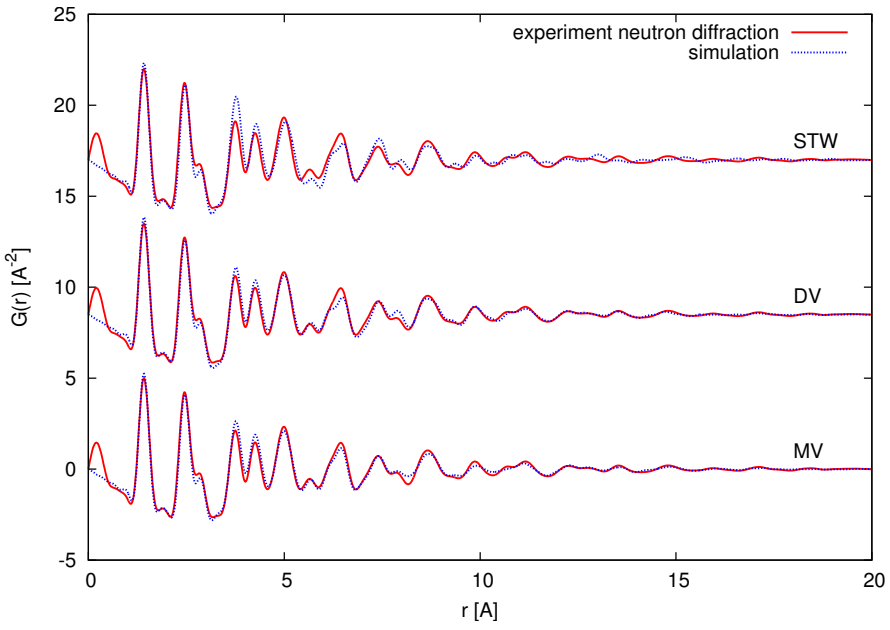

Figure 4.57: Comparison of the PDFs for theoretical models containing: mono-, di-vacancies and STW type defects with the neutron experimental data for carbonized cellulose.

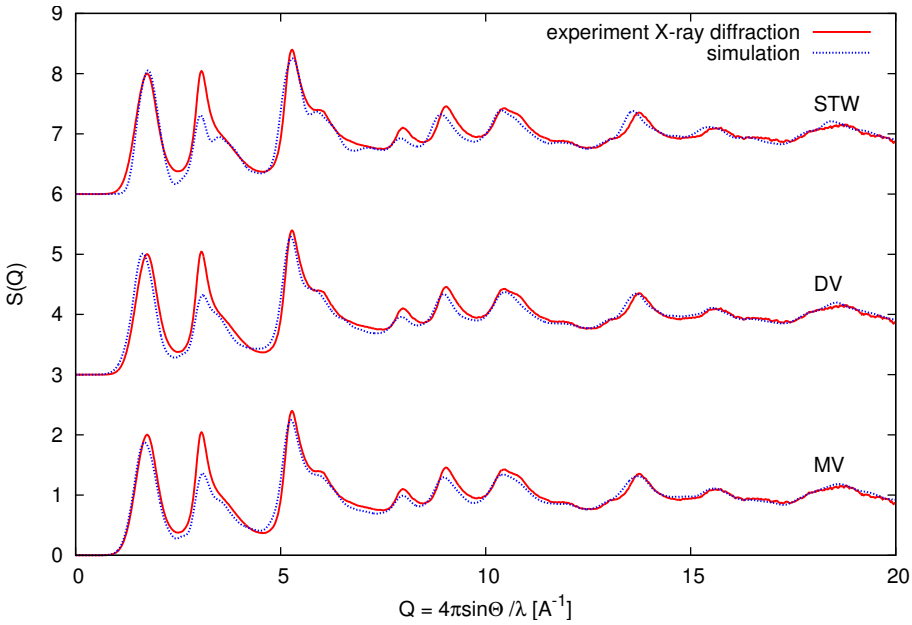

Figure 4.58: Comparison of the structural factors for theoretical models containing: mono-, di- vacancies and STW type defects with the X-ray experimental data for carbonized cellulose.

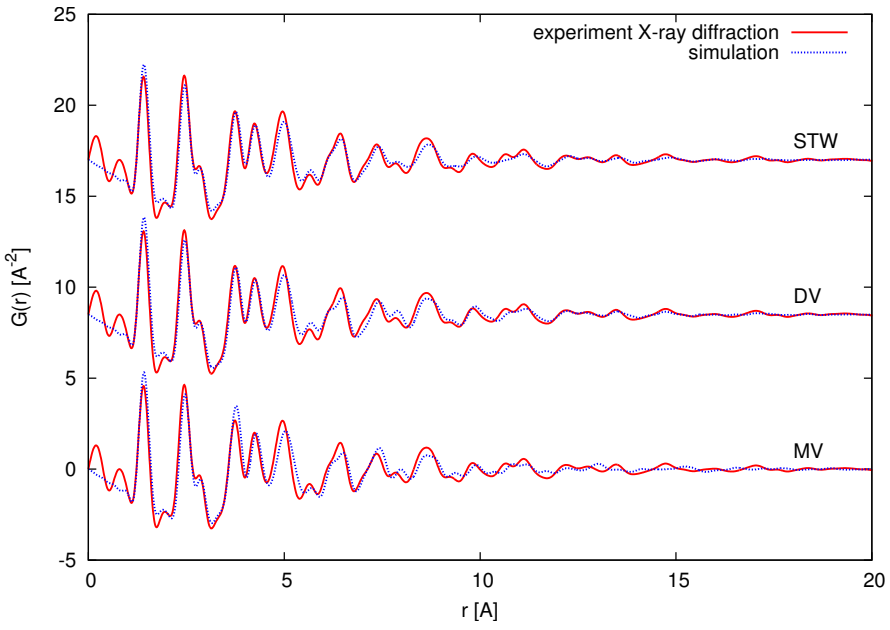

Figure 4.59: Comparison of the PDFs for theoretical models containing: mono- and di- vacancies and STW type defects with the X-ray experimental data for carbonized cellulose.

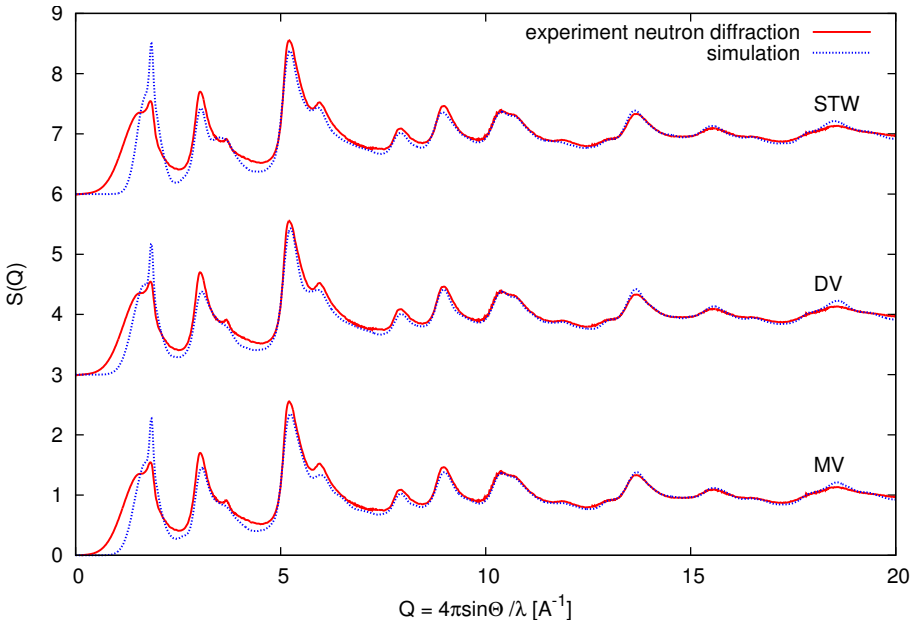

Figure 4.60: Comparison of the structural factors for theoretical models containing: mono-, di- vacancies and STW type defects with the neutron experimental data for activated cellulose.

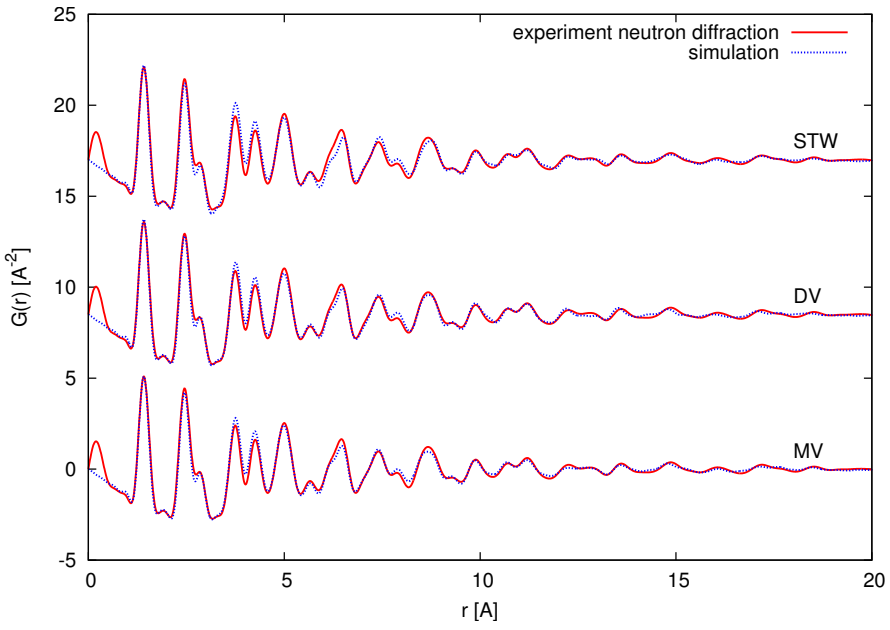

Figure 4.61: Comparison of the PDFs for theoretical models containing: mono-, di-vacancies and STW type defects with the neutron experimental data for activated cellulose.

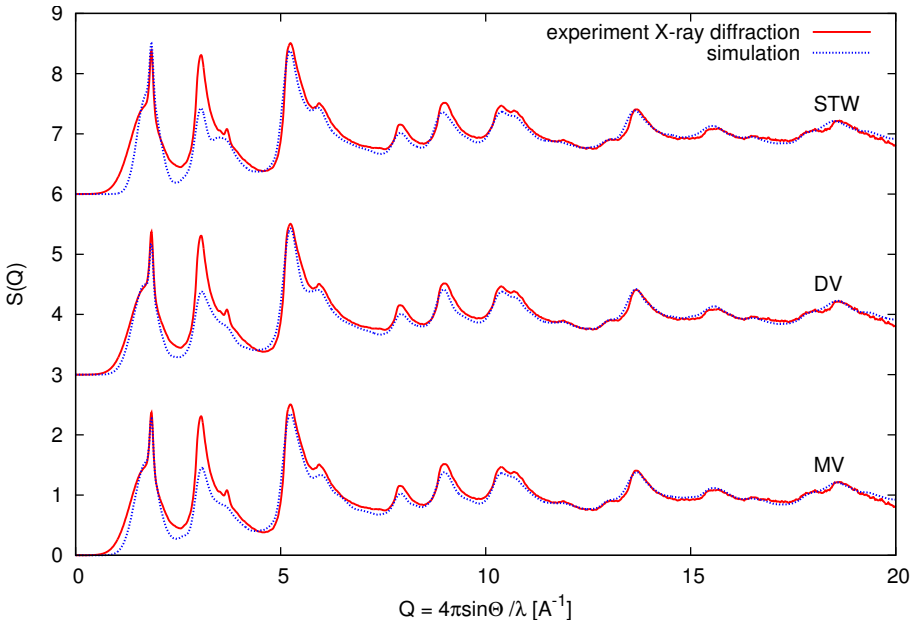

Figure 4.62: Comparison of the structural factors for theoretical models containing: mono-, di- vacancies and STW type defects with the X-ray experimental data for activated cellulose.

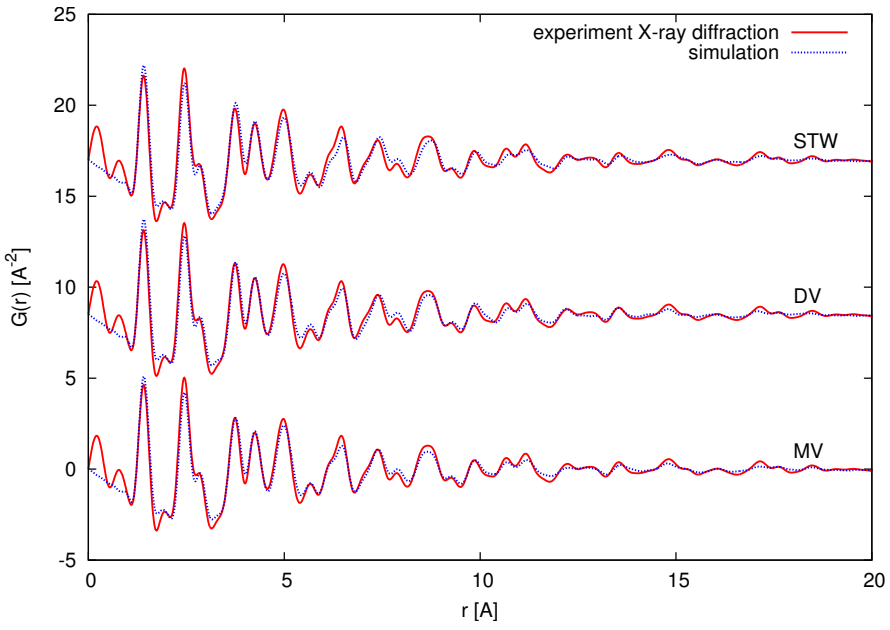

Figure 4.63: Comparison of the PDFs for theoretical models containing: mono- and di- vacancies and STW type defects with the X-ray experimental data for activated cellulose.

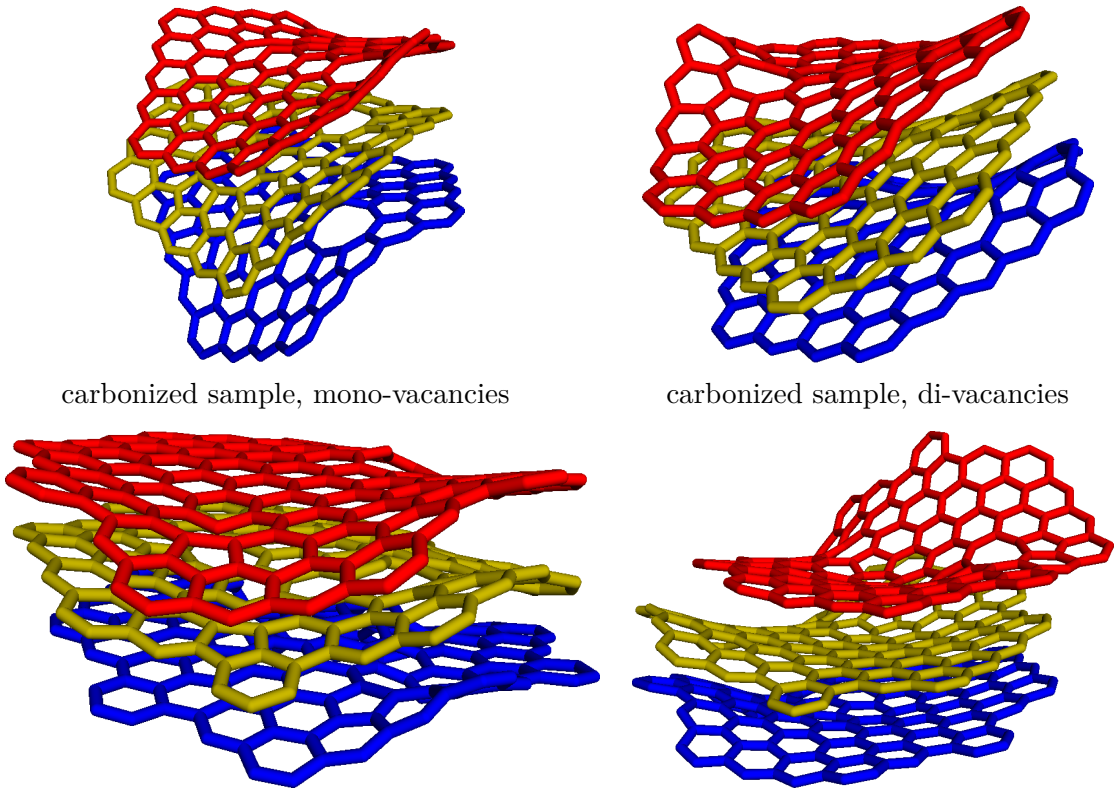

carbonized sample, mono-vacancies

carbonized sample, di-vacancies

activated sample, mono-vacancies

activated sample, di-vacancies

Figure 4.64: Visualisation of MD simulations for cellulose sample containing mono- and di- vacancies.

4.4.3 Summary

Also in case of measurements of the cellulose sample, the obtained results are in agreement between applied techniques.

Similarly to the saccharose case, the carbonized cellulose sample presents a more homogeneous structure than the sample after activation. The average value of crystallite size L_a obtained from Raman measurements is equal to 28 Å. The diffraction techniques provided a smaller value of 19.6 Å. The discrepancies between the obtained values can be accounted for by the fact that the Raman equation is an empirical one and dependent on fitting the obtained data. The Raman-diffraction discrepancy is most likely caused by the fact that the structure of the sample consists of interlinked honeycomb regions. The number of layers was estimated as 3 based on computer simulations combined with measurements from diffraction techniques.

For the activated sample, the obtained results show a more inhomogeneous structure with a mixed number of layers. Most of the sample consists of 3 layers on average, however it is impossible to omit the addition of a 18-layered fraction which is most likely localized within pore walls as the *HRTEM* images suggest. It was calculated that high-layered fraction constitutes 20% of the whole structure. The computer simulations backed by X-ray/neutron scattering measurements suggest that coherently scattering regions have a diameter of 22 Å. From the Raman scattering results an average value $L_a = 99$ was obtained. The obtained values varied from 26 Å to 308 Å. The sample is visibly inhomogeneous which makes this value a little less trustworthy, with the same reasoning as in the case of saccharose.

The activation process changed the sample's structure, most visibly by creating high-layered regions within pore walls.

5 Conclusions

The selected techniques complement each other, solidifying drawn conclusions and painting a wholesome image of the investigated materials. In the proposed approach, data obtained through Raman scattering and *HRTEM* provide clues for the construction of atomistic models. The information obtained in such a way strictly depends upon the location where it was collected. In case of highly homogeneous samples it does necessarily change the outcome, however when structure varies a lot through the sample volume the main method used in this work shows its true potential. The results presented in this work show that scattering techniques combined together with computational methods provide detailed structural information about investigated materials. Because of the nature of the investigated materials, they cannot be classified as a crystalline or a slightly distorted crystalline material and thus cannot be treated with procedures developed for such materials. In order to extract most of the structural information contained in the collected data, computer simulations need to be combined with analysis of the diffraction data in real space through the formalism of *PDFs*. It not only provides estimates of the size of coherently scattering regions but also makes it possible to speculate about the defective nature of the material. The theoretical calculations can be directly verified by comparison with the experimental data both in reciprocal and real space. By combining computer simulations with diffraction methods we are able to obtain structural information about larger sample volume when compared with information obtained from direct imaging techniques which are local probes of the structure. They however provide valuable insights into sample structure from different perspectives and fill in the existing gaps in the material's structural image.

The investigated materials have numerous applications and are highly valued for their properties. Their physical and chemical properties are strongly influenced by the presence of defects, and thus detailed knowledge of their structure at the atomic level is

necessary for a deeper understanding of the synthesis procedures. By linking knowledge about the structure and preparation process, materials with improved properties and performance can be engineered. In the case of graphene most efforts are dedicated towards obtaining large non-defected single layers, however precisely ordered defects change material properties in a strictly controlled way that it is e.g. conducting only through designated paths. For activated carbons structural information provides insight into the activation process allowing tailor-fitting materials: for filters – e.g. targeting a certain size of molecule, for gasses storage – increasing storage capacity, for supercapacitors – fine tuning capacity, and many others. Such an approach is expected to be valuable for a wide variety of industrial applications for the structural characterization of carbon materials and for detecting and describing their structural defects while produced on a mass scale.

Bibliography

[1] A Bielański. *Podstawy chemii nieorganicznej*, volume 3. PWN, 2002. ISBN 8301138165.

[2] R Saito, G Dresselhaus, and M Dresselhaus. *Pysical Properties of Carbon Nanotubes*. Imperial College Press, 1998. ISBN 1860940935.

[3] ZQ Li, CJ Lu, ZP Xia, Y Zhou, and Z Luo. X-ray diffraction patterns of graphite and turbostratic carbon. *Carbon*, 45(8):1686 – 1695, 2007. ISSN 0008-6223.

[4] BE Warren. X-ray diffraction in random layer lattices. *Physical Review*, 59(9):693, 1941.

[5] KS Novoselov, AK Geim, SV Morozov, D Jiang, Y Zhang, SV Dubonos, IV Grigorieva, and AA Firsov. Electric field effect in atomically thin carbon films. *Science*, 306(5696):666–669, 2004.

[6] F Bonaccorso, A Lombardo, T Hasan, Z Sun, L Colombo, and AC Ferrari. Production and processing of graphene and 2d crystals. *Materials Today*, 15(12): 564 – 589, 2012.

[7] PT Araujo, M Terrones, and MS Dresselhaus. Defects and impurities in graphene-like materials. *Materials Today*, 15(3):98–109, 2012.

[8] X Wang, L Zhi, and K Mullen. Transparent, conductive graphene electrodes for dye-sensitized solar cells. *Nano Letters*, 8(1):323–327, 2008.

[9] Y Zhang, Y-W Tan, Horst L Stormer, and P Kim. Experimental observation of the quantum hall effect and berry's phase in graphene. *Nature*, 438:201–204, 2005.

[10] F Schedin, AK Geim, SV Morozov, EW Hill, P Blake, MI Katsnelson, and KS Novoselov. Detection of individual gas molecules adsorbed on graphene. *Nat Mater*, 6:652–655, 2007.

[11] S Stankovich, DA Dikin, GHB Dommett, KM Kohlhaas, EJ Zimney, EA Stach, RD Piner, ST Nguyen, and RS Ruoff. Graphene-based composite materials. *Nature*, 442:282–286, 2006.

[12] RE Franklin. Crystallite growth in graphitizing and non-graphitizing carbons. *Proceedings of the Royal Society of London A: Mathematical, Physical and Engineering Sciences*, 209(1097):196–218, 1951.

[13] H Marsh and F Rodriguez-Reinoso. *Activated Carbon*. Elsevier Science and Technology Books, 2006. ISBN 0080444636.

[14] S Duber, J-N Rouzaud, C Clinard, and S Pusz. Microporosity and optical properties of some activated chars. *Fuel processing technology*, 77:221–227, 2002.

[15] J Rouquerol, D Avnir, CW Fairbridge, DH Everett, JH Haynes, N Pernicone, JDF Ramsay, KSW Sing, and KK Unger. recommendations for the characterization of porous solids (technical report). *Pure and Applied Chemistry*, 66:1739–1758, 1994.

[16] RCh Bansal and M Goyal. *Activated Carbon Adsorption*. CRC Press, 2005. ISBN 0824753445.

[17] PJF Harris. Structure of non-graphitising carbons. *International Materials Reviews*, 42(5):206–218, 1997.

[18] PJF Harris, A Burian, and S Duber. High-resolution electron microscopy of a microporous carbon. *Philosophical Magazine Letters*, 80(6):381–386, 2000.

[19] PJF Harris. Fullerene-related structure of commercial glassy carbons. *Philosophical Magazine*, 84(29):3159–3167, 2004.

[20] PJF Harris. New perspectives on the structure of graphitic carbons. *Critical Reviews in Solid State and Materials Sciences*, 30(4):235–253, 2005.

[21] PJF Harris, Z Liu, and K Suenaga. Imaging the atomic structure of activated carbon. *Journal of physics: Condensed matter*, 20(36):362201, 2008.

[22] WS Hummers and RE Offeman. Preparation of graphitic oxide. *Journal of the American Chemical Society*, 80(6):1339–1339, 1958.

[23] J Lindon, G Tranter, and J Holmes, editors. *Encyclopedia of Spectroscopy and Spectrometry*, volume 2. Academic Press, 2000.

[24] GE Bacon. *Neutron Diffraction. Monographs on the Physics and Chemistry of Materials*. Oxford University Press, 2nd. edition edition, 1962.

[25] J Baruchel. *Neutron and synchrotron radiation for condensed matter studies: Theory, instruments and methods*. Neutron and Synchrotron Radiation for Condensed Matter Studies. Springer-Verlag, 1993. ISBN 9783540565611.

[26] PSI webpage. http://www.psi.ch/.

[27] ISIS webpage. http://www.isis.stfc.ac.uk/.

[28] ESS webpage. https://europeanspallationsource.se/.

[29] ILL webpage. http://www.ill.eu/.

[30] T Egami and SJL Billinge. *Underneath the Bragg peaks: structural analysis of complex materials*. w. H. Freeman and company, 2003.

[31] HE Fischer, AC Barnes, and PS Salmon. Neutron and x-ray diffraction studies of liquids and glasses. *Reports on Progress in Physics*, 69(1):233, 2006.

[32] Y Waseda. *Anomalous X-Ray Scattering For Materials Characterisation. Atomic-scale Structure Determination*. Springer, 2002.

[33] RE Dinnebier and SJL Billinge. *Powder Diffraction. Theory and Practice*. The Royal Society of Chemistry, 2008. ISBN 9780854042319.

[34] ESRF webpage. http://www.esrf.eu/.

[35] A Guinier. *X-Ray Diffraction In Crystals, Imperfect Crystals and Amorphus Bodies*. Elsevier, 1963.

[36] R Guinebretière. *X-ray Diffraction by Polycrystalline Materials*. ISTE, 2007. ISBN 9781905209217.

[37] HH Rose. Optics of high-performance electron microscopes. *Science and Technology of Advanced Materials*, 9(1):014107, 2008.

[38] B Fultz and JM Howe. *Transmission electron microscopy and diffractometry of materials*. Springer Science & Business Media, 2012.

[39] F Tuinstra and JL Koenig. Raman spectrum of graphite. *The Journal of Chemical Physics*, 53(3):1126–1130, 1970.

[40] AC Ferrari and J Robertson. Interpretation of raman spectra of disordered and amorphous carbon. *Phys. Rev. B*, 61:14095–14107, May 2000.

[41] DS Knight and WB White. Characterization of diamond films by raman spectroscopy. *Journal of Materials Research*, 4(02):385–393, 1989.

[42] MJ Matthews, MA Pimenta, G Dresselhaus, MS Dresselhaus, and M Endo. Origin of dispersive effects of the raman d band in carbon materials. *Physical Review B*, 59(10):R6585, 1999.

[43] A Sadezky, H Muckenhuber, H Grothe, R Niessner, and U Pöschl. Raman microspectroscopy of soot and related carbonaceous materials: spectral analysis and structural information. *Carbon*, 43(8):1731–1742, 2005.

[44] M Pawlyta, J-N Rouzaud, and S Duber. Raman microspectroscopy characterization of carbon blacks: Spectral analysis and structural information. *Carbon*, 84:479–490, 2015.

[45] MS Dresselhaus, A Jorio, AG Souza Filho, and R Saito. Defect characterization in graphene and carbon nanotubes using raman spectroscopy. *Philosophical Transactions of the Royal Society of London A: Mathematical, Physical and Engineering Sciences*, 368(1932):5355–5377, 2010.

[46] L Hawelek, A Brodka, JC Dore, V Honkimäki, and A Burian. Fullerene-like structure of activated carbons. *Diamond and Related Materials*, 17(7):1633–1638, 2008.

[47] L Hawelek, A Brodka, JC Dore, V Honkimaki, S Tomita, and A Burian. Structural studies of nanodiamond by high-energy x-ray diffraction. *Diamond and Related Materials*, 17(7):1186–1193, 2008.

[48] L Hawelek, W Wrzalik, A Brodka, JC Dore, AC Hannon, S Iijima, M Yudasaka, T Ohba, K Kaneko, and A Burian. A pulsed neutron diffraction study of the topological defects presence in carbon nanohorns. *Chemical Physics Letters*, 502 (1):87–91, 2011.

[49] L Hawelek, N Woznica, A Brodka, V Fierro, A Celzard, A Bulou, and A Burian. Graphene-like structure of activated anthracites. *Journal of Physics: Condensed Matter*, 24(49):495303, 2012.

[50] AM Hindeleh and R Hosemann. Microparacrystals: The intermediate stage between crystalline and amorphous. *Journal of Materials Science*, 26(19):5127–5133, 1991. ISSN 00222461.

[51] R Brämer and W Ruland. The limitations of the paracrystalline model of disorder. *Die Makromolekulare Chemie*, 177(12):3601–3617, 1976.

[52] A Brodka, J Kołoczek, and A Burian. Application of molecular dynamics simulations for structural studies of carbon nanotubes. *Journal of nanoscience and nanotechnology*, 7(4-5):1505–1511, 2007.

[53] J Tersoff. Empirical interatomic potential for silicon with improved elastic properties. *Physical Review B*, 38(14):9902, 1988.

[54] J Tersoff. Empirical interatomic potential for carbon, with applications to amorphous carbon. *Physical Review Letters*, 61(25):2879, 1988.

[55] J Tersoff. Modeling solid-state chemistry: Interatomic potentials for multicomponent systems. *Physical Review B*, 39(8):5566, 1989.

[56] GC Abell. Empirical chemical pseudopotential theory of molecular and metallic bonding. *Physical Review B*, 31(10):6184, 1985.

[57] DW Brenner, OA Shenderova, JA Harrison, SJ Stuart, B Ni, and SB Sinnott. A second-generation reactive empirical bond order (rebo) potential energy expression for hydrocarbons. *Journal of Physics: Condensed Matter*, 14(4):783, 2002.

[58] S J Stuart, AB Tutein, and JA Harrison. A reactive potential for hydrocarbons with intermolecular interactions. *The Journal of chemical physics*, 112(14):6472–6486, 2000.

[59] J Kotakoski, AV Krasheninnikov, and K Nordlund. Energetics, structure, and long-range interaction of vacancy-type defects in carbon nanotubes: Atomistic simulations. *Phys. Rev. B*, 74:245420, 2006.

[60] F Banhart, J Kotakoski, and AV Krasheninnikov. Structural defects in graphene. *ACS Nano*, 5(1):26–41, 2011.

[61] MM Ugeda, I Brihuega, F Hiebel, P Mallet, J Veuillen, JM Gómez-Rodríguez, and F Ynduráin. Electronic and structural characterization of divacancies in irradiated graphene. *Physical Review B*, 85(12):121402, 2012.

[62] PA Thrower. *Chemistry and Physics of Carbon*, volume 5. Marcel Dekker Publishers, 1969.

[63] AJ Stone and DJ Wales. Theoretical studies of icosahedral c60 and some related species. *Chemical Physics Letters*, 128(5–6):501 – 503, 1986.

[64] J Kotakoski, JC Meyer, S Kurasch, D Santos-Cottin, U Kaiser, and AV Krasheninnikov. Stone-wales-type transformations in carbon nanostructures driven by electron irradiation. *Physical Review B*, 83(24):245420, 2011.

[65] HE Fischer, GJ Cuello, P Palleau, D Feltin, AC Barnes, YS Badyal, and JM Simonson. D4c: A very high precision diffractometer for disordered materials. *Applied Physics A*, 74:s160–s162, 2002.

[66] MA Howe, RL McGreevy, and P Zetterström. Correct: A correction program for neutron diffraction data. *NFL Studsvik internal report*, 1996.

[67] BE Warren and P Bodenstein. The diffraction pattern of fine particle carbon blacks. *Acta Crystallographica*, 18(2):282–286, 1965.

[68] S Ergun and RR Schehl. Analysis of the structure of a glassy carbon using the fourier transfor m technique. *Carbon*, 11(2):127 – 138, 1973.

[69] H Fujimoto. Theoretical x-ray scattering intensity of carbons with turbostratic stacking and ab stacking structures. *Carbon*, 41(8):1585 – 1592, 2003. ISSN 0008-6223.

[70] R Hosemann and SN Bagchi. *Direct analysis of diffraction by matter*. North-Holland Pub. Co., 1962.

[71] AM Hindeleh and R Hosemann. Paracrystals representing the physical state of matter. *Journal of Physics C: Solid State Physics*, 21(23):4155, 1988.

[72] R Hosemann and AM Hindeleh. Structure of crystalline and paracrystalline condensed matter. *Journal of Macromolecular Science, Part B*, 34(4):327–356, 1995.

[73] L Hawelek, J Koloczek, A Brodka, JC Dore, V Honkimaki, and A Burian. Structural studies of disordered carbons by high-energy x-ray diffraction. *Philosophical Magazine*, 87(32):4973–4986, 2007.

[74] A Burian, A Ratuszna, and JC Dore. Radial distribution function analysis of the structure of activated carbons. *Carbon*, 36(11):1613 – 1621, 1998.

[75] JC Dore, M Sliwinski, A Burian, WS Howells, and D Cazorla. Structural studies of activated carbons by pulsed neutron diffraction. *Journal of Physics: Condensed Matter*, 11(47):9189, 1999.

[76] A Szczygielska, A Burian, and JC Dore. Paracrystalline structure of activated carbons. *Journal of Physics: Condensed Matter*, 13(24):5545, 2001.

[77] LA Girifalco, M Hodak, and Roland S Lee. Carbon nanotubes, buckyballs, ropes, and a universal graphitic potential. *Phys. Rev. B*, 62:13104–13110, 2000.

[78] HJC Berendsen, JPM Postma, WF van Gunsteren, A DiNola, and JR Haak. Molecular dynamics with coupling to an external bath. *The Journal of Chemical Physics*, 81(8):3684–3690, 1984.